

The Pennsylvania State University

The Graduate School

Department of Physics

PLASMON DISPERSION IN TWO-DIMENSIONAL
CHARGE-SHEETS

A Dissertation in

Physics

by

Yu Liu

© 2009 Yu Liu

Submitted in Partial Fulfillment
of the Requirements
for the Degree of

Doctor of Philosophy

May 2009

The dissertation of Yu Liu was reviewed and approved¹ by the following:

Roy Willis
Professor of Physics
Thesis Adviser
Chair of Committee

Xiaoxing Xi
Professor of Physics

Gerald Mahan
Professor of Physics

Nicholas Winograd
Professor of Chemistry

Jayanth Banavar
Professor of Physics
Department Head of Physics

¹ Signatures on file in the Graduate School.

Abstract

The dispersion of sheet plasmons in two-dimensional electron systems was investigated in an in-situ ultra high vacuum environment by angle-resolved high-resolution electron-energy-loss spectroscopy (HREELS). In particular, the two-dimensional electron systems investigated were silver-induced surface superstructure, $\text{Si}(111)(\sqrt{3} \times \sqrt{3})\text{-Ag}$, and an epitaxially grown graphene layer on $\text{SiC}(0001)$.

A two-dimensional sheet of charge was produced by precisely depositing a thin layer of silver onto $\text{Si}(111)(7 \times 7)$ to form $\text{Si}(111)(\sqrt{3} \times \sqrt{3})\text{-Ag}$ superstructure and characterized by HREELS. Measurements for low silver coverage confirmed a two-dimensional adatom gas phase previously discovered by other experimental techniques and also determined the critical coverage to sustain this phase. A further deposition of silver adatoms destroyed the two-dimensional adatom gas phase, and silver grew in Stranski-Krastanov mode, forming silver micro-crystal after completion of the first silver layer. At this stage, the dispersion of sheet plasmons deviated from theoretical prediction, which features an opening of a gap where the momentum transfer vanishes. A calculation based on the theory of surface plasmons agreed with this observation, which implied this was a transition from a 2D-type plasmon to a 3D-type plasmon. This was a surprising result due to the unique electronic structure of $\text{Si}(111)(\sqrt{3} \times \sqrt{3})\text{-Ag}$ which maintained electron density roughly the same due to a depletion layer underneath the silicon surface. Eventually, the conventional surface plasmon was observed at the deposition of about 20 monolayers (ML) of silver, indicative of fully screening from the substrate.

HREELS studies of the sheet plasmon on a single graphene layer disclosed its two dimensional character and agreed with theoretical calculation of dispersion, but showed no damping where it was predicted. Also, we observed that the decay rate was roughly equal to the Fermi velocity.

The sheet-plasmon dispersion of few-layer graphene were characterized by HREELS. The 2-ML graphene had a similar behavior, whereas a peak splitting was observed around Fermi wavevector, due to the splitting of π and π^* band at the corner (\mathbf{K} point) of the hexagonal Brillouin zone. In measurements of 3- and 5-ML graphene layers, the opening gap between π and π^* band induced a gap of dispersion behavior which indicated the failure of the free-electron-gas picture due to the reformed band structure. A qualitatively kinematic analysis of momentum transfer of electrons was used to explain the similarity between band gap and energy gap in dispersion diagrams.

Table of Contents

List of Tables	viii
List of Figures	ix
Acknowledgments	xvii
Chapter 1. INTRODUCTION	1
1.1 Plasmons	1
1.2 Two Dimensional Electron Gas	4
Chapter 2. Experimental Setup	7
2.1 Ultra High Vacuum	7
2.1.1 UHV Chamber	8
2.1.1.1 Pumps	8
2.1.1.2 Preparation Chamber	10
2.1.1.3 HREELS Chamber	10
2.1.2 Quadrupole Mass Spectrometer	11
2.2 Electrons as a Tool for the Characterization	11
2.2.1 HREELS	12
2.2.1.1 Instrumentation	12
2.2.1.2 Dipole Scattering	18
2.2.1.3 Impact Scattering	21

	vi
2.2.2 LEED	21
2.3 Physical Vapor Deposition	25
2.4 Silicon Wafer Processing	28
2.4.1 Cleaning	29
2.4.2 Thermal Treatment	29
Chapter 3. Plasmon Dispersion of Reconstructed Silicon Surfaces	32
3.1 Si(111)(7×7)	33
3.1.1 Atomic and Electronic Structure of Si(111)(7×7)	33
3.1.1.1 Sample preparation	36
3.1.1.2 Results	36
3.2 Si(111)($\sqrt{3} \times \sqrt{3}$)-Ag	38
3.2.1 Atomic and Electronic Structure of Si(111)($\sqrt{3} \times \sqrt{3}$)-Ag . .	39
3.2.2 Sample Preparation	41
3.2.3 Plasmon Dispersion of Si(111)($\sqrt{3} \times \sqrt{3}$)-Ag	42
3.2.4 Evolvment of Plasmons Dispersion Behavior	49
3.3 Conclusion	60
Chapter 4. Plasmon Dispersion of Epitaxial Graphene Layer	61
4.1 From Graphite to Graphene	61
4.1.1 Graphite	61
4.1.2 Graphene	63
4.2 Single Layer Graphene	66
4.3 Conclusion	79

Chapter 5. Plasmon Dispersion of Multi-layer Graphene	81
5.1 Measurements of Multi-Layer Graphene	81
5.2 Discussion	88
5.3 Conclusion	92
Chapter 6. SUMMARY AND FUTURE STUDY	93
6.1 Summary	93
6.1.1 Si(111)-($\sqrt{3} \times \sqrt{3}$)-Ag	93
6.1.2 Graphene	94
6.1.3 Impact of the research	95
6.2 Future Study	96
Bibliography	97

List of Tables

2.1	Solutions of RCA cleaning of silicon wafer	29
-----	--	----

List of Figures

1.1	Schematic of 2D- and 3D-type plasmons.	2
1.2	(a) Change density distribution in a sheet; (b) electric field lines	3
1.3	Confinement of electrons in two types of potential well. (a) Triangle potential well in a semiconductor inversion layer, (b) square potential well on the surface of Si(111)($\sqrt{3} \times \sqrt{3}$)-Ag and graphene	5
2.1	A top view of UHV system in this thesis research.	9
2.2	The mean free path λ of electrons in solids as a function of their energy. This is curve also called the "universal curve" for the probing depth of electrons into solids; this is a complication of experimental data for a large variety of materials and energies [9].	13
2.3	A block diagram of the HREEL spectrometer.	14
2.4	the schematic of HREELS (LK2000-14-R)	15
2.5	monochromator is composed of two 127° cylinders with radius $a = 3$ cm and $b = 4$ cm respectively, the electrons with energy $E_0 = e \Delta V / 2 \ln(a/b)$ traverse along center path through monochromator. Accordingly, electrons with energy other than that terminated their trajectory either at outer plate ($E > E_0$) or inner plate ($E < E_0$)	17
2.6	Electric field in dipole scattering	19

2.7	Angle dependence of the absolute intensities as a function of the collection angle $\Delta\theta_s$. The scattering geometry is shown in the upper inset. Vibrational modes at 80 and 260 meV are only observed in the off-specular spectra, which are excited via the impact scattering mechanism. Figure from reference [16]	22
2.8	The principle of the formation of a diffraction pattern in a LEED experiment.	23
2.9	LEED schematic	26
2.10	Metallic vapor phase diagram.	27
2.11	The holder for heating silicon wafer.	31
3.1	Atomic structure of Si(111)(7×7). (a) Schematic of atomic arrangements; (b) STM image, from Omicron Inc.	34
3.2	Two-dimensional band-dispersion diagram for Si(111)(7×7) clean surface measured by ARUPS [21]	35
3.3	Electron-energy-loss-data from a clean Si(111)(7 × 7) sample. The red curve is the average of 5 nearest neighbor data points . The inset shows the LEED pattern generated by an electron beam of 64 eV.	37
3.4	Phase diagram obtained by STM-study of Ag/Si(111) system [26], showing surface reconstructions vs Ag coverage and annealing or growth temperature. The solid circles indicate initial growth conditions for a given sequence.	38

3.5	Atomic structure of Si(111)($\sqrt{3} \times \sqrt{3}$)-Ag. (a) Schematic of atomic arrangements; (b) STM image, from Omicron Inc.	39
3.6	Two-dimensional band-dispersion diagram for 1 ML Si(111)($\sqrt{3} \times \sqrt{3}$)-Ag surface measured by ARUPS [30]	40
3.7	HREEL-spectra taken from the same sample on Si(111)-(7 \times 7), (3 \times 1)-Ag, and ($\sqrt{3} \times \sqrt{3}$) surface at room temperature. Electron impact energy $E_0=20.29\text{eV}$ and incident angle $\theta=60^\circ$. Inset: LEED pattern of Si(111)($\sqrt{3} \times \sqrt{3}$)-Ag surface, taken at 90 eV of the incident electron beam.	43
3.8	Scattering geometry of HREELS used in this work. The analyzer can slide on the track to achieve off-specular scattering at various scattering angle ϕ_s	44
3.9	Spectra of Si(111)($\sqrt{3} \times \sqrt{3}$)-Ag at specular scattering ($\phi_s=0^\circ$) and off-specular ($\phi_s=2^\circ$). Inset: (a) 10-times magnified spectra; (b) background-removed spectra by using off-specular spectra subtracting specular one.	45
3.10	Background-removed spectra taken from Si(111)-($\sqrt{3} \times \sqrt{3}$)-Ag surface at room temperature. The black arrows indicate the center of loss peaks, with q at the right side corresponding to momentum transfers of measurements at various angles. Electrons impact energy: $E_0=20.29\text{eV}$, and incident angle: $\theta=60^\circ$	47

- 3.11 (a) Plasmon energy dispersion on Si(111)-($\sqrt{3} \times \sqrt{3}$)-Ag surface. The red curve is the best fit of plasmon energy according to Stern's theory on 2DES with non-local correction. The dashed blue curve indicates the \sqrt{q} dispersion for non-interacting 2DEG with the same electron density as prepared $\sqrt{3}$ surface. (b) Loss-intensity profile plotted in both cartesian and polar coordinates. The scale of angular coordinate was magnified 3 times for visibility. 48
- 3.12 Sheet plasmon dispersions up to 1.08 ML of silver adatoms. (a) Dispersion of silver film thicknesses from 1 ML to 1.05 ML (b) Dispersion silver film thicknesses from 1.05 ML to 2.08 ML. 51
- 3.13 (a) Photoemission measurements of Ag-doped surface state of Si(111)($\sqrt{3} \times \sqrt{3}$)-Ag. From Ref. [35]. (b) Angle-resolved ultraviolet photoelectron spectroscopy on Ag-doped Si(111)($\sqrt{3} \times \sqrt{3}$)-Ag. From Ref. [36]. 52
- 3.14 Plasmon dispersions up to 4.05-ML silver adatoms. HREELS measurements were performed at various scattering angle ϕ_s with a angular step of 0.5° . (a) Dispersion of 0.37-ML, 0.74-ML and 1.11-ML silver adatoms (b) Dispersion of 1.48 ML, 1.85-ML, 4.05 ML silver adatoms. 54

3.15	Schematic of charge profile in normal direction of surface. (a) Silver single-crystal surface. z_0 indicates the interface of silver and vacuum. The solid curve shows the density variation of free $5s$ electron. The shaded area represents screening effect from $4d$ electrons in terms of $\varepsilon(\omega)_d$. (b) $\text{Si}(111)(\sqrt{3} \times \sqrt{3})$ -Ag surface. z_0 here indicates the interface of silver film and silicon substrate. The light shaded areas show charge profiles of electrons (-) and holes (+), which have the same area to keep surface region electronic neutrality.	57
3.16	Conventional surface plasmon appeared at the deposition of 20-ML silver adatoms. Black arrow (3.9 eV) indicates the conventional surface plasmon.	59
4.1	(a) Graphite lattice. (b) Brillouin zone of graphite.	62
4.2	The π energy band of graphite along several high symmetry direction. The energy dispersion is plotted relative to Fermi level in the low-energy electronic excitations of graphite [48].	63
4.3	building block of graphitic materials. It can be wrapped up into buckyballs (0D), rolled into nanotubes (2D) or stacked into 3D graphite. Figure duplicated from reference[49]	64
4.4	Normalized HREEL spectra of SiC surface and graphene on SiC. The inset shows the LEED pattern of $\text{SiC}(0001)(1 \times 1)$ surface taken at incident electron beam of 80 eV.	69

- 4.5 Sheet-plasmon loss peaks of graphene dispersing with increasing momentum transfer q . The lines in magnified spectra at large momentum transfer ($> 0.5 \text{ \AA}^{-1}$) are smoothed by averaging 3-5 nearest neighbor points. Also the last two spectra (green, brown) with very broad peaks were partially presented in this figure as result of figure layout, but the extensively scanned portions from 2000 meV to 2500 meV were included in data analysis of peak positions. The incident electron beam energy is 20.29 eV. 70
- 4.6 Scattering cross-section intensity varying with q . The angular distribution profile (inset diagram, red line) of loss intensity is strongly peaked around 1.5° to specular direction (green line). Scattering angle ($0^\circ \leq \theta_s < 5^\circ$) is magnified by 3 times in polar coordinates. 72
- 4.7 Plasmon dispersion for graphene of similar charge density, ($E_F = 0.57 \text{ eV}$) $n \sim 2 \times 10^{13} \text{ cm}^{-2}$ and schematic band structures (inset diagrams) show the origin of single-particle excitations SPE (1) intraband and (2) interband. Graphene is ambipolar with, electron and hole carriers in separate π, π^* bands. 74
- 4.8 Plasmon dispersion for Si(111)-($\sqrt{3} \times \sqrt{3}$)-Ag surface-state band ($E_F = 0.19 \text{ eV}$), $n \sim 2 \times 10^{13} \text{ cm}^{-2}$. The schematic band structure (inset diagrams) shows the origin of single-particle excitations SPE 75
- 4.9 Plasmon damping [full-width at half-maximum (FWHM) of loss peak, Fig. 4.5] plotted as a function of momentum transfer q for (G) graphene and (SS) surface-state 2D systems. 79

5.1	(a)SiC(0001) sample with steps; (b)SEM image of terrace on SiC(0001).	82
5.2	HREEL spectra of two layers of graphene on SiC. The spectra at large momentum transfer are smoothed by averaging 5-7 nearest neighbor points for visibility (superimposed lines). The inset shows a splitting of the wavevector $q = 0.068 \text{ \AA}^{-1}$	83
5.3	HREEL spectra of three layers of graphene on SiC. The spectra at large momentum transfer are smoothed by averaging 5-7 nearest neighbor points for visibility (superimposed lines).	84
5.4	HREEL spectra of five layers of graphene on SiC. The spectra of large momentum transfer are smoothed by averaging 5-7 nearest neighbor points for visibility (superimposed lines).	85
5.5	Dispersion behaviors of graphene layer of various thickness	87
5.6	Photoemission images revealing the band structure of (a) single and (b) bilayer graphene along high symmetry directions $\Gamma - K - M - \Gamma$. The dashed (blue) lines are scaled DFT band structure of freestanding films. Inset in (a) shows the 2D Brillouin zone of graphene. From Ref. [81] . .	88
5.7	(a)-(d) The π and π^* bands near E_F for 1-4 graphene layers, respectively. $k_{\parallel} = -1.703 \text{ \AA}^{-1}$ corresponds to the \mathbf{K} point. The dashed lines are from a calculated tight binding band structure, with band parameters adjusted to reproduce measured bands. Red and orange (light gray) lines are for Bernal-type (ABAB and ABAC) stackings, while blue (dark gray) lines are for rhombohedral-type stackings. From Ref. [81]	89

5.8	The loss energy associated with momentum transfer according to the properties of beam energy. The route of transition in band diagram has the same slope. Inset shows the schematic of transition route induced by low energy electron excitation, $\Delta E > \Delta_g$	91
-----	--	----

Acknowledgments

I would like to thank my thesis adviser, Roy Willis, for his invaluable guidance and advice throughout the completion of this work.

I would like to thank my group members: Dr. Kenneth Podolak, Dr. Hyosig Won, Dr. Michael Birke and Dr. Ted Kreutz for experimental assistance in our lab. A special thanks goes to Ken for his extensively copyediting this thesis.

I would like to thank those who have funded my stay at Penn State: Teaching Assistantship of Physics Department and Petroleum Research Fund of American Chemical Society.

I would like to thank all my friends who made my life at Penn State easier thereby I can concentrated on this research for last few years.

I would also like to thank my wife, Min, her love, encouragement, and comradeship kept me on track.

Finally, I am especially indebted to my parents whose love and support made the completion of this work possible.

IN MEMORY OF MY FATHER,

GUANGLIN LIU (1945 - 2007)

Chapter 1

INTRODUCTION

1.1 Plasmons

Plasmons are collective excitation of electrons in a crystal, or on its surface. Plasmons propagate as longitudinal charge density fluctuations through the volume of solids or along its surface. The type of electrons involved in the excitations critically determines the characteristics of plasmons. For a free electron gas in the bulk, The volume plasmon is characterized by a finite plasma frequency $\omega_p = \sqrt{n e^2 / m \varepsilon_0}$ at the vanishing wavevector q and quadratic dependence of dispersion on wavevector in the long wavelength limit:

$$\omega(q) = \omega_p + \frac{3 v_F^2}{10 \omega_p} q^2, \quad (1.1)$$

where $\omega(q)$ is plasmon frequency, v_F is the Fermi velocity, n , e , and m are density, charge and mass of an electron, respectively.

The surface plasmon is a self-sustaining oscillation of the semi-infinite electron gas with a single plane boundary. A reduced surface plasma frequency $\omega_p / \sqrt{2}$ is obtained by applying Maxwell's equation boundary condition at the interface of the bulk and vacuum. The dispersion of the surface plasmon is very sensitive to the charge profile at the surface and bulk electronic properties. For most alkali metals, the surface plasmon

disperses negatively and then positively in a linear mode, due to the charge centroid located on the vacuum side.

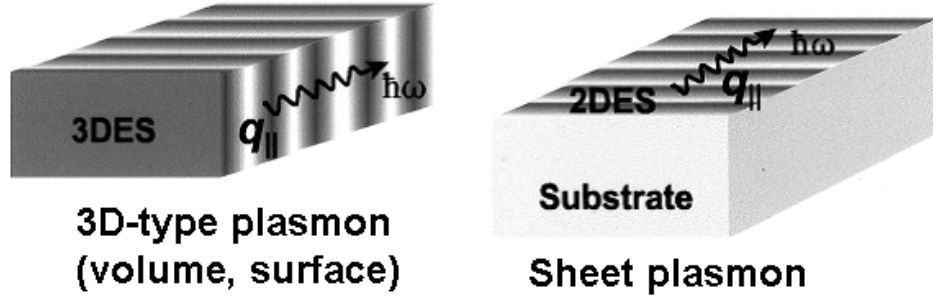


Fig. 1.1. Schematic of 2D- and 3D-type plasmons.

Volume plasmons and surface plasmons are considered to be 3D type because electrons involved in an excitation are free to move in the bulk and underneath the surface. In the real potential of a periodic lattice for the bulk or surface, the band structure has to be considered to calculate the properties of volume and surface plasmons. Meanwhile, the characterizations of plasmons in experiments also provide detailed information of the electronic structures for the bulk or surface. Considerable attention has been attracted in the physics of plasmons. [1, 2, 3, 4]

As shown in Fig. 1.1, the sheet plasmon is a collective excitation locating in a monolayer-thick charge-sheet, and involving only two-dimensionally confined electrons, rather than the excitation of the surface plasmon which involves bulk electrons and extends deeply into bulk. In the view of quantum mechanics, the two-dimensional confinement means electrons can move freely in a plane whereas in the perpendicular direction of the plane, electrons are bound in ground state and isolated from other states due to

their high excitation energy. The dispersion in a sheet of free electron gas is

$$\omega_{2D}(q) = \sqrt{\frac{n_{2D} e^2}{2m \varepsilon_0}} q. \quad (1.2)$$

As $q \rightarrow 0$, $\omega_{2D}(q \rightarrow 0)$, which is the characteristic of sheet plasmon compared to the finite plasma frequency ω_p in 3D-type plasmons. This can be understood in terms of a restoring force between parallel charge wires for sheet plasmons, which is inversely proportional to the spacing λ , shown in Fig. 1.2. However, the restoring force between parallel charge sheets for volume plasmon is constant, irrelevant to the sheet spacing, resulting in a finite energy for the long wavelength limit. The dispersion of sheet plasmon follows \sqrt{q} for the ideal two-dimensional free electron gas.

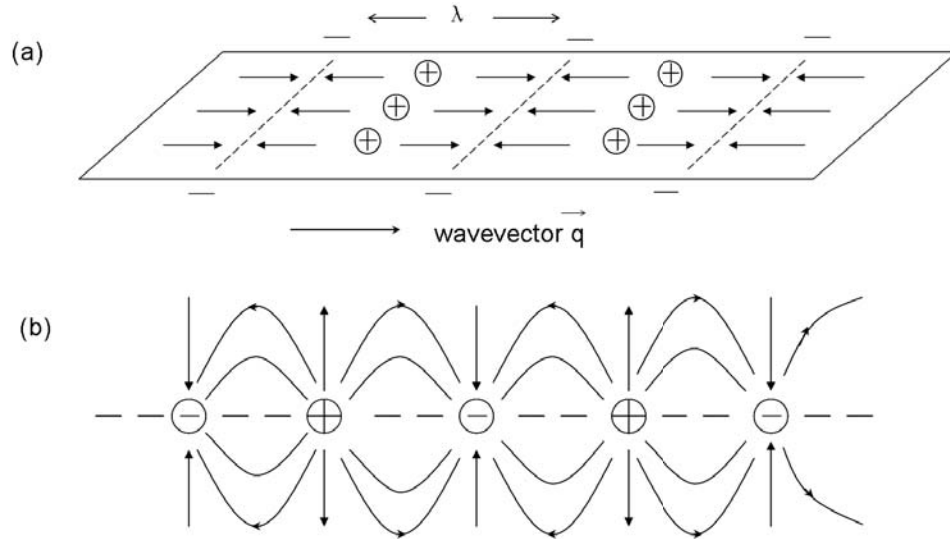


Fig. 1.2. (a) Charge density distribution in a sheet; (b) electric field lines

Three decades ago, sheet plasmons were first observed on the liquid helium surface [5], and in inversion layers of Si-SiO₂ structures [6]. The characterization of dispersion for both systems were limited by structures of both systems and the experimental techniques they employed, where only electron-density-dependent dispersion was characterized with a plasmon energy in the order of 10^{-3} meV for liquid helium surface and 1 meV for the inversion layer of Si-SiO₂. Until recently, a more strictly confined two-dimensional gas system was reported in a silver-induced surface superstructure (Si(111)($\sqrt{3} \times \sqrt{3}$)-Ag) [7]. Moreover a wavevector-dependent dispersion was reported on this surface by using electron energy loss spectroscopy [8]. This novel two-dimensional electron system provides us a playground, also a standard for further study of two-dimensional electron systems that are prepared by various methods.

1.2 Two Dimensional Electron Gas

The sheet plasmon is a unique physical process of a two-dimensional electron system. The properties of two-dimensional electron systems are crucial to the observation of sheet plasmons. Figure 1.3 shows two types of confinement of a two-dimensional electron gas (2DEG). In Fig. 1.3(a), typical for space-charge layer in semiconductor transistor, a triangle potential well is formed by a potential barrier between vacuum and the depletion layer, in energy levels with quantized energies around 20 meV; in Fig. 1.3(b), the schematic of the system we used to sustain sheet plasmons, which consists of a much narrower potential well that is formed by potential barriers between vacuum and the conduction band edge, where quantized energy is about 5 eV while staying away from the thermal excitation energy around 25 meV for room temperature.

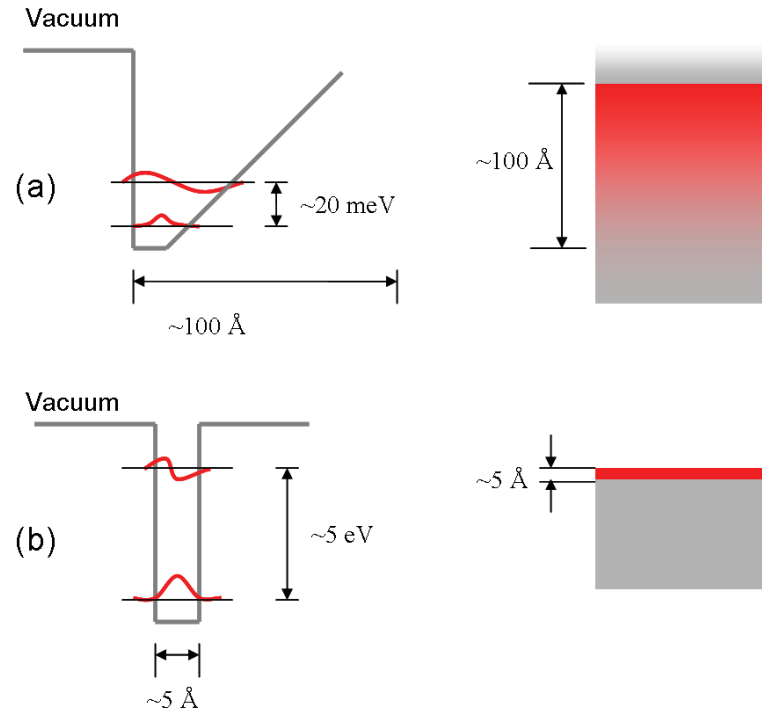


Fig. 1.3. Confinement of electrons in two types of potential well. (a) Triangle potential well in a semiconductor inversion layer, (b) square potential well on the surface of $\text{Si}(111)(\sqrt{3} \times \sqrt{3})\text{-Ag}$ and graphene

Angle-resolved high-resolution electron-energy-loss spectroscopy is the best candidate of tools available to study the dispersion of sheet plasmon, since the excitation by low-energy electrons have a strong advantage to optical experiments in the aspect of momentum transfer. A considerable momentum transfer enables plasmons to enter various regions dominated by different physical processes, e.g. single particle excitation, interband transition.

Si(111)($\sqrt{3} \times \sqrt{3}$)-Ag and graphene are two well-confined, two dimensional systems prepared on a semiconductor surface to study sheet plasmon. Besides superior two-dimensional character, these two systems have their well-studied three-dimensional counterparts, silver crystal and graphite, which provides us benchmarks in a study of their collective behaviors.

Chapter 2

Experimental Setup

2.1 Ultra High Vacuum

The preparation of thin films and surfaces with negligible contamination requires ambient pressure of the order of 10^{-10} torr. Furthermore, much of the analysis of thin films requires similar vacuum conditions. Pressure of this order of magnitude is commonly referred to as ultra high vacuum (UHV) and is typically accomplished in a specially processed stainless steel chamber which is continuously evacuated by a variety of pumps. These pumps are connected to each other in specific order according to their pumping mechanism. A mechanic pump normally brings the pressure to a rough vacuum ($\sim 10^{-3}$ torr), then a turbomolecular pump connecting vacuum chamber and mechanic pump can bring the pressure down further to $\sim 10^{-7}$ torr, which is limited by water vapor pressure absorbed on the wall of chamber at room temperature. UHV will be obtained by following one-day long baking process to desorb water residue from walls. If venting gas has high humidity or the chamber stay in atmospheres for a long time, extra baking time will be required to bring the pressure down to $\sim 3 \times 10^{-8}$ torr. At the last stage of baking, equipments with filaments are powered on for degassing. When chamber cools down, the resulting pressure typically goes down to $\sim 10^{-10}$ torr.

2.1.1 UHV Chamber

The UHV chamber is commonly made of stainless steel due to its desirable properties: mechanically strong, machinable, weldable, effectively outgassing by baking. The ports on UHV chamber are sealed with CF (ConFlat) flanges, and instruments or view-ports are installed through these ports in the walls of the chamber. The seal mechanism is a knife-edge that is machined below the flat surface of flanges. As the bolts of a flange-pair are tightened, the knife edges make annular grooves on each side of a soft metal gasket. The extruded metal fills all the machining marks and surface defects in the flange, yielding a leak-tight seal. The CF flange seals operate from atmosphere to 10^{-13} torr, and within the temperature range from -196°C to 450°C .

2.1.1.1 Pumps

In order to evacuate a chamber or keep UHV pressure, pumps must be operating continuously. There are four kinds of pumps used in our UHV system. Mechanical Rotary Pumps prepare a roughing vacuum and keep fore-vacuum stage for the turbomolecular pump. Turbomolecular pump is the primary pump to obtain and maintain UHV. Ion pump maintains UHV after the turbomolecular pump turns off so that vibrations that are created by the turbomolecular pump are reduced. Titanium sublimation pumps are typically used as an effective way to pump hydrogen in UHV and boost pumping speed at a large gas load.

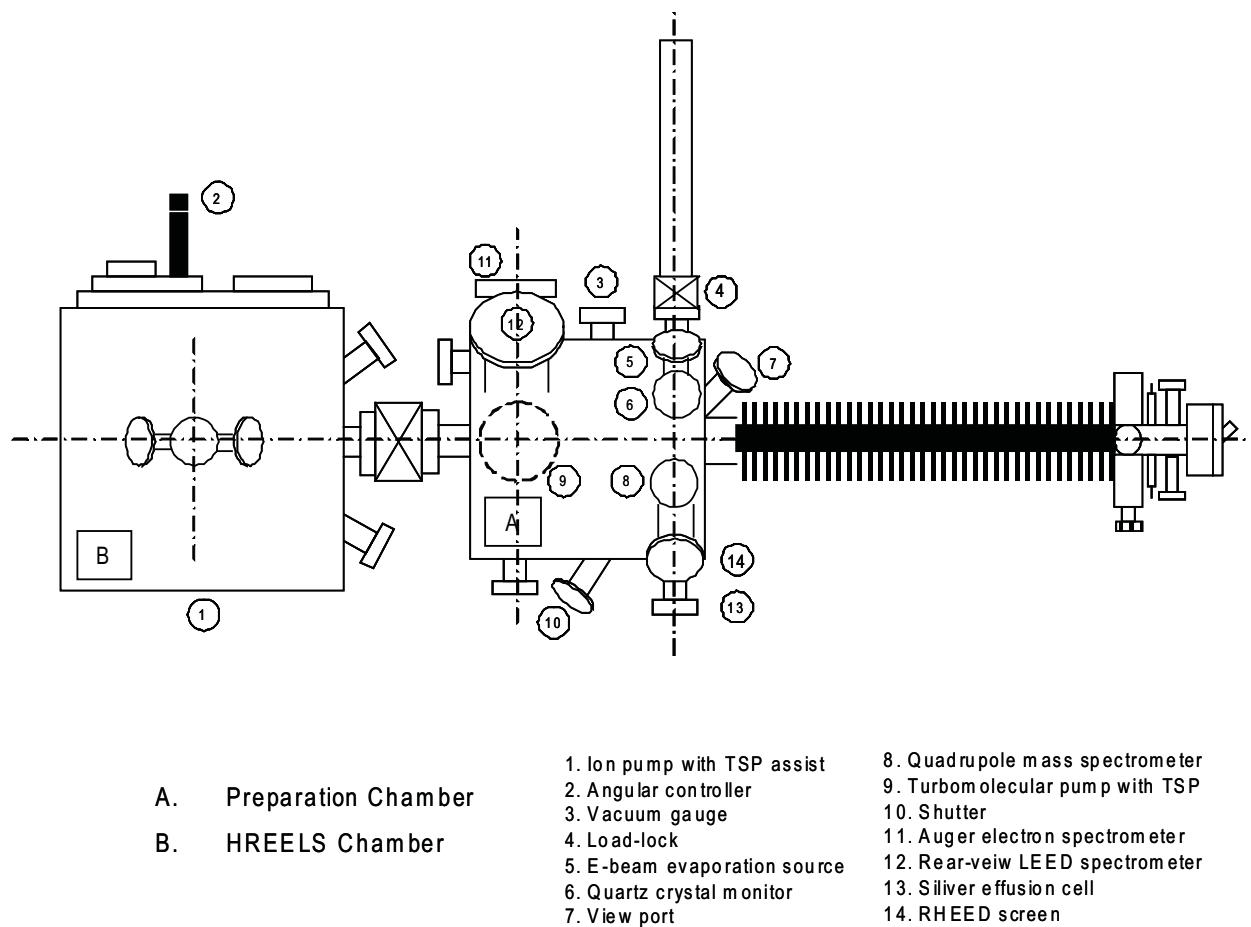


Fig. 2.1. A top view of UHV system in this thesis research.

2.1.1.2 Preparation Chamber

The preparation chamber is connected with HREELS chamber through a 6" inch gate valve. When sample preparation is in progress, the gate valve is close to prevent evaporation-material vapor from contaminating the coated surface of spectrometer. The primary function for this chamber is thin film preparation, as its name suggests. The base pressure after bake-out is $\sim 2 \times 10^{-10}$ torr, and achieved by a turbomolecular pump and a titanium sublimation pump. The layout of this chamber is quite flexible and can be arranged to fulfill various experimentations. There are several evaporators installed on this chamber including effusion cells for Ag, In, Mn; a DC magnetron sputtering gun for Si; and a crucible for C_{60} . Two XTC crystal monitors are to provide thickness information for different thin-film evaporation sources. The characterization tools are AES-LEED and RHEED to check surface cleanness, structures, film thickness of layer-by-layer growth. The surface can be bombarded with a sputter ion gun. A 4 feet long sample manipulator with five degrees of freedom, capability of heating and cooling is sealed with chamber through a long UHV bellow. A sample holder is installed on the stage of manipulator according to the method for heating process, i.e. resistive heating and electron bombardment heating.

2.1.1.3 HREELS Chamber

The HREELS chamber is used exclusively for housing the HREEL spectrometer. It can keep a working pressure of 8×10^{-11} torr by ion pump only. No deposition equipment is installed in this chamber for protecting the coated surface of the spectrometer.

2.1.2 Quadrupole Mass Spectrometer

The quadrupole mass spectrometer is a multi-purpose instrument in surface science and semiconductor fabrication. It has the following applications: leak detection, virtual leaks or desorption, outgassing studies, process gas monitor and control. The quadrupole consists of four parallel metal rods. Each opposing rod pair is connected together electrically and a radio frequency voltage is applied between one pair of rods, and the other. A direct current voltage is then superimposed on the R.F. voltage. Ions travel down the quadrupole in between the rods. Only ions of a certain mass-to-charge ratio m/z will reach the detector for a given ratio of voltages: other ions have unstable trajectories and will collide with the rods. This allows selection of a particular ion by varying the voltage.

2.2 Electrons as a Tool for the Characterization

Electrons with energies ranging from a few eV to several thousand eV have very small penetration depth. The dominant electron energy loss mechanism in solids is the excitation of valence band electrons whose electron density is nearly constant. Because of this fact, a universal curve for the inelastic mean free path of an electron versus its kinetic energy is plotted in Fig. 2.2. Electrons with kinetic energy of 100eV have a mean free paths around (5Å), which is just several monolayer thickness. This shallow probing depth of electrons make them an indispensable tool for characterizing electronic

properties of the surface and for ultrathin film. The High-Resolution Electron-Energy-Loss Spectrometer (HREELS) is built based on this nature of electrons and extensively employed in the research of this thesis.

Another important application of electrons in characterization is structural analysis. Electrons are diffracted by the lattices of a surface or solid as the wavelength of electrons is comparable with the interatomic distances. The various long range order for a surface or solid can be identified by a pattern projected by diffracted electrons. We use Low Energy Electron Diffraction (LEED) and Reflection High Energy Electron Diffraction (RHEED) to monitor the process of surface treatment and ultrathin-film growth.

2.2.1 HREELS

Electron energy loss spectroscopy using low energy electrons was first applied to study surface vibrations of adsorbates on W(100) surface. In 1970, loss spectroscopy study on surface phonon excitation of semiconductor surface was reported [10]. As the technique has been developing steadily, the instrumental resolution improve greatly and enabled its application in a wide variety of areas in surface physics and chemistry. The ever increasing field of loss spectroscopy has been dealt with in review articles [11, 12], conference reports [13], and books [14].

2.2.1.1 Instrumentation

The HREELS is highly sophisticated instrumentation because the excitation energy and linewidth of plasmon span the range of 10 meV up to 10 eV. Therefore, not

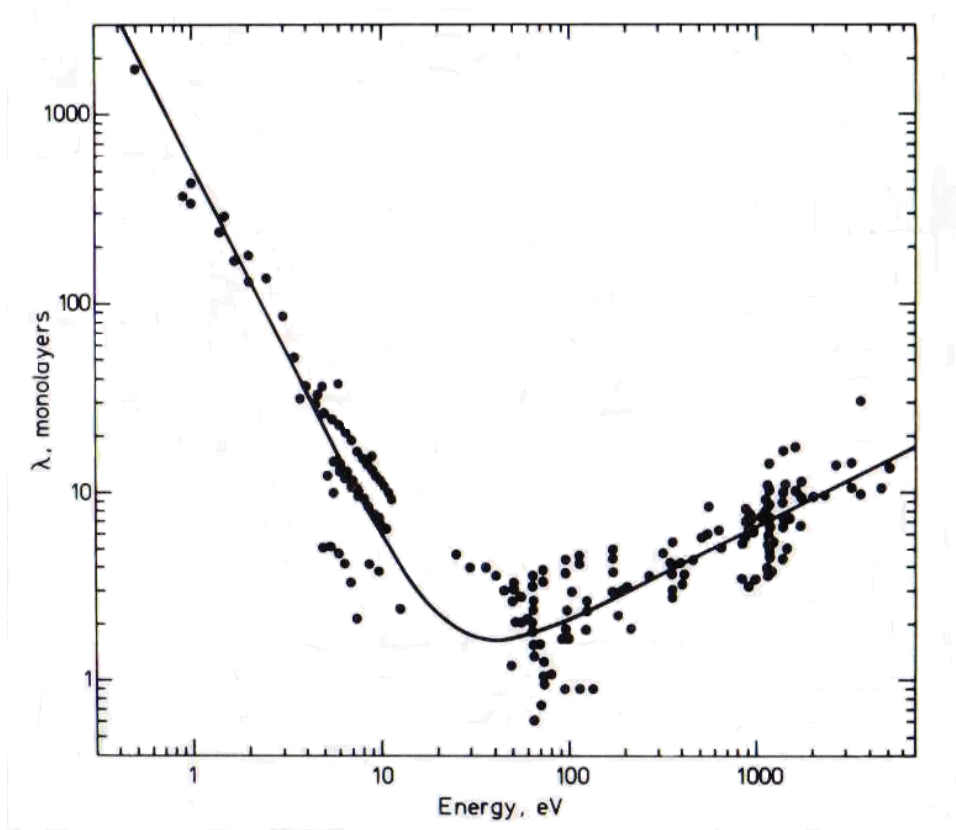


Fig. 2.2. The mean free path λ of electrons in solids as a function of their energy. This is curve also called the "universal curve" for the probing depth of electrons into solids; this is a compilation of experimental data for a large variety of materials and energies [9].

only must the analyzer be capable of high-energy resolution, but also the incident beam must be highly monochromatic. Since no physical source of electron emission can provide such a monoenergetic electron beam with a narrow energy distribution, the spectrometer must use electron optical devices as energy filter following an electron emitter. A schematic diagram of a complete spectrometer is shown in Fig. 2.3. Electrons emitted from thermionic cathode (filament: LaB_6) are directed by groups of lenses and filtered by both rough and fine monochromators before the electrons interact with sample which is grounded to prevent charge accumulation. The reflected electrons scattered from sample surface are collected by a angle-resolving analyzer which is composed of monochromator and channeltron multipliers for counting electrons in each energy channels. High energy resolution (≤ 10 meV) can only be obtained when electrons pass the monochromator at low kinetic energies. However, the potential difference of the spectrometer surface due to the work-function differences of various materials may pose a severe problem. The electrons energy may not be accurately controlled because they are interfered by the potential difference. In order to overcome this problem, any surfaces directly or indirectly exposed to electron beam are uniformly coated with graphite due to its excellent conductivity. Two cylindric envelopes made of Mu-metal are used to isolate spectrometer from any stray magnetic field.

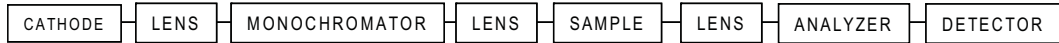


Fig. 2.3. A block diagram of the HREEL spectrometer.

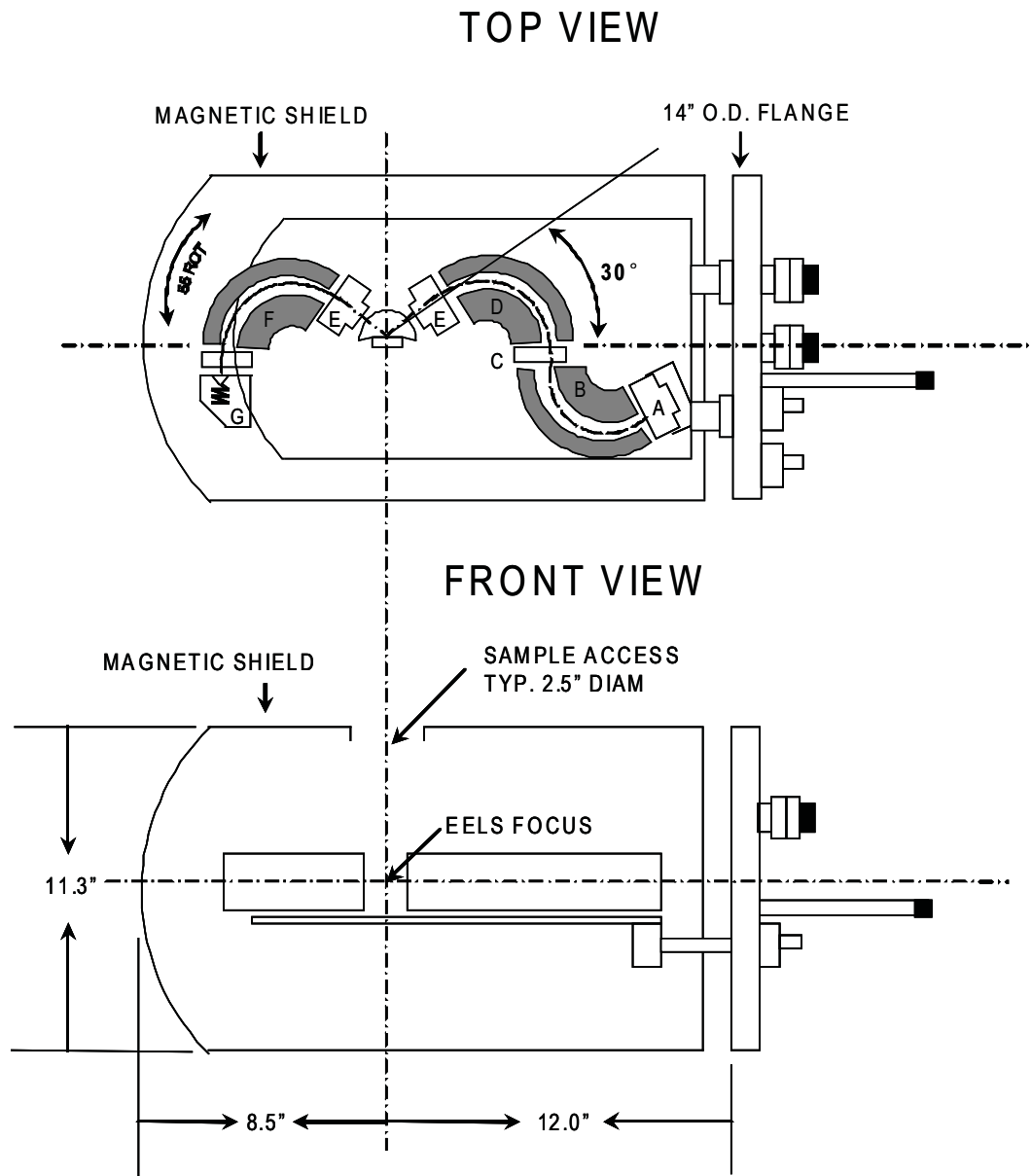


Fig. 2.4. the schematic of HREELS (LK2000-14-R)

LK2000-14-R HREELS spectrometer consists of two monochromators and one analyzer which are all a type of electrostatic deflector. As show in Fig. 2.4, three 127° cylindrical deflector are designed to generate a monoenergetic electron beam and to analyze scattered electron at an angle. The passing energy of deflectors are determined by voltage applied across inner and outer plates. An electron with mass m and velocity v in the deflecting field ε between the inner and the outer plates travels along the center path when electrostatic force is equal to centripetal force:

$$mv^2/r = 2E_0 = e\varepsilon, \quad (2.1)$$

where r is the radius of center path, E_0 the energy of incident electron. The electric field ε is determined by the potential difference ΔV across the inner and the outer plates with radii of curvature a and b respectively. we have:

$$\varepsilon = \frac{\Delta V}{\ln(b/a)r}. \quad (2.2)$$

Then combining Eqn. 2.1 we have:

$$E_0 = \frac{e\Delta V}{2\ln(b/a)}. \quad (2.3)$$

The energy resolution $\Delta E_{1/2}$ is approximately evaluated by [14]:

$$\Delta E_{1/2}/E_0 = \Delta s/r \quad (2.4)$$

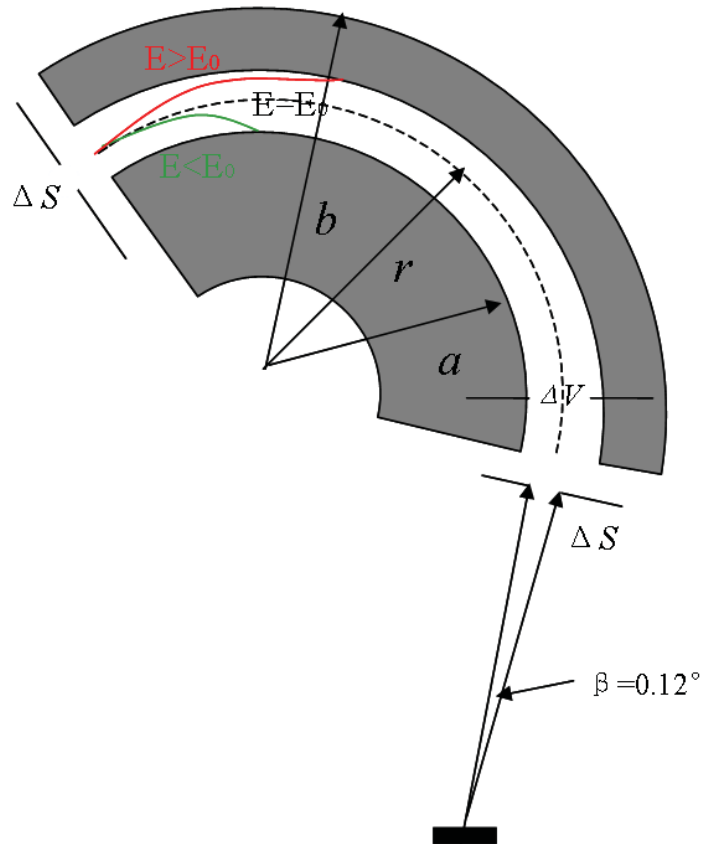


Fig. 2.5. monochromator is composed of two 127° cylinders with radius $a = 3$ cm and $b = 4$ cm respectively, the electrons with energy $E_0 = e \Delta V / 2 \ln(a/b)$ traverse along center path through monochromator. Accordingly, electrons with energy other than that terminated their trajectory either at outer plate ($E > E_0$) or inner plate ($E < E_0$)

where Δs is the width of slit. In our experiments, the passing energy E_0 was set 3 eV, Δs of fine monochromator and analyzer are both equal to 1 mm. Based on Eqn. 2.4, the resolution $\Delta E_{1/2}$ of each system is 6 meV each. The system resolution will be the convolution of those two, which results in:

$$\Delta E_{total} = \sqrt{\Delta E_{mono}^2 + \Delta E_{ana}^2}. \quad (2.5)$$

So ΔE_{total} is 8.5 meV. If angular factors are taken into consideration, the system resolution is 9.48 meV which is given by the manufacturer and used in the data analysis of this work.

2.2.1.2 Dipole Scattering

There are mainly two electron scattering mechanisms which give rise to electron energy losses, i.e. dipole scattering and impact scattering. In this work, the physical process of interaction of electrons and samples is dipole scattering.

The dipole scattering is often a dominant contribution to the inelastic electron scattering cross section. The oscillating component of the electric dipole moment sets up an electric field in the vacuum above the surface and these oscillating electric fields scatter the incident electron inelastically. The induced dipole field is long ranged. Figure 2.2.1.2 shows the electric field in dipole scattering scheme. For a dipole placed just above the metal surface, the potential seen by an electron in the vacuum above the surface is,

$$V(\mathbf{r}) = \frac{2pz}{r^3} e^{-i\omega_0 t}, \quad (2.6)$$

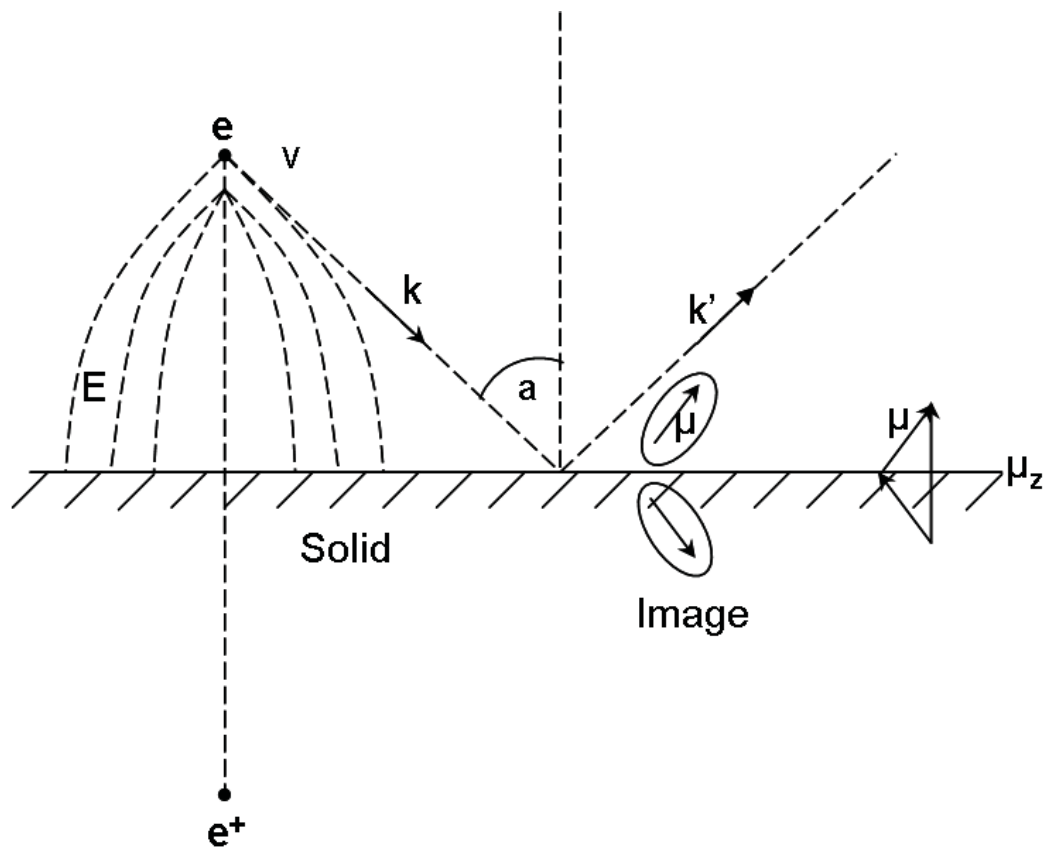


Fig. 2.6. Electric field in dipole scattering

where p is the Z axis component of electric dipole moment, \mathbf{r} is the displacement, ω_0 is oscillating dipole frequency. The Eqn. 2.6 can be rewritten by introducing q_{\parallel} , i.e.

$$V(\mathbf{r}) = \frac{pe^{-i\omega_0 t}}{\pi} \int d^2 q_{\parallel} e^{i\mathbf{q}_{\parallel} \cdot \mathbf{r}_{\parallel}} e^{-q_{\parallel} z} \quad (2.7)$$

which shows the potential decomposed into a linear combination of two dimensional waves localized near the surface. The component of wave vector q_{\parallel} has a field which extends into the vacuum a distance $l(q_{\parallel}) = q_{\parallel}^{-1}$. Consequently, the long wavelength contributions to the potential must extend far into the vacuum to satisfy Laplace equation ($\nabla^2 V = 0$) at the surface.

This long range potential also results in the scattering cross section, which is peaked strongly around the specular direction. This key feature can be used to experimentally distinguish dipole scattering from other scattering processes by measuring the angular distribution of inelastically scattered electrons.

Consider an incident electron with kinetic energy E_i . After inelastic interaction, the scattered electron has energy $E_s = E_i \pm \hbar\omega_0$. The excitation cross section is a maximum roughly at $\hbar\omega_0/E_i$ [15] and sharply concentrated into a lobe of angular width about 1° to 3° . Under usual experimental conditions, $\hbar\omega_0 \ll E_i$, the electric dipole scattering mechanism produces a narrow angular distribution profile. For instance, $E_i = 5$ eV, $\hbar\omega_0 = 100$ meV, then the angle to the specular direction is $\theta_s = 0.6^\circ$. For the analyzer in our spectrometer, the acceptance aperture is around 0.2° and angular resolution of rotation is 0.5° which are sufficient to resolve the angular distribution of scattered electrons. The loss intensity $I(\omega)$ is related to the microscopic dielectric function $\varepsilon(\omega)$ has

a fairly simple form

$$I(\omega) = \frac{2|R_i|^2\sqrt{(1-2\vartheta_E)}}{a_0k_i\cos\theta_i}\frac{1+n(\omega)}{\hbar\omega}\text{Im}\left\{\frac{-1}{1+\varepsilon(\omega)}\right\}, \quad (2.8)$$

where $|R_i|^2$ is the reflectivity, a_0 is the Bohr radius, ϑ_E is $\hbar\omega/E_i$, k_i and θ_i are the momentum and the incident angle of the incoming electrons respectively, and $n(\omega)$ is the Bose factor.

2.2.1.3 Impact Scattering

In the last section, dipole scattering due to a long-range interaction was introduced. A second mechanism, involving short range interactions, is impact scattering, first observed by Ho et al. in the vibrational modes of hydrogen terminated W(100) surface [16]. In their experiment, loss structure was reported when the electron analyzer was rotated away from the specular direction in Fig. 2.7. The scattering event in this case occurs at very small distances and gives rise to completely different characteristics to dipole scattering. In contrast, instead of sharply peaked angular distribution profile due to dipole scattering, impact scattering produces a spreading angular profile. The theoretical description of impact scattering requires detailed knowledge of the electron scattering potential.

2.2.2 LEED

LEED is one of most common surface science techniques used in studies of crystalline surfaces. It probes the long range order of periodic surface structures. Electron

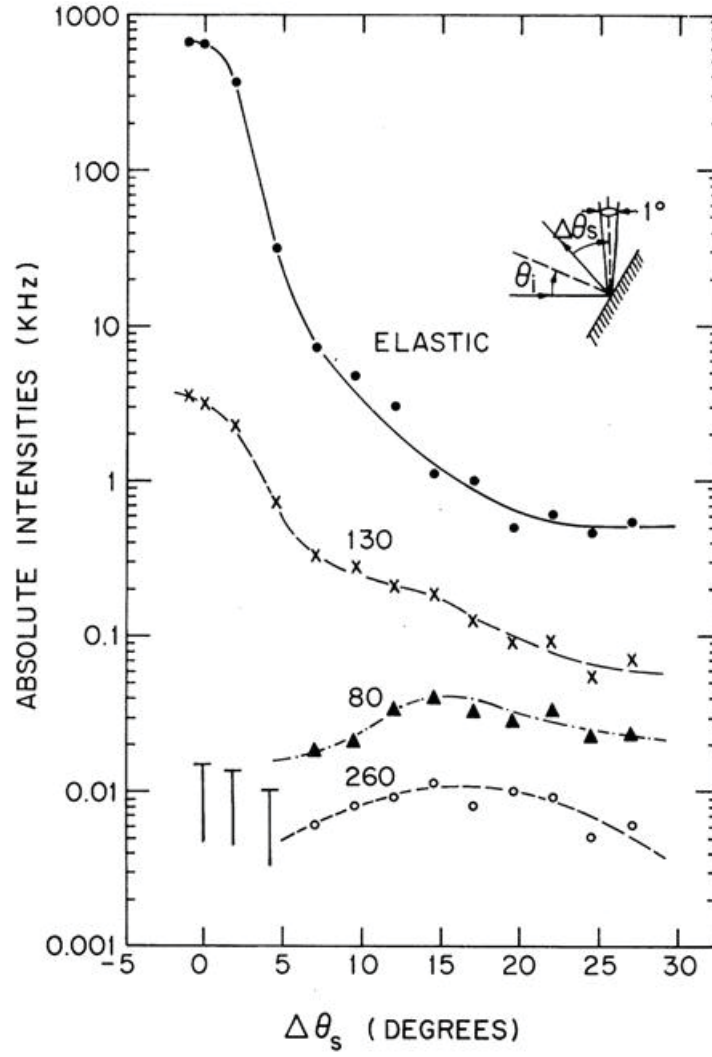


Fig. 2.7. Angle dependence of the absolute intensities as a function of the collection angle $\Delta\theta_s$. The scattering geometry is shown in the upper inset. Vibrational modes at 80 and 260 meV are only observed in the off-specular spectra, which are excited via the impact scattering mechanism. Figure from reference [16]

diffraction from crystalline surfaces was first discovered by Davisson and Germer in 1921. The interference phenomena of electrons scattered by crystals is closely related to the development of quantum mechanics as its experimental verification of de Broglie's hypothesis $\lambda = h/p$ (h Planck's constant).

Electron diffraction arises from the constructive and destructive interference of the electron wave that is elastically scattered from a surface potential. A simple kinematical model of LEED based on the Laue x-ray diffraction model can be used to derive many of useful formulas. The periodic arrangement of atoms in two dimensions can be described by a unit cell, which is defined as the smallest parallelogram such that the lattice can be constructed by translation operations. Basis vectors (\mathbf{a}_1^* , \mathbf{a}_2^*) of a complementary

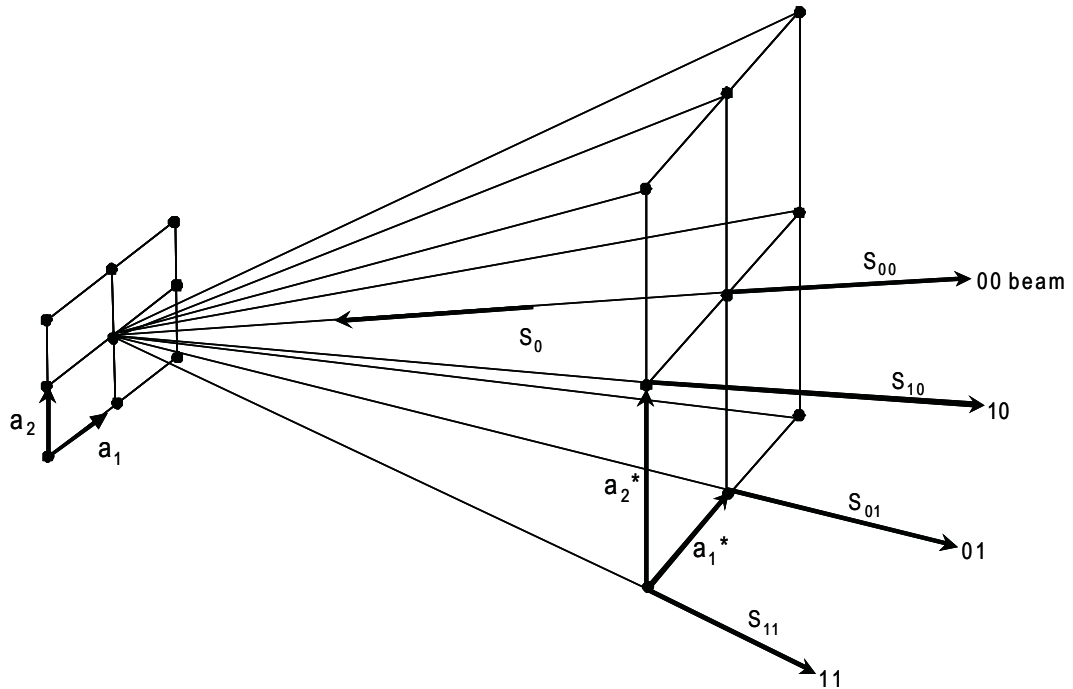


Fig. 2.8. The principle of the formation of a diffraction pattern in a LEED experiment.

reciprocal lattice is defined by the basis vectors ($\mathbf{a}_1, \mathbf{a}_2$) obeying the equations

$$\mathbf{a}_i \cdot \mathbf{a}_j^* = \delta_{ij} (i, j = 1, 2), \quad (2.9)$$

where δ_{ij} is Kronecker symbol. $\delta_{ij} = 0$ if $i \neq j$, and $\delta_{ij} = 1$ if $i = j$. The principle underlying the LEED experiment is illustrated schematically by Fig. 2.2.2. The direction of the incident primary electron beam is characterized by the unit vector \mathbf{s}_0 , and the directions of interference maxima are given by a set of unit vectors \mathbf{s} , which are determined by the following Laue conditions:

$$\begin{aligned} \mathbf{a}_1 \cdot (\mathbf{s} - \mathbf{s}_0) &= h_1 \lambda \\ \mathbf{a}_2 \cdot (\mathbf{s} - \mathbf{s}_0) &= h_2 \lambda \end{aligned} \quad (2.10)$$

(h_1, h_2 are integers). If we let $\Delta \mathbf{s} = \mathbf{s} - \mathbf{s}_0$, then the Equ. 2.10 can be rewritten as

$$\frac{\Delta \mathbf{s}}{\lambda} = h_1 \mathbf{a}_1^* + h_2 \mathbf{a}_2^*. \quad (2.11)$$

which shows that the directions of the interference maxima are determined by the 2D vectors of a 2D reciprocal lattice. In LEED experiments the directions of the scattered beams are given by the points where they intersect with the fluorescent screen giving rise to the diffraction spots. As a consequence, the observed diffraction pattern is a direct representation of the reciprocal lattice of the surface. The electron wave length can be simply calculated by $\lambda_e = \sqrt{150/E_i}$, where λ_e is electron wave length in unit of

angstrom and E_i is the kinematic energy of electrons in unit of eV. A typical 100 eV electron beam has a wave length of 1.2 Å which in the order of lattice constant ($1 \sim 3$ Å). A schematic of LEED system is shown in Fig. 2.9.

In this work, the LEED pattern is primary characterization tool to identify surface superstructure in our preparation precesses. The sharpness of diffraction spots is also one of tools for cleanness just by easy eye-check, diffuse spots indicate contaminants which show up in surface-adsorbates-sensitive energy loss spectroscopy.

2.3 Physical Vapor Deposition

Thin films may be prepared by several different techniques, e.g. physical vapor deposition (PVD), chemical vapor deposition (CVD), electrochemical deposition. In the category of PVD, if sorted by the method of vaporizing material source, there are three sub-category of vacuum depositions, i.e. thermal evaporation, sputtering, pulsed laser deposition. However, all these methods are physical processes only, rather than any chemical reaction at the deposited surface such as in CVD. According to the way of vaporized material condensations onto surface, there are three primary growth modes, Frank-van der Merwe (FM layer-by-layer), Stranski-Krastanov (SK layer-island) and Volmer-Weber (VW island). These growth mode are determined by the properties of both deposited material and substrate surface.

The preparation chamber is capable of being set up to perform almost all of these processes. In this work, electron bombardment heating is used to evaporate the pure metal material in effusion cell with vapor output aperture aligned with sample surface. With effusion cell, the deposited area is limited to sample area only and chamber pressure

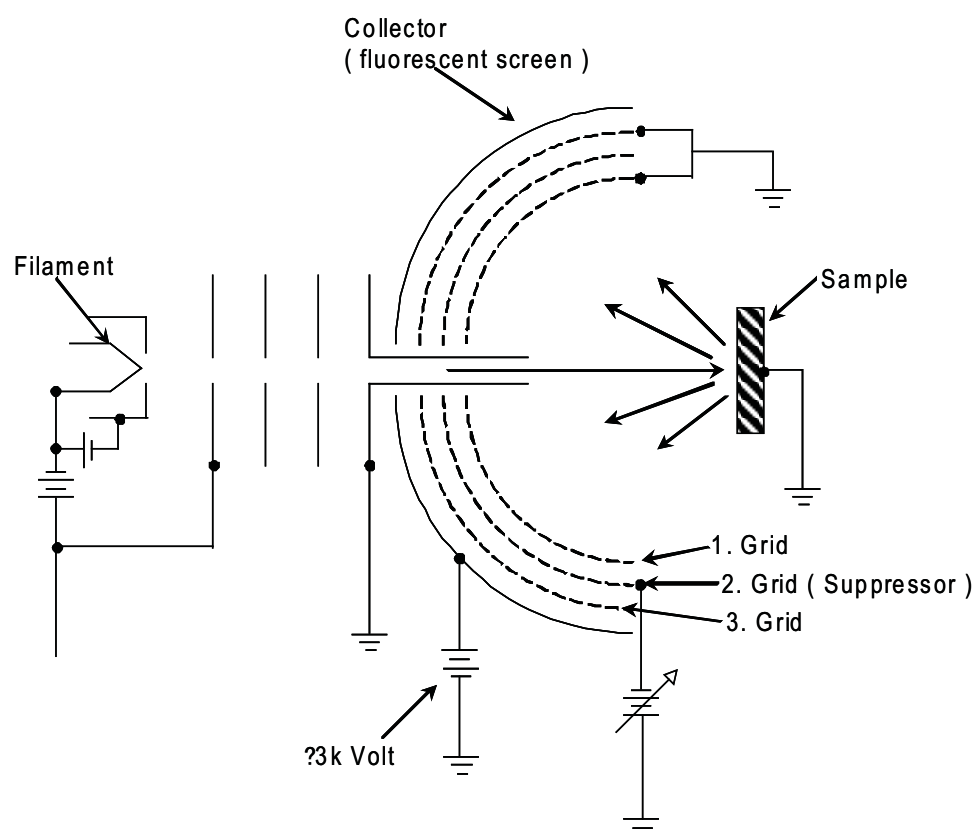


Fig. 2.9. LEED schematic

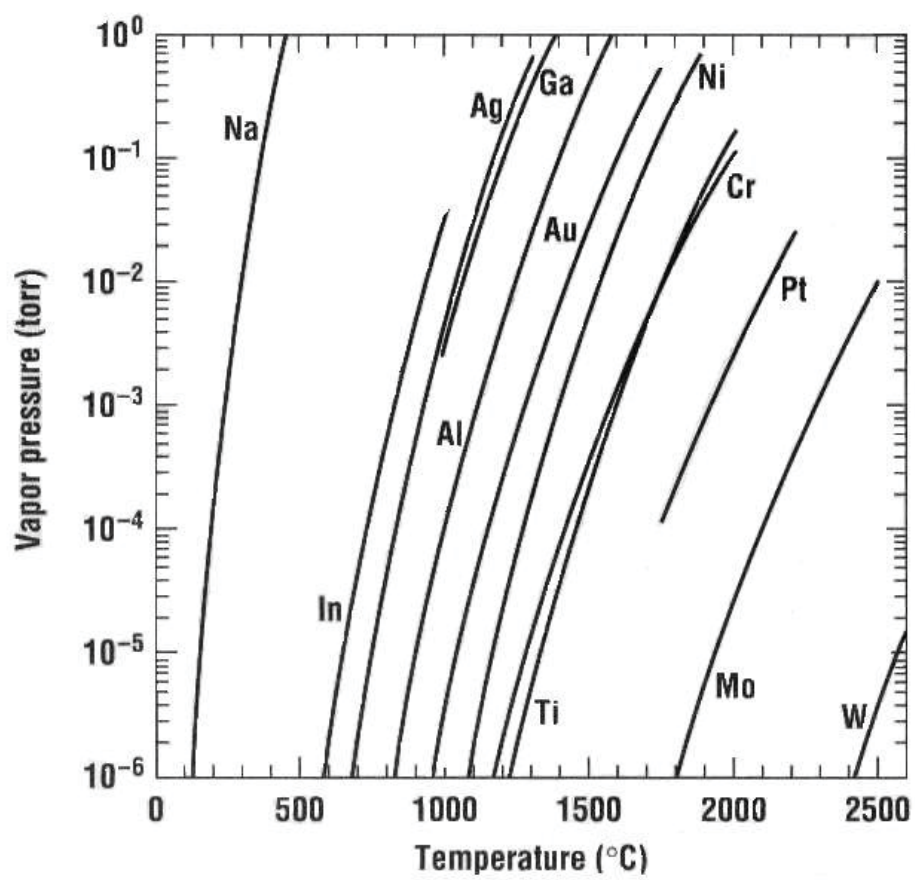


Fig. 2.10. Metallic vapor phase diagram.

can keep low at deposition since metal vapor pressure is restrained inside the effusion cell. An equation can be derived under the assumption that the particle current density is conserved in deposition process. If F is the flux composed of atoms with mass m at the equilibrium pressure $P(T)$ in the cell at temperature T , one obtains

$$F = \frac{P(T)A}{\pi L^2 \sqrt{2\pi m k T}} \quad (2.12)$$

where L is the distance between cell aperture and substrate surface, and k is Boltzmann's constant. To obtain a reasonable deposition rates ($0.1 \sim 1 \text{ \AA/s}$), the equilibrium pressure $P(T)$ is around 10^{-2} torr for noble metal and the corresponding evaporation temperature needs to be higher than 1000° C from vapor phase diagram in Fig. 2.10. At this high temperature, metal caps around cell and electron emitter (thoriated tungsten filament) are used as radiation shield.

The deposition rate is monitored by quartz crystal oscillator which is able to move into the front of sample surface for more accurate measurements. The deposition rates signal is also sent to a power supply to form a negative feedback for automatical mode. A shutter between the cell and sample is also installed for manual control. Alternatively a electron beam power supply embedded with temperature negative feedback can be also used to control the flux off effusion cell.

2.4 Silicon Wafer Processing

Silicon as the basic material of microelectronic industry attracts tremendous research focus in last two decades. Benefited from those research discovery and innovation,

current silicon-based electronic advance to a mature industry involved a variety of techniques and process. In this work, clean and thermal treatment processes are required to prepare silicon wafer as a qualified substrate.

2.4.1 Cleaning

The ideal goal of cleaning is to remove all impurities from a surface. There are three types of impurities often existing on the surface, including organic residues, metallic particles and oxides. A series of baths for immersion of wafers, named RCA clean, are preformed to attack contaminants before introducing into vacuum. The solutions with composition and function are list in the Tab. 2.1.

Table 2.1. Solutions of RCA cleaning of silicon wafer

Solutions	Composition	Volume Ratio	Temperature	Remark
SC1	$NH_4OH/H_2O_2/H_2O$	1:1:5	80°C	Organic residues
HF	HF/H_2O	1:50	20°C	Chemical oxide
SC2	$HCl/H_2O_2/H_2O$	1:1:6	80°C	Metallic contaminants

After RCA cleaning, a wafer will be blown dry by nitrogen gun. As the clean silicon surface is very active and easily reacts with oxygen in ambient air, a thermal treatment in ultra high vacuum is required to remove any thin oxide layer from surface.

2.4.2 Thermal Treatment

Thermal treatment of silicon wafer is an indispensable process for both silicon substrate preparation and metallic thin film deposition. The two major obstacles need to overcome are undesired diffusion and non-uniform heating. In the work of metallized

silicon surface, a special wafer holder is designed and built to handle the silicon wafer based on dozens of tests. To reducing the diffusion from electrodes at high temperature and thermal gradient from contacts between electrodes and sample, the tantalum electrodes buffered with chips from the same wafer disk are used in the resistive heating, and this buffer chips also spreads electric current uniformly into sample since the inevitable point contact between electrode and wafer surface, creating a thermal gradient. To prevent other source of contaminants, the surface whose temperature thermal radiation from the heated sample may raise high is covered with low-vapor-pressure molybdenum foil. A fast response power supply is used to limit passing current after sample is breakdown which may be assisted by a heater underneath the sample shield for a low doping silicon sample.

The temperature is measured by pyrometer at high temperature and power output at low temperature with a calibration from a on-sample thermocouple measurement from a sacrificed sample used for the calibration. The emissivity of surface measured by pyrometer is also experimentally determined by calibrating from the thermocouple measurement.



Fig. 2.11. The holder for heating silicon wafer.

Chapter 3

Plasmon Dispersion of Reconstructed Silicon Surfaces

In the work of this chapter ¹, the sheet-plasmon behavior on Si(111)($\sqrt{3} \times \sqrt{3}$)-Ag surface superstructures was studied by HREELS. In the initial stage of silver-adatom deposition, charges transfer from the silver adatoms to surface states of Si(111)($\sqrt{3} \times \sqrt{3}$)-Ag until reaching a critical coverage $\theta_c \sim 0.03$ ML, the variation in electron density was brought out in the blue shift of the plasmon energy. Further deposition of silver adatom induced silver micro-crystal and morphology effect which alter the plasmon dispersion, where a plasmon transition from 2D type to 3D type was also observed.

Silicon, with its indispensable role in microelectronics, has always been a major research target both in academic and industrial lab. In the area of surface science, surface reconstruction and induced surface superstructure attract much attention because lack of symmetry in a direction normal to the surface and reconstructed periodic atomic arrangements produce a variety of properties different to that in bulk. In addition to superstructures formed on clean surfaces, more than 300 kinds of adsorbate-induced surface superstructures have been found on silicon [18].

Of particular interest for two-dimensional electron systems, two reconstructed silicon surfaces [Si(111)(7×7) and Si(111)($\sqrt{3} \times \sqrt{3}$)-Ag] were prepared and studied by exciting plasmons with low energy electrons. Si(111)(7×7) is the precursor in preparation

¹ Part of this work was briefly published in Ref. [17]

of Si(111)($\sqrt{3} \times \sqrt{3}$)-Ag, and the unique electronic properties of Si(111)($\sqrt{3} \times \sqrt{3}$)-Ag is closely related to both surface and electronic structures of Si(111)(7×7).

3.1 Si(111)(7×7)

3.1.1 Atomic and Electronic Structure of Si(111)(7×7)

The Si(111)(7×7) surface is one of the most studied systems in surface science and has borne a controversy of its atomic arrangement for more than two decades before dimer-adatom-stacking fault (DAS) structure was firstly brought out [19]. Fig. 3.1 shows the DAS structure of Si(111)(7×7) and empty state STM image. The unit cell of Si(111)(7×7) has corner holes connecting each other by chains of dimers and contains two triangles separated by the dimer chains. Each triangle has six adatoms and three rest atoms, arranged locally in a 2×2 periodicity. In DAS structure, there are totally 19 dangling bonds, which is much less than 49 unpaired electrons on an unconstructed Si(111) surface. This results in a decrease of the total energy, which was theoretically estimated to be ~ 0.4 eV lower than unrelaxed surface [20].

In bulk silicon, an energy gap (~ 1.1 eV) opens up between conduction band and valence band. However, on the surface of silicon, the missing covalent atoms on the vacuum side of topmost atomic layer on surface, lead to dangling bonds which have an energy level within silicon bulk band gap to form surface electronic states. On Si(111)(7×7) surface, energy levels of those dangling-bond states are located around the middle of the bulk band gap. In experiments of angle-resolved ultraviolet photoelectron spectroscopy (ARUPS), surface-state bands were detected and shown in Fig. 3.2 [21]. The surface

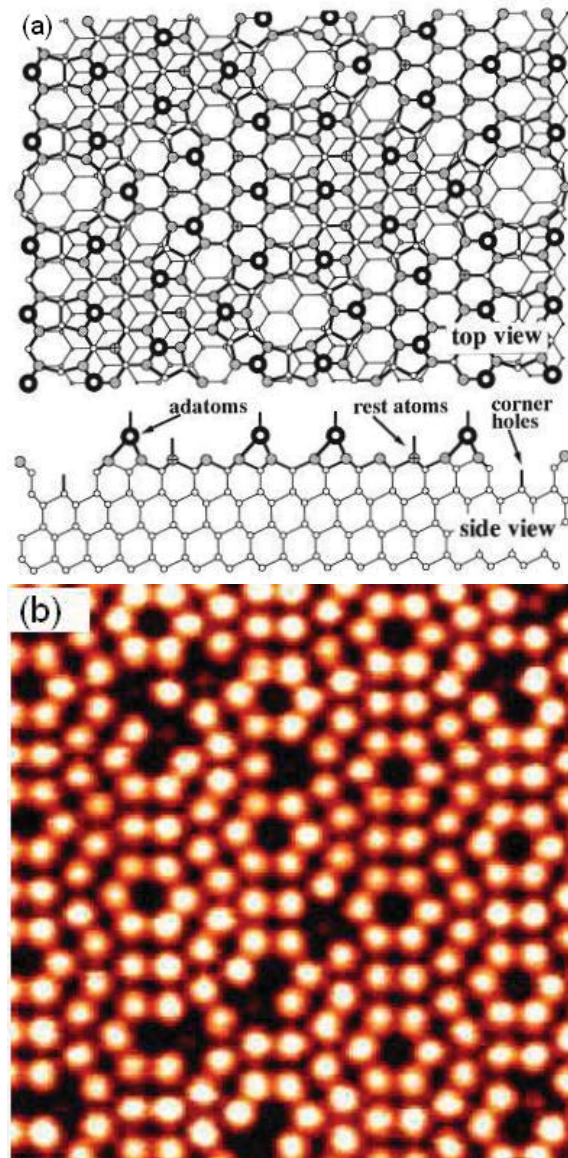


Fig. 3.1. Atomic structure of Si(111)(7 \times 7). (a) Schematic of atomic arrangements; (b) STM image, from Omicron Inc.

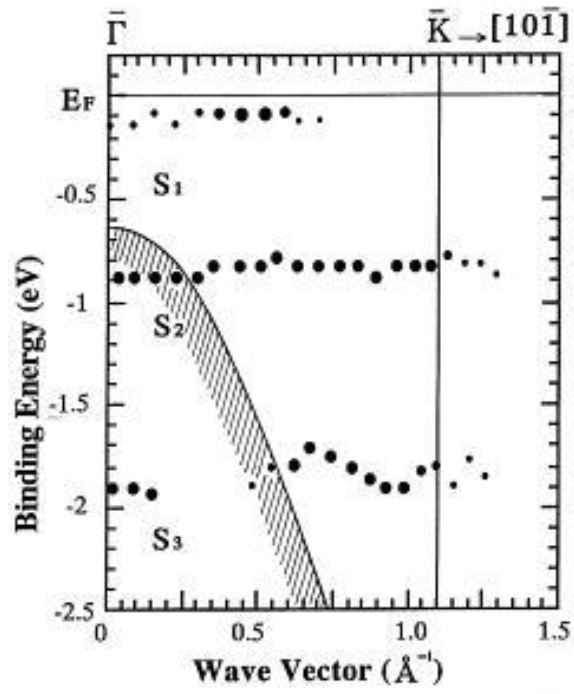


Fig. 3.2. Two-dimensional band-dispersion diagram for Si(111)(7 × 7) clean surface measured by ARUPS [21]

state (denoted by S_1 in Fig. 3.2) is always detected at the Fermi Level (E_F) and its high density of state results in "Fermi-level pinning". The metallic properties of Si(111)(7×7) is also due to surface state straddling the Fermi-level [22]. Another important feature in band diagram is that the surface state S_1 is non-dispersing due to the non-overlapping nature of dangling bonds: p_z -like orbitals and its localization.

3.1.1.1 Sample preparation

Samples were cut from commercial-manufactured Si(111) wafers including both p-type and n-type bulk doping. Before introducing into ultra-high vacuum, samples were chemically cleaned to remove organical and metallic particles adsorbed on wafer surfaces. As preparation chamber was evacuated down to $\sim 10^{-10}$ torr, samples were degassed at around 200 °C for about 12 hours. After degassing, samples were slowly heated to 900 °C and flashed to 1200 °C for 10 seconds to remove silicon oxides, followed by gradually cooling down to room temperature. Since high-temperature processing was involved in our preparation, a home-developed silicon wafer holder was used to prevent metal diffusion from clips etc., described in Chapter 2.

3.1.1.2 Results

HREELS was performed on a clean Si(111)(7×7) surface whose surface reconstruction was identified by the LEED pattern. Figure 3.3 shows the loss spectrum at room temperature which was obtained from an incident electron beam with the kinetic energy of $E_0=20.29$ eV (typical setting for most of measurements in this work). The spectrum-structure of EELS spectrum away from elastic peak ($E_{loss} = 0$ eV) is brought

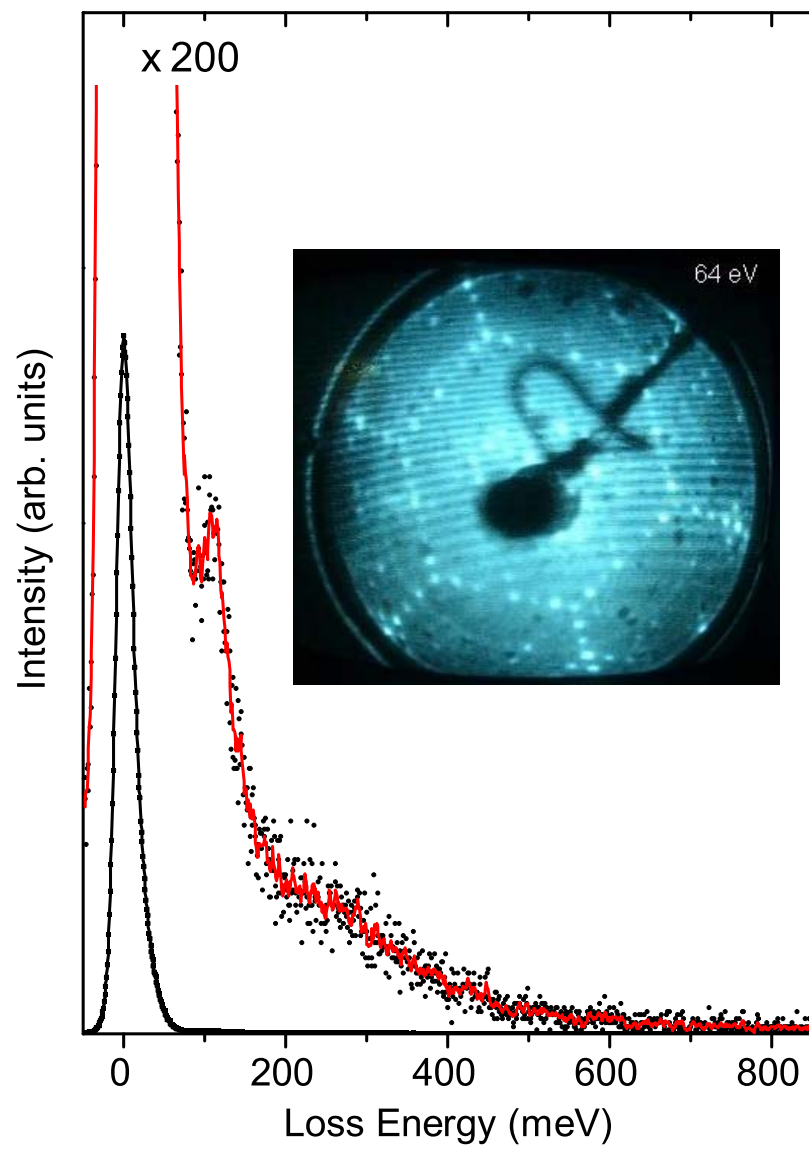


Fig. 3.3. Electron-energy-loss-data from a clean Si(111)(7 × 7) sample. The red curve is the average of 5 nearest neighbor data points . The inset shows the LEED pattern generated by an electron beam of 64 eV.

out by magnifying intensity of each scanning channel 200 times, and a red line within loss-intensity data points represents the average of five nearest neighbor points to smooth spectrum. The loss structure around 100 meV is convolution of carbon-adsorption [23] and surface band transition which was studied thoroughly by EELS [24, 25]. The 112-meV loss peak is the trace of carbon contamination on silicon surface. In our lab, the preparation chamber has a long history of deposition of C_{60} , so that in those loss spectra taken from samples with repeated heating processes, this carbon loss peak is very strong and needs to be removed in analyzing loss structures around 100 meV region. The inset of Fig. 3.3 shows the LEED pattern taken at the incident electron energy of 64 eV.

3.2 $\text{Si}(111)(\sqrt{3} \times \sqrt{3})\text{-Ag}$

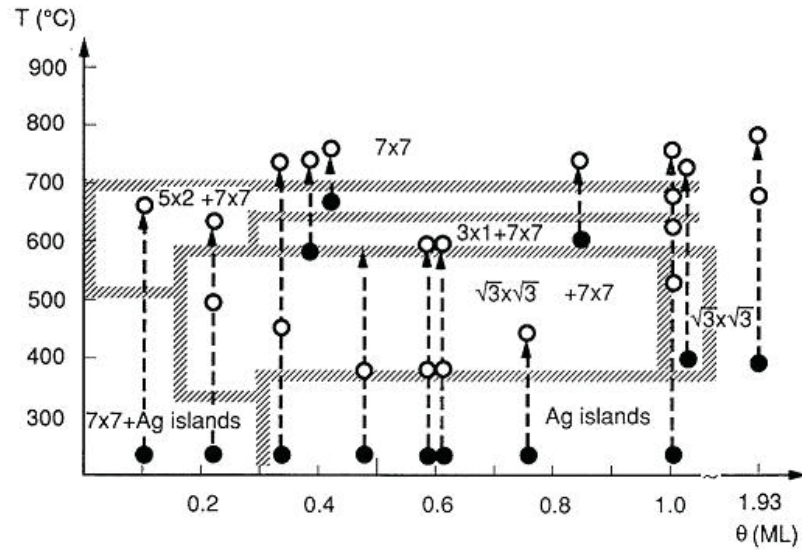


Fig. 3.4. Phase diagram obtained by STM-study of Ag/Si(111) system [26], showing surface reconstructions vs Ag coverage and annealing or growth temperature. The solid circles indicate initial growth conditions for a given sequence.

When silver atoms are deposited on Si(111)(7×7) surface, active dangling bonds are saturated by forming covalent bonds with silver adatoms, resulting in further surface rearrangements according to preparation conditions. Figures 3.4 shows the dependence of surface reconstruction on silver coverages, growing and annealing temperatures. The metallic Si(111)($\sqrt{3} \times \sqrt{3}$)-Ag surface provides a well-confined two-dimensional electron system to study 2DEG, which is much thinner than conventional two-dimensional gas systems formed at surface inversion layers or determinations. In the work on Si(111)($\sqrt{3} \times \sqrt{3}$)-Ag surface, we investigated plasmons dispersion of 2DEG and its evolution with further silver coverage.

3.2.1 Atomic and Electronic Structure of Si(111)($\sqrt{3} \times \sqrt{3}$)-Ag

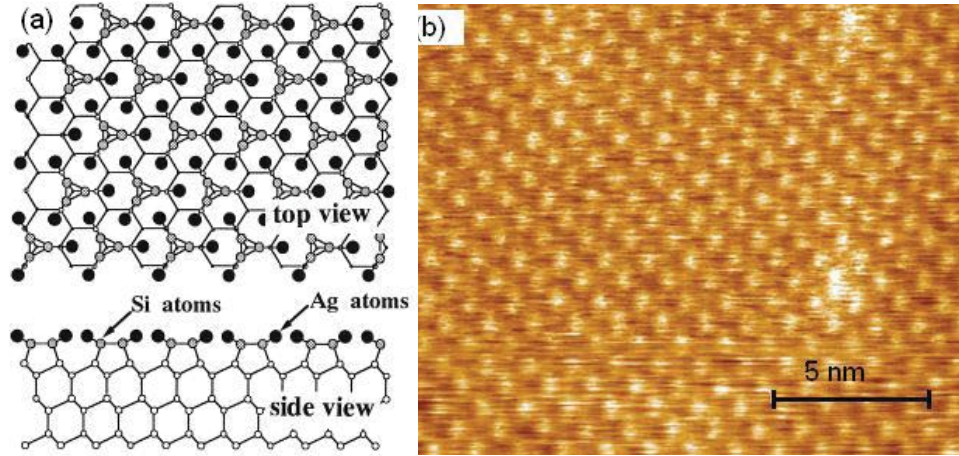


Fig. 3.5. Atomic structure of Si(111)($\sqrt{3} \times \sqrt{3}$)-Ag. (a) Schematic of atomic arrangements; (b) STM image, from Omicron Inc.

The Si(111)($\sqrt{3} \times \sqrt{3}$)-Ag surface also experienced a decades debate about its atomic arrangement, before two structure models were brought out to completely describe this reconstruction. The so-called "Honeycomb-Chained Triangle" (HCT) structure was firstly brought out in 1991 [27, 28], and then the so-called "InEquivalent Triangle" (IET) structure, was brought out after a symmetry-broken phase was discovered at low temperature [29], which was more energetically favorable than the HCT structure. However, at room temperature the thermal excitation makes the HCT structure favorable for the Si(111)($\sqrt{3} \times \sqrt{3}$)-Ag surface. The topmost silicon atoms (large open circles) make trimers, each of which forms an ionic covalent bond with a Ag atom (filled circles) to make Ag triangles, as shown in Fig. 3.5.

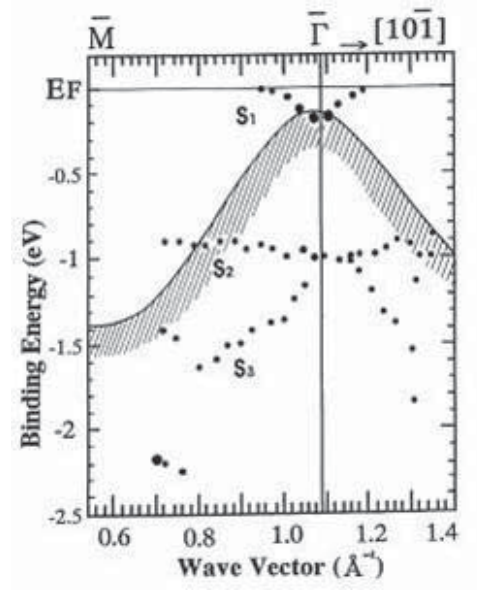


Fig. 3.6. Two-dimensional band-dispersion diagram for 1 ML Si(111)($\sqrt{3} \times \sqrt{3}$)-Ag surface measured by ARUPS [30]

Figure 3.6 shows band diagram of the surface states (denoted by S_1 , S_2 , and S_3) on the $\text{Si}(111)(\sqrt{3} \times \sqrt{3})\text{-Ag}$ surface [31, 21]. Of all these states, the S_1 state has a striking parabolic dispersion feature, i.e. the parabolic dispersion strongly crossing E_F in contrast to the localized S_1 state on the $\text{Si}(111)(7 \times 7)$ surface (Fig. 3.2). The bottom of this parabolic band is located below E_F by about 0.2 eV, so that electrons are trapped in this surface state, and the broad dispersion also means an extended wavefunction for this state, resulting in electrons traveling via the centers of the Ag triangles which have maximums in its local density of states [corresponds to the protrusions in the empty state STM image (Fig. 3.5)]. This surface state S_1 is irrespective of the doping type and doping concentration of silicon wafers and either of the surface preparation procedure, which is confirmed by both (ARUPS) [30] and HREELS [8]. This suggests intrinsic two-dimensional nature of a free electron system in surface state S_1 as the exclusive result of reconstruction of topmost two to three layers ($\sim 5 \text{ \AA}$).

3.2.2 Sample Preparation

The ultra-purity silver pellets were melted and evaporated from a home-made tantalum effusion cell with an aperture directed at the sample surface. The deposition rate was monitored by quartz crystal oscillator which can be moved directly in front of sample. The thickness of silver, expressed here in the unit of ML (monolayer, corresponding to $7.8 \times 10^{14} \text{ atoms cm}^{-2}$, areal density of silicon atom on $\text{Si}(111)$ surface), was controlled by tuning the time of exposure to the source. To obtain silver-induced reconstruction, besides a initially 7×7 -reconstructed silicon substrate, certain elevated

temperature of substrate was required at deposition. Typically in our work, Si(111)- $(\sqrt{3} \times \sqrt{3})$ -Ag was prepared by depositing 1 ML silver onto a Si(111)(7×7) substrate at 500 °C, as plotted in the temperature- and coverage-dependent phase diagram, Fig. 3.4.

The prepared Si(111)- $(\sqrt{3} \times \sqrt{3})$ -Ag surface was checked by LEED before performing HREELS measurements. Although less intuitive to direct observation by LEED pattern, HREELS spectrum can somehow reflect the difference of various metallized surface reconstructions. Figure 3.7 shows the spectra taken from the same sample with different surface superstructures. The black, red, green curve show the normalized spectra of 7×7 , 3×1 , $\sqrt{3} \times \sqrt{3}$ surface, respectively. The spectra in the dashed box are magnified 100 times to show rich features in that region, where an obvious broadening of positive parts of elastic peaks induced by the superposition of Drude background indicates the increasing metallic properties of surfaces. Meanwhile, the suppression and broadening of peaks and background are strong evidences that these rich loss features only originate from certain surface superstructures.

3.2.3 Plasmon Dispersion of Si(111)- $(\sqrt{3} \times \sqrt{3})$ -Ag

To characterize sheet-plasmon dispersion, a series of angular-dependent measurements were performed by EELS. The momentum transfer, q , of each measurement is determined by applying conservation laws of energy and momentum:

$$E_{\text{loss}} = E - E', \quad (3.1)$$

$$q = k_{\text{i}} \sin \theta_{\text{i}} - k_{\text{off-spec}} \sin(\theta_{\text{i}} - \phi_{\text{s}}), \quad (3.2)$$

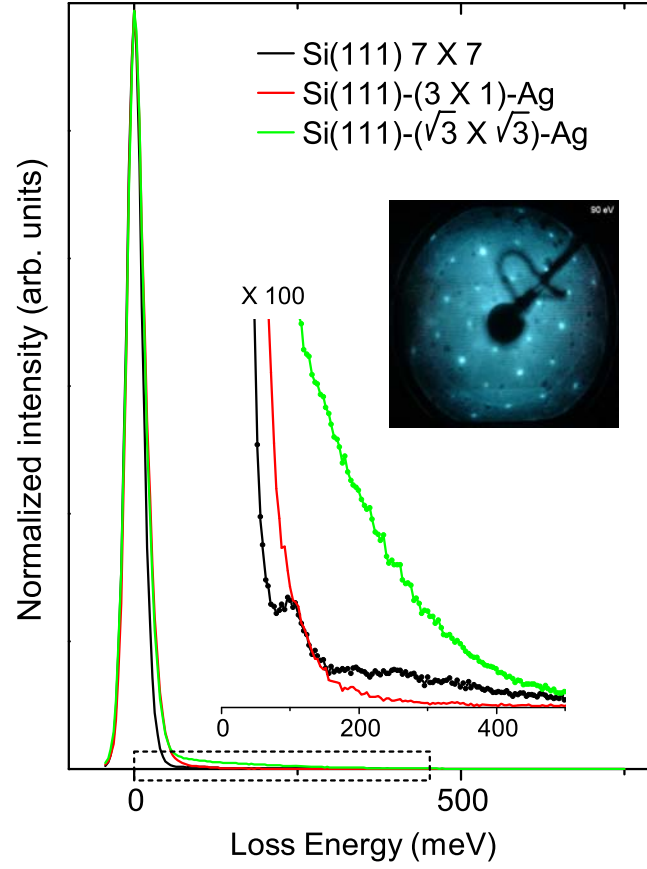


Fig. 3.7. HREEL-spectra taken from the same sample on Si(111)-(7×7), (3×1)-Ag, and ($\sqrt{3} \times \sqrt{3}$) surface at room temperature. Electron impact energy $E_0=20.29\text{eV}$ and incident angle $\theta=60^\circ$. Inset: LEED pattern of Si(111)-($\sqrt{3} \times \sqrt{3}$)-Ag surface, taken at 90 eV of the incident electron beam.

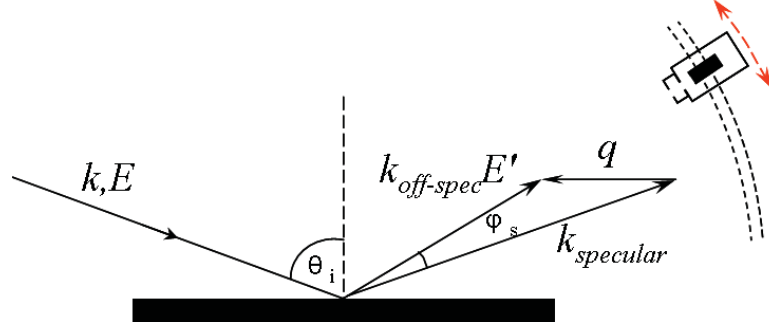


Fig. 3.8. Scattering geometry of HREELS used in this work. The analyzer can slide on the track to achieve off-specular scattering at various scattering angle ϕ_s .

where definitions of variables are illustrated in Fig. 3.8. Given a slow electron with static mass, m_e , we have

$$q = \frac{\sqrt{2m_e E}}{\hbar} [\sin\theta_i - \sqrt{1 - E_{\text{loss}}/E} \sin(\theta_i - \phi_s)]. \quad (3.3)$$

The electron density on Si(111)($\sqrt{3} \times \sqrt{3}$)-Ag surface is in the order of 10^{13} cm^{-2} , which results in the plasmon energy in the region from 100 meV to 700 meV. For measurements at small scattering angle, loss structures of spectra mainly reside in the region where strong "Drude" tails and adsorbate-vibration coexist. The superposition of peaks from various physical processes makes a pure mathematical deconvolution not reliable. For instance, the parameter for Drude background must input on case-by-case basis, since it highly depends on surface on study, but the source of fitting parameters is from raw spectra with all other structures included. Especially in cases with high electron density of surface, dispersion behaviors at small q have no general trend. To achieve consistence in data analysis, we exclude any manual input in data analysis by sacrificing the spectrum

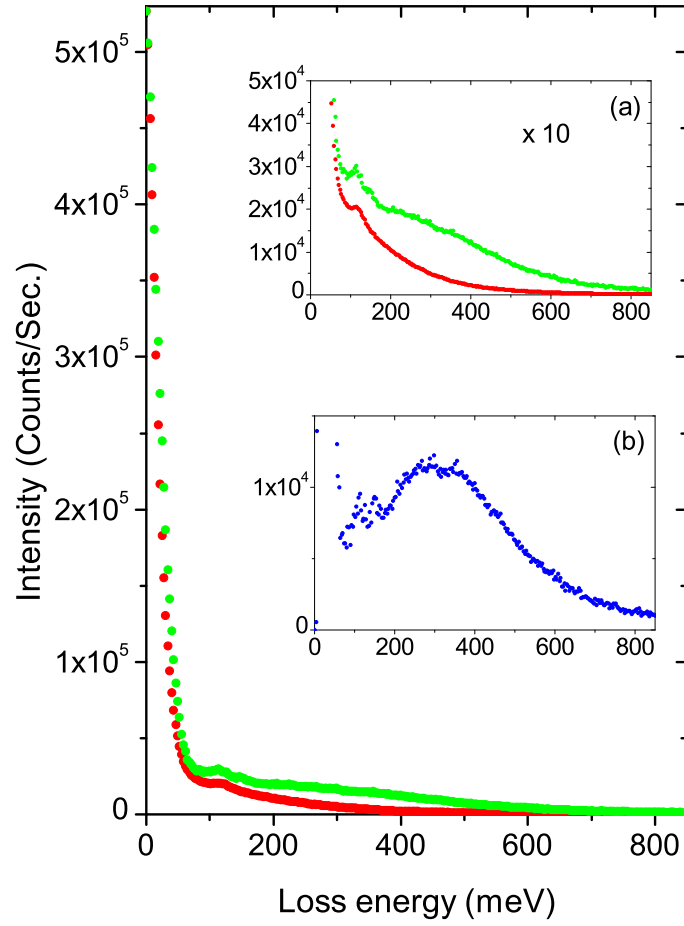


Fig. 3.9. Spectra of Si(111)($\sqrt{3} \times \sqrt{3}$)-Ag at specular scattering ($\phi_s=0^\circ$) and off-specular ($\phi_s=2^\circ$). Inset: (a) 10-times magnified spectra; (b) background-removed spectra by using off-specular spectra subtracting specular one.

in specular direction as a background calibration for individual measurements at off-specular directions due to the fact that the spectrum in specular direction contains actual information for both "Drude" tail and adsorbates vibrations. Figure 3.9 shows the process to bring out the plasmon loss peaks. A complete background-removed spectra of Si(111)-($\sqrt{3} \times \sqrt{3}$)-Ag is illustrated in Fig. 3.10.

Fig. 3.11 shows plasmon dispersion with wavenumber and loss intensity profile with wavenumber and scattering angle. The vanishing of plasmon energy in long wavelength limit is the signature of sheet plasmon in contrast to the opening of a gap at zero q wavevector in the case of surface and bulk plasmons. The range of dispersing energy is far larger than any dispersion of phonons on semiconductor surfaces. Moreover, parameters from the data-fitting based on 2DEG theoretical calculation agree well with those obtained by other experimental techniques.

The fitting model we used was derived by Stern within the framework of the nonlocal response theory by random phase approximation (RPA) [32]. The following is an approximation up to the second-order term in q :

$$\omega(q) = \left[\frac{4\pi n_{2D} e^2}{m^* (1 + \varepsilon)} q + \frac{3\pi n_{2D} \hbar^2}{2 (m^*)^2} q^2 + o(q^3) \dots \right]^{1/2}. \quad (3.4)$$

where $\omega(q)$ is the plasmon frequency, n_{2D} is the areal density of electrons, m^* is the effective mass of electrons, e is electron charge, and ε is the substrate dielectric constant which is non-dispersing within the frequency range of interest. Fitting was performed by setting n_{2D} and m^* as fitting variables. In the long wavelength limit, the higher order terms of q vanish quickly in the Eqn. 3.4, consequently the plasmon dispersion follows

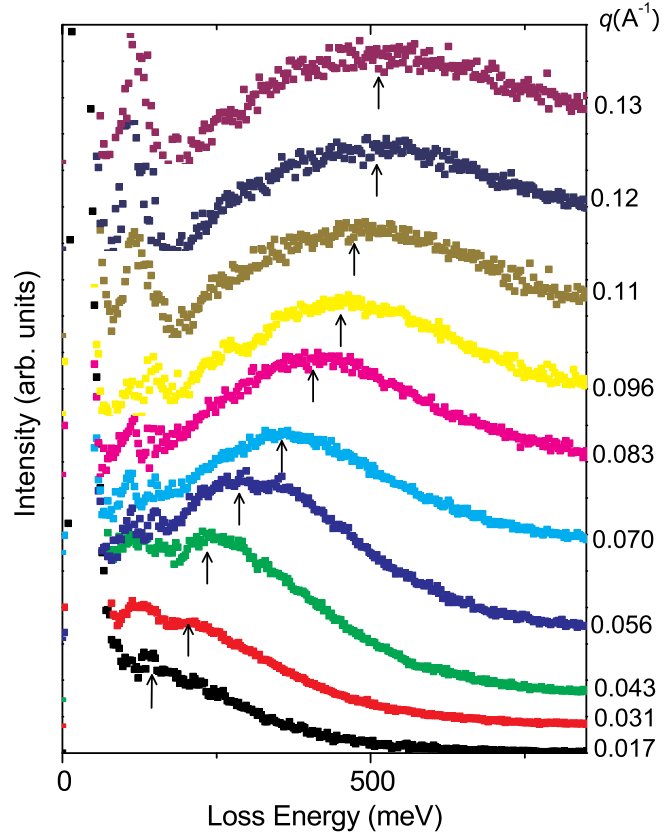


Fig. 3.10. Background-removed spectra taken from Si(111)-($\sqrt{3} \times \sqrt{3}$)-Ag surface at room temperature. The black arrows indicate the center of loss peaks, with q at the right side corresponding to momentum transfers of measurements at various angles. Electrons impact energy: $E_0=20.29\text{eV}$, and incident angle: $\theta=60^\circ$.

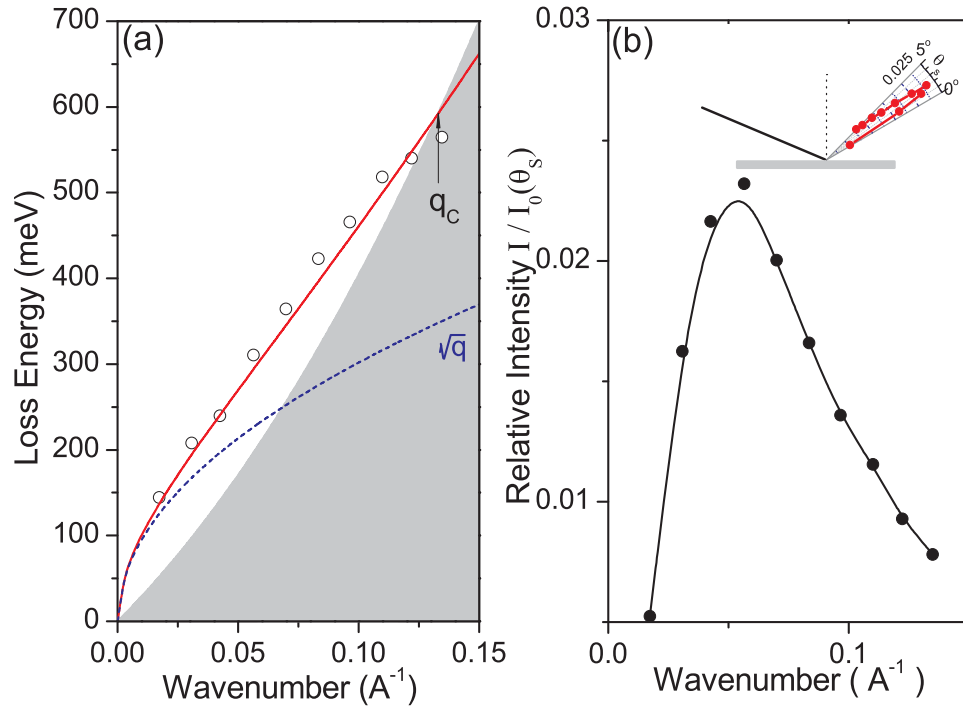


Fig. 3.11. (a) Plasmon energy dispersion on Si(111)-($\sqrt{3} \times \sqrt{3}$)-Ag surface. The red curve is the best fit of plasmon energy according to Stern's theory on 2DES with non-local correction. The dashed blue curve indicates the \sqrt{q} dispersion for non-interacting 2DEG with the same electron density as prepared $\sqrt{3}$ surface. (b) Loss-intensity profile plotted in both cartesian and polar coordinates. The scale of angular coordinate was magnified 3 times for visibility.

the \sqrt{q} behavior which is the case of non-interacting 2DEG. A transformation of the second term in Eqn. 3.4 can be made by introducing Fermi velocity

$$v_F = \frac{\hbar k_F^2}{m^*}, \quad (3.5)$$

where

$$k_F = \sqrt{2\pi n_{2D}}. \quad (3.6)$$

Then the second term can be rewritten as $\frac{3}{4} v_F^2 q^2$ which indicates the origin of this correction from non-local effects.

The red curve in Fig. 3.11 shows the best fitting to data points, which gives $n_{2D} = 2.0 \pm 0.56 \times 10^{13} \text{ cm}^{-2}$ and $m^* = (0.18 \pm 0.03)m_e$, respectively. The blue dashed curve is non-interacting 2DEG \sqrt{q} dispersion calculated with the electron density from this fitting. The correction term dominates the behavior at large wavenumber and deviates the dispersion of sheet plasmons from that of non-interacting 2DEG as increasing wavenumber q . A cutoff wavenumber q_c (black arrow in Fig. 3.11) shows where the collective excitation of electrons enters a single-particle-excitation region and decays into electron-hole pairs, which is also the so-called Landau edge. The loss intensity of plasmons quickly damp after entering into shaded region, indistinguishable from background.

3.2.4 Evolvment of Plasmons Dispersion Behavior

The surface plasmon of silver, both on silver single-crystal surface and silver thin-film on Si(111)-(7 × 7), is a well-studied 3D-type plasmons [3, 2, 33, 34]. Sheet plasmons distinguish themselves primarily from surface plasmons by having a vanishing energy in

the long wavelength limit rather than a finite value. In this part of my work, in order to investigate how sheet-plasmon dispersion response to further silver adatoms, HREELS measurements were performed on Si(111)-($\sqrt{3} \times \sqrt{3}$)-Ag surface with various thicknesses of Ag-film overlayer.

All measurements are performed consecutively on the same sample prepared in-situ. For each deposition, HREELS measurements started from scattering angle $\phi_s=0^\circ$ (specular direction) to $\phi_s=5^\circ$ with the step of 1° , rather than previously more detailed measurements with the step of 0.5° . The amounts of silver was calculated by multiplying deposition rate with exposure time to source. The sample was kept at room temperature at deposition and without further annealing.

Figure 3.12 shows how plasmon dispersion behaviors evolve with deposition of silver adatoms on Si(111)-($\sqrt{3} \times \sqrt{3}$)-Ag surface. In Fig. 3.12(a), using the same Stern model in previous section to fit plasmon data, we have electron density of $n_{2D}=2.04, 3.09, 1.77 \times 10^{13} \text{ cm}^{-2}$ for 1-ML, 1.02-ML, and 1.05-ML surface, respectively.

The blue shift and increased steepness in the dispersion of 1.02-ML surface are due to the charge transfer from silver adatoms to surface state S_1 (Fig. 3.13). This observation is consistent with a photoemission study on Si(111)-($\sqrt{3} \times \sqrt{3}$)-Ag surface. [35] By depositing silver adatoms, the surface state shifts downward and as a result, the two-dimensional Fermi surface also enlarges, as shown in Fig. 3.13(a), which is indicated by the increase of electron density from our fitting of n_{2D} . The other feature from evolving dispersions is that a critical coverage $\Theta_c \sim 0.02 \text{ ML}$ of silver adatoms exists on Si(111)-($\sqrt{3} \times \sqrt{3}$)-Ag surface. This similar critical coverage was also reported in measurements of electrical conduction [37] and ultraviolet photoelectron spectroscopy,

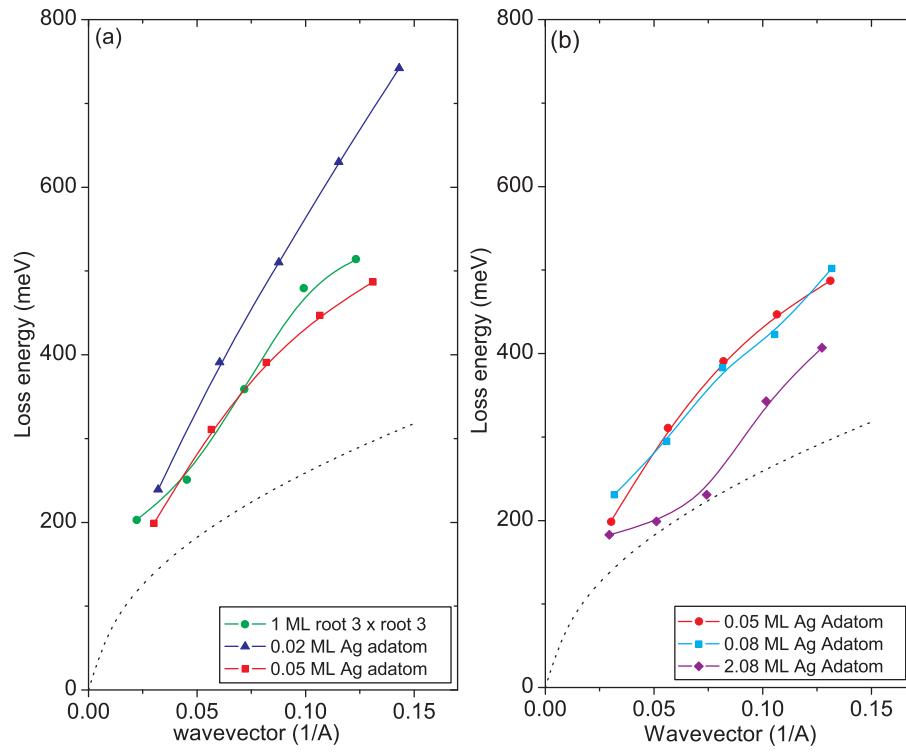


Fig. 3.12. Sheet plasmon dispersions up to 1.08 ML of silver adatoms. (a) Dispersion of silver film thicknesses from 1 ML to 1.05 ML (b) Dispersion silver film thicknesses from 1.05 ML to 2.08 ML.

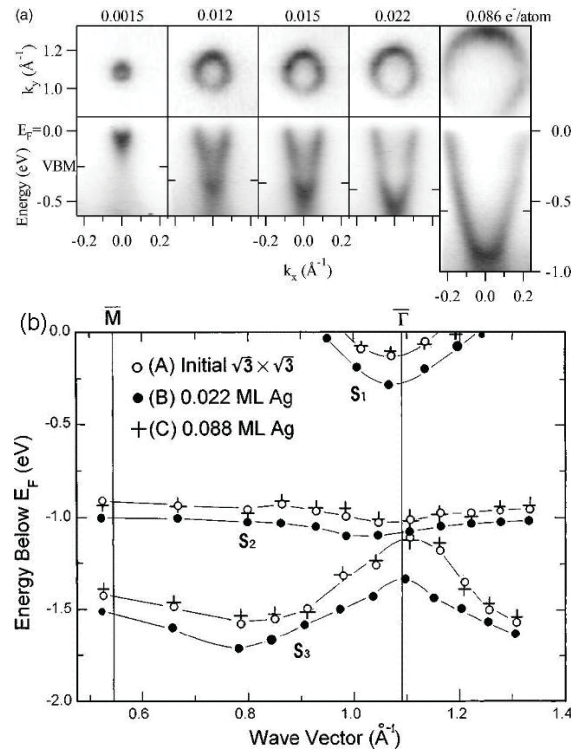


Fig. 3.13. (a) Photoemission measurements of Ag-doped surface state of Si(111)($\sqrt{3} \times \sqrt{3}$)-Ag. From Ref. [35]. (b) Angle-resolved ultraviolet photoelectron spectroscopy on Ag-doped Si(111)($\sqrt{3} \times \sqrt{3}$)-Ag. From Ref. [36].

Fig. 3.13(b) [36]. Below Θ_c , a so-called two-dimensional adatom gas phase is formed, and remarkably increases electron density of surface, contributing to higher plasmon energy and surface conductance. A frozen two-dimensional adatom gas was imaged by low-temperature STM study [38]. Continued deposition exceeding Θ_c , the two-dimensional adatom gas phase is destroyed by formations of silver micro-crystals where nucleation centers work like a sinker to trap all the highly mobile silver adatoms. A quantitative analysis of this critical coverage Θ_c can be done in the frame of thermodynamics of crystal growth, with related information of surface, e.g. surface diffusion energy and constant, binding energy of clusters, and surface characteristic vibration frequency.

Figure 3.12(b) shows plasmon dispersion behaviors measured up to 2.08-ML silver adatoms. There is not much difference between 1.05 ML [red curve, Fig. 3.12(b)] and 1.08 ML [cyan curve, Fig. 3.12(b)], however, a striking change was observed when the film thickness reached 2.08 ML [purple curve, Fig. 3.12(b)]. The linear-like dispersion changed to a more complicated curvature and Stern's model failed to fit this dispersion. For instance, the best fitting of 2.08 ML sample gave $n_{2D} = 3.60 \pm 3.48 \times 10^{13} \text{cm}^{-2}$, in which the uncertainty was almost the same as electron density itself. Furthermore, a smooth extrapolation into the long wavelength limit suggests a finite gap. In order to characterize this behavior, a series of more detailed measurements starting with 0.37 ML to 4.05 ML of silver adatoms were performed on the same sample in Fig. 3.14(a),(b).

The tendency to the opening of a gap at long wavelengths becomes more distinct with the increasing thickness of silver adatoms. This energy gap is estimated to be 225

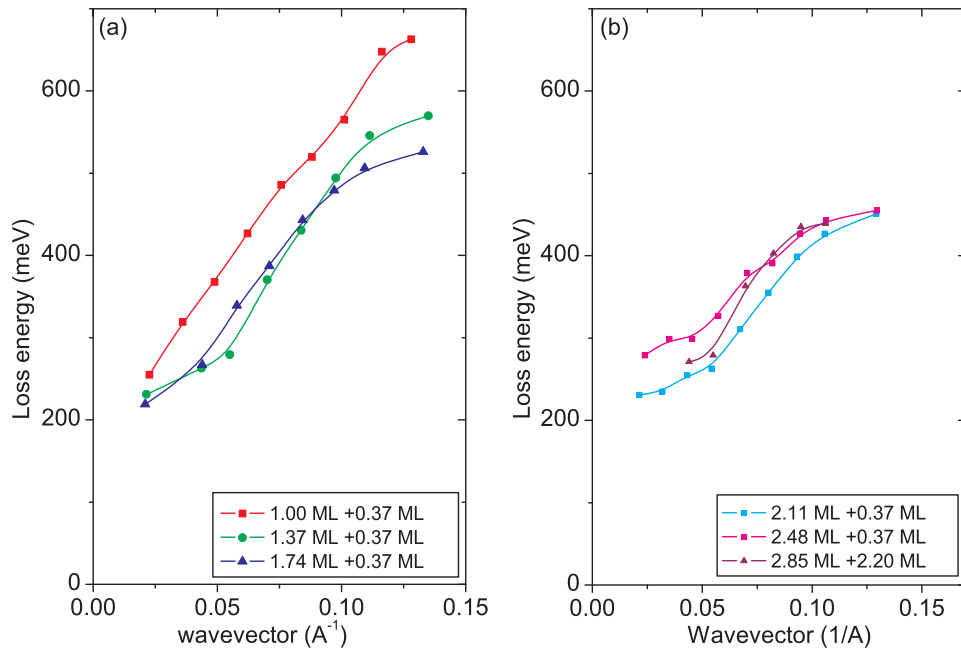


Fig. 3.14. Plasmon dispersions up to 4.05-ML silver adatoms. HREELS measurements were performed at various scattering angle ϕ_s with a angular step of 0.5° . (a) Dispersion of 0.37-ML, 0.74-ML and 1.11-ML silver adatoms (b) Dispersion of 1.48 ML, 1.85-ML, 4.05 ML silver adatoms.

± 15 meV², which is out of any energy range of most types of quasiparticles on silicon and silver surfaces, to the best of my knowledge. Due to the specular beam intensity in HREELS, we cannot experimentally investigate this behavior in the long wavelength limit, despite the significant physical importance in disclosing possible new mode or coupling of collective excitations. However, it is a worthy test to discuss this observation in the context of simple models of the charge profiles at the surface within the framework of surface plasmon theory.

Starting with the simple metal, alkali metals have spherical Fermi surfaces lying entirely inside a first Brillouin zone, where s electrons have negligible influence from filled d -band structure. The unscreened bulk plasma frequency ω_p of a free electron gas is:

$$\omega_p = \sqrt{\frac{n_{3D} e^2}{m_e \varepsilon_0}}. \quad (3.7)$$

where n_{3D} is bulk density of electrons, m_e is static mass of electrons, e is electron charge, and ε_0 is static dielectric constant of vacuum. The electron density of alkali metals can be estimated by

$$n_{3D} = \frac{\rho N_A}{M}, \quad (3.8)$$

where ρ is the density of bulk, N_A is the Avogadro constant, and M is the mole of mass. For instance, sodium has $\rho = 0.97$ g cm⁻³ and $M = 22.99$ g mol⁻¹, then $n_{3D} = 2.54 \times 10^{22}$ cm⁻³. It turns out the bulk plasmon energy of sodium is 5.92 eV by applying Eqn. 3.7, which is close to experimental measurements, 5.6 \sim 5.72 eV [1]. The surface plasmon

² The estimation was done by averaging energy-intercepts of linear fitting to dispersion curves of three different thicknesses, in the small q region ($q < 0.05 \text{ \AA}^{-1}$).

frequencies, ω_{sp} , of most alkali and alkaline-earth metals are equal to $\omega_{\text{p}}/\sqrt{2}$ [3]. However, the noble metals fail to follow $1/\sqrt{2}$ ratio between surface plasmon and bulk plasmon due to the involvement of filled d -band states. Treated the same way as free electron gas of alkali metals, the bulk plasmon frequency of silver gives $\hbar\omega_{\text{p}} = 8.98$ eV, which is way above the experimental result, 3.78 eV [1]. The screened bulk plasma frequency ω_{p}^* was calculated by introducing dynamical response from d -band into the dielectric function $\varepsilon(\omega)$, leading to

$$\varepsilon(\omega) = \varepsilon(\omega)_f + \varepsilon(\omega)_d, \quad (3.9)$$

where $\varepsilon(\omega)_d$ is dielectric function of d -band electrons and

$$\varepsilon(\omega)_f = 1 - \frac{\omega_{\text{p}}^2}{\omega^2} \quad (3.10)$$

for free s electrons. Therefore, we have

$$\omega_{\text{p}}^* = \frac{\omega_{\text{p}}}{\sqrt{1 + \varepsilon(\omega)_d}}, \quad (3.11)$$

accordingly, the screened surface plasmon is

$$\omega_{\text{sp}}^* = \frac{\omega_{\text{p}}}{\sqrt{2 + \varepsilon(\omega)_d}}. \quad (3.12)$$

$\varepsilon(\omega)_d$ was obtained from both optical experiment [39] and calculation [40], with a value of about 5 to 6, which gave $\hbar\omega_{\text{sp}}^*$ is around 3.67 eV.

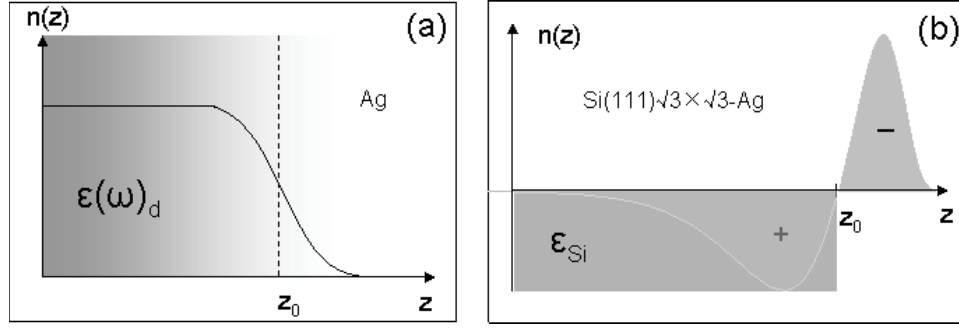


Fig. 3.15. Schematic of charge profile in normal direction of surface. (a) Silver single-crystal surface. z_0 indicates the interface of silver and vacuum. The solid curve shows the density variation of free $5s$ electron. The shaded area represents screening effect from $4d$ electrons in terms of $\epsilon(\omega)_d$. (b) $\text{Si}(111)(\sqrt{3} \times \sqrt{3})\text{-Ag}$ surface. z_0 here indicates the interface of silver film and silicon substrate. The light shaded areas show charge profiles of electrons (-) and holes (+), which have the same area to keep surface region electronic neutrality.

Figure 3.15 shows charge profiles of silver surface and $\text{Si}(111)(\sqrt{3} \times \sqrt{3})\text{-Ag}$ surface. At the silver/silicon interface z_0 in Fig. 3.15(b), the dark shaded region indicates the surface space-charge layer where electrons are depleted. This depletion layer beneath interface ($z < z_0$) deeply extends into silicon bulk, and accumulated holes is represented by light shaded region with the same area as the electrons region. The existence of this depletion layer determines the electron density of surface by accepting electrons of deposited silver adatom once the two-dimensional adatom gas phase is destroyed. In our calculation, $n_{3D} = 8.61 \times 10^{19} \text{ cm}^{-3}$ is obtained and converted from fitting of surface with 0.08-ML silver adatoms (blue curve in Fig. 3.12(b)), m_e in Eqn. 3.7 is replaced with effective mass of $m^* = 0.19 m_e$ to introduce the effect from band structures, and $\epsilon(\omega)_d$ in Eqn. 3.12 is replaced with a dispersionless silicon dielectric constant $\epsilon_{\text{Si}} = 11.5$, then we have

$$\omega_{\text{sp}}^* = \sqrt{\frac{n_{3D} e^2}{m^* (2 + \epsilon_{\text{Si}})}}. \quad (3.13)$$

and screened surface plasmon energy $\hbar\omega_{\text{sp}}^* = 215$ meV, which agrees well with estimation, 225 ± 15 meV. This agreement in energy of surface plasmon at the vanishing momentum transfer indicates that the transition from 2D electron density to 3D electron density in calculation virtually reflects the transition from sheet plasmon to surface plasmon. The observation of this transition is due to the unique structure of 2DEG systems, where nearly free electrons with high density are trapped in silver-induced superstructure and strongly affected by underneath silicon depletion layer. Although the other two systems show 2D plasmon dispersions, i.e. image-potential-induced surface states on liquid helium [5] and silicon inversion layer [6], they are not able to vary the film thickness.

As a speculation, at certain stage (20 ML in our observation) that silver atoms are sufficient enough to fully cover surface, the low-energy surface plasmon disappear and conventional surface plasmon appears. Figure 3.16 shows the continuous deposition until the appearance of the conventional silver surface plasmon (~ 3.9 eV), which generally agrees with studies of surface plasmons on Ag/Si(111)(7×7) surface of various thicknesses of silver thin film. [33, 34]. We were not able to measure the dispersion of the conventional surface plasmon since its loss intensity was not strong enough to distinguish peak locations in off-specular measurements.

Another feature is that the dispersing slope changes abruptly around $q \approx 0.05 \text{ \AA}^{-1}$ in Fig. 3.14 as a result of plasmon confinement within silver crystal island. Plasmons with wavelength larger than the size of island d can not propagate, so the size of island can be calculated by equating $d = 2\pi/q$. In the our case, the island size is $d = 126 \text{ \AA}$ which is comparable to results of STM study of Ag/Si(111) [41].

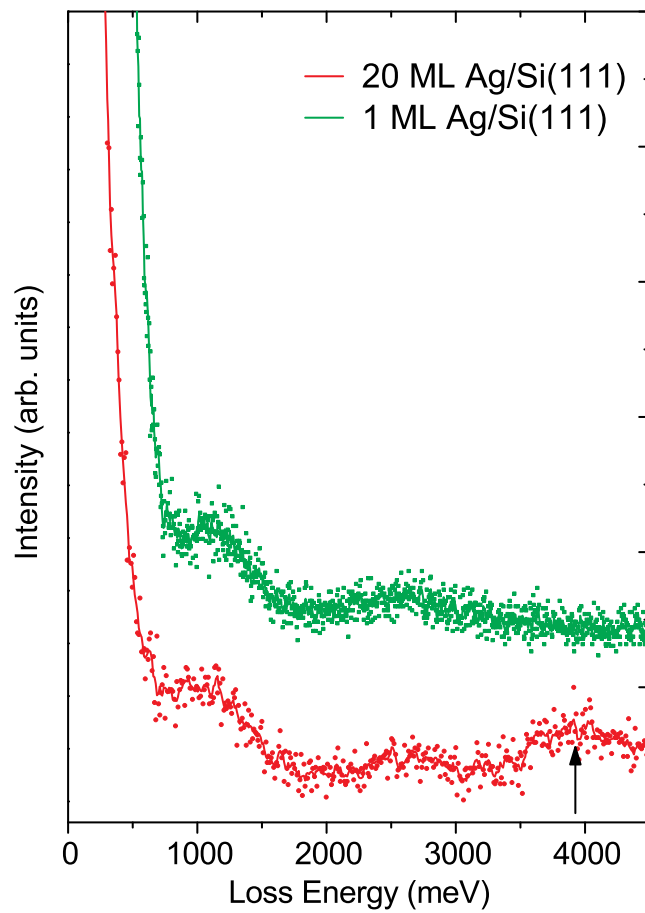


Fig. 3.16. Conventional surface plasmon appeared at the deposition of 20-ML silver adatoms. Black arrow (3.9 eV) indicates the conventional surface plasmon.

3.3 Conclusion

In summary, a systematic study on surface of silver/silicon was done by HREELS, the thickness-dependent dispersion behaviors of $\text{Si}(111)(\sqrt{3} \times \sqrt{3})\text{-Ag}$ were characterized. The evolution of sheet plasmons in the low coverage of silver adatoms revealed a critical coverage corresponding to the formation and destruction of two-dimensional adatom gas phase, which agrees with conductance and ultraviolet photoelectron measurements. Both observation and calculation of opening gap in the long wavelength limit implicated a transition from 2D-type sheet plasmons to 3D-type surface plasmons, as the result of unique electronic structure of 2DEG system on $\text{Si}(111)(\sqrt{3} \times \sqrt{3})\text{-Ag}$. Finally, the grainy size of silver island can be estimated from the kink of dispersion curves, where plasmon starts dispersion. A more sophisticated calculation is necessary to fully understand the dispersion behaviors of the low-energy surface plasmon, where Stern's model fails, and particularly, its dependence on the changing micro-morphology.

Chapter 4

Plasmon Dispersion of Epitaxial Graphene Layer

4.1 From Graphite to Graphene

4.1.1 Graphite

Graphite is one of the allotropes of carbon which has been studied for more than half century and is widely used as a well-defined substrate in current surface science research, and a calibration surface in a variety of microscopies of atomic resolution, e.g. scanning tunneling microscopy, atomic-force microscopy, etc. As a layered material, graphite is composed of a stacked hexagonal planes, in which carbon atoms in a plane have a nearest neighbor spacing of 1.42 Å and the adjacent layers are separated by 3.35 Å. The graphite crystal lattice and the stacking sequence of graphite layers are shown in Fig. 4.1(a), whereas the Brillouin zone is a thin hexagonal cylinder in Fig. 4.1(b).

The electronic band structure is well developed in theoretical calculation and verified in various experimentations, e.g. optical excitation [42], magnetoreflexion [43, 44], excitation by electrons [45, 46, 47]. In a single plane, the carbon atoms are strongly bound to their nearest neighbors by sp^2 covalent bonds, while the graphite sheets are weakly bound together by the remaining p_z electrons. These two bondings are reflected in the electronic band structure by σ band and π bands. The sp^2 hybrid bonds form σ bands which have widely separated filled bonding σ and unfilled anti-bonding σ^* states. The p_z bonds form overlapping π and π^* bands which are located about the Fermi level

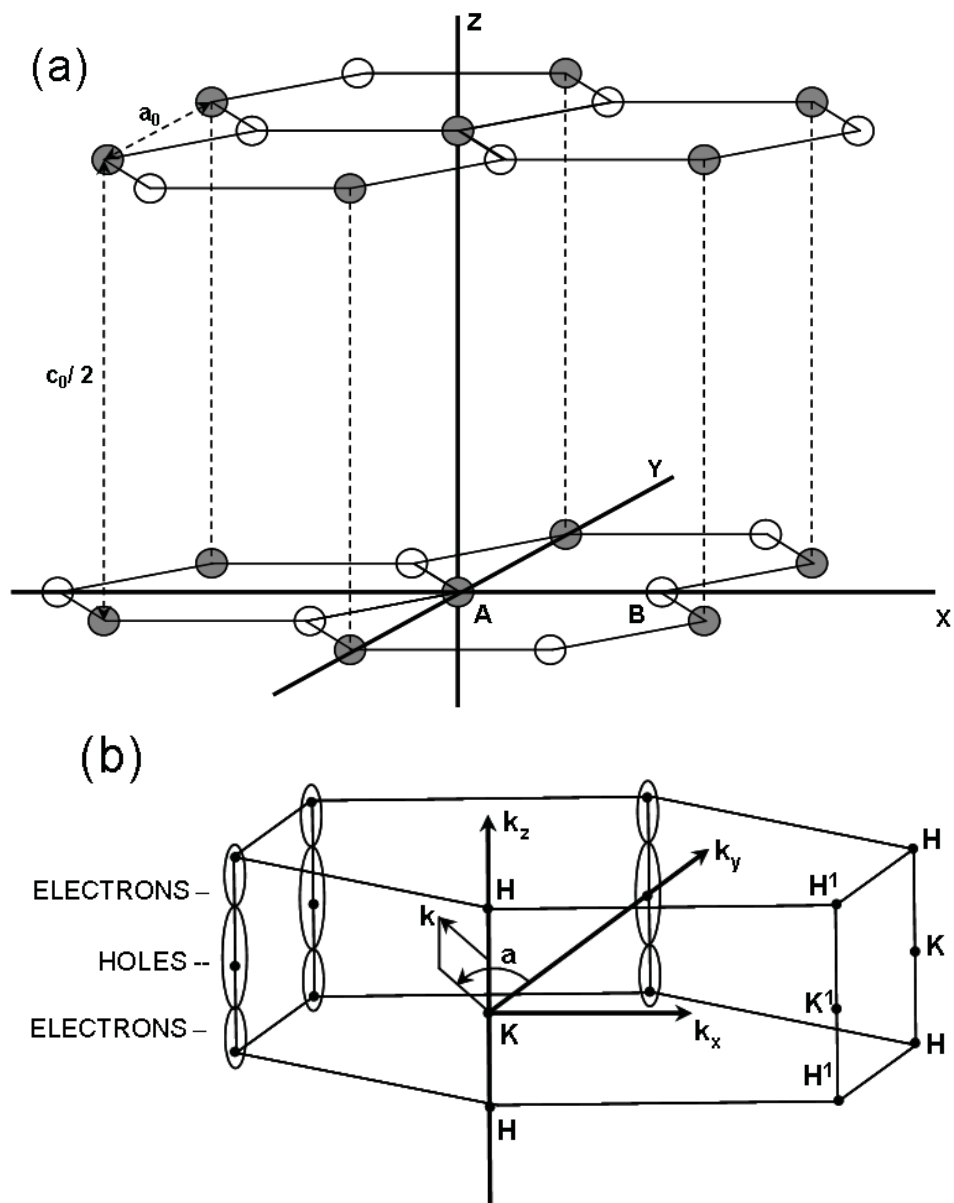


Fig. 4.1. (a) Graphite lattice. (b) Brillouin zone of graphite.

and well within the gap between the bonding and anti-bonding σ bands. The dispersion characteristics of these π and π^* bands are shown in Fig. 4.2. Thus the excitation energies less than σ bands gap (6 eV) are dominated by states within the π bands.

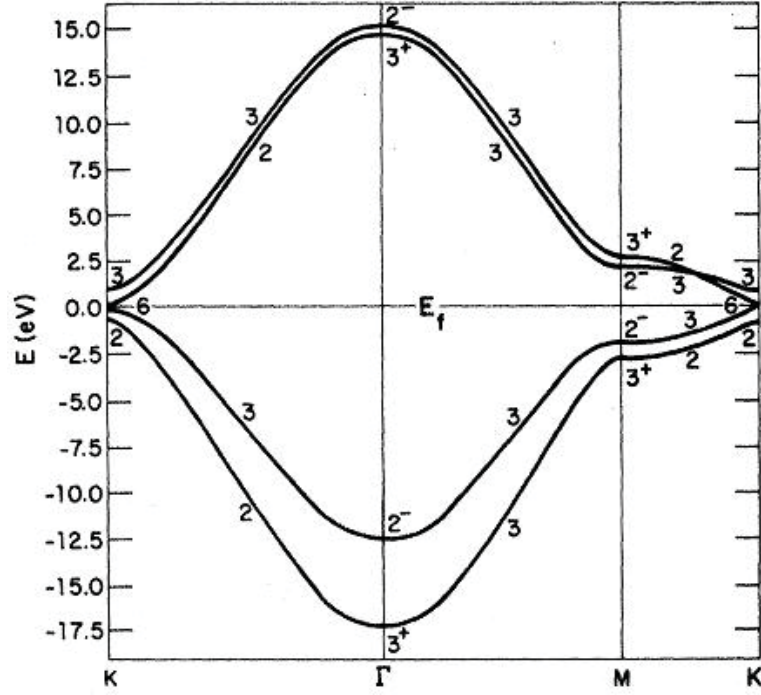


Fig. 4.2. The π energy band of graphite along several high symmetry direction. The energy dispersion is plotted relative to Fermi level in the low-energy electronic excitations of graphite [48].

4.1.2 Graphene

Graphene is a single layer of carbon atoms tightly packed into a two-dimensional (2D) honeycomb lattice, which is also a basic building block for graphitic materials of all other dimensionalities. It can be wrapped up into zero-dimensional (0D) fullerenes,

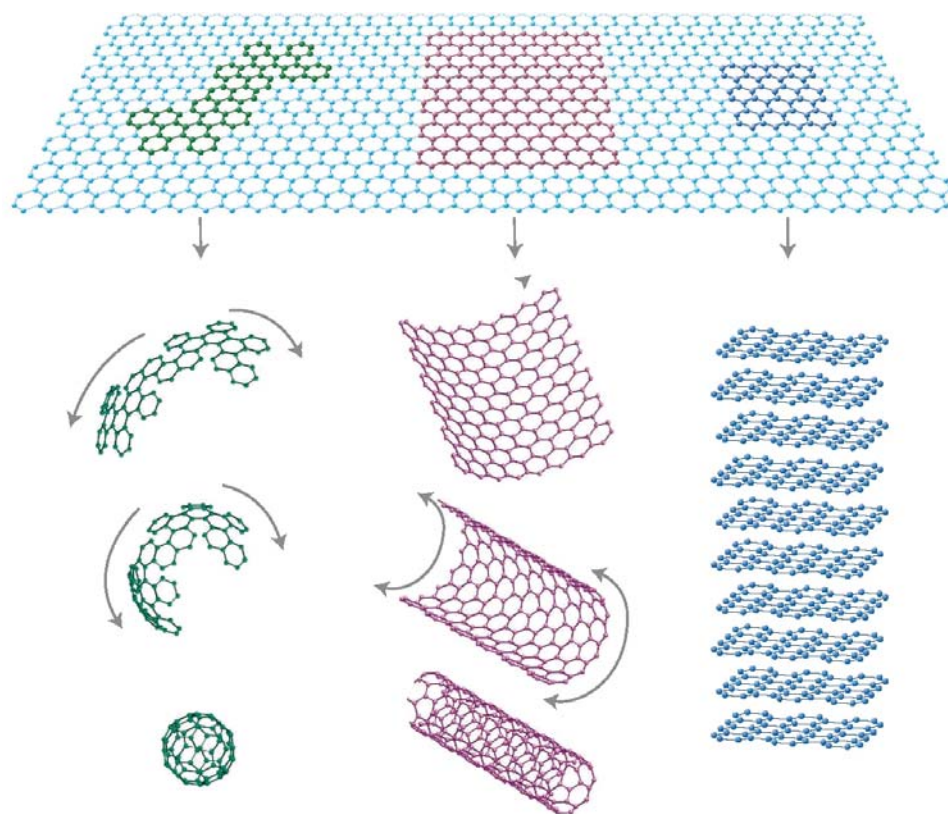


Fig. 4.3. building block of graphitic materials. It can be wrapped up into buckyballs (0D), rolled into nanotubes (2D) or stacked into 3D graphite. Figure duplicated from reference[49]

rolled into one-dimensional (1D) nanotubes or stacked into three-dimensional (3D) graphite shown in Fig. 4.3.

Four decades ago, graphene was the model used for calculating the band structure of graphite [50, 51]. Forty years later, an experiment study revealed the charge carriers in graphene mimic relativistic particles with zero rest mass and have an effective 'speed of light' $c^* \approx 10^6$ m/s [52, 53]. This unusual phenomena currently attracts enormous attention in academic research, including an anomalous quantum Hall effect [53, 54], ballistic electron transport at room temperature [55], micron-scale coherence length [55, 56], and novel many-body couplings [57].

There are primarily two methods to obtain graphene: micromechanical cleavage of bulk graphite [52] and epitaxial growth on SiC [58]. From the first method, one can find a free-standing graphene layer by deliberately searching with a carefully prepared Si wafer substrate covered a certain thickness of SiO₂. However, tremendous caution and perseverance of researchers are indispensable for accomplishing graphene searching among thousands of graphite flakes. Comparing with the first method, the second method enables graphene to be prepared in large scale by using commercialized SiC wafer, which make it a possible route towards graphene electronics. The epitaxial growth requires sample thermal processing up to 1500 °C in ultrahigh vacuum and LEED for structure characterization.

In this work, the sheet-plasmon dispersion of epitaxial graphene single layer are studied for the first time and compared with sheet plasmons of 2D surface state of Si(111)-($\sqrt{3} \times \sqrt{3}$)-Ag surface, presented in previous chapter.

4.2 Single Layer Graphene¹

Using angle-resolved high-resolution electron-energy-loss-spectroscopy (HREELS), we compare experimental results for the wavevector-dependent behavior of plasmons in a graphene sheet on SiC(0001) with that due to a filled band of surface states on semiconducting silicon. There are significant differences in behavior between the two systems, and the behavior predicted for a classical two-dimensional sheet of electrons. In particular, the damping increases with wavevector independent of any obvious inelastic scattering channel. The results illustrate the importance of finite-momentum, non-local potential effects for the dynamical behavior of electrically-isolated charge sheets.

The electronic properties of graphene, a monolayer of carbon atoms connected in a honeycomb lattice, has become the subject of much experimental and theoretical interest [49] since it became practical to produce single sheets of this graphitic material [59]. This due to a unique characteristic of the dispersion of its π -bands, which meet at a single symmetry point, the K-point of a hexagonal Brillouin Zone [60]. In conventional 2D electron-gas systems, in which charge is trapped in semiconductor inversion layers [6], heterostructure [61], or surface states [8], the single-particle energy $E(k)$ varies with the momentum k quadratically in parabolic bands at the Fermi energy, E_F . In graphene, the charge carriers propagate in π states which are linear through E_F with energies, $E = |\hbar k|v_F$ (\hbar -reduced plank constant) and extremely high Fermi velocity, $v_F \sim 1/300c$ (c = speed of light). The effective mass, $m^* = \hbar k_F/v_F$, is much lower than that of particles in a parabolic band, such that electron-electron collisions are more likely to occur, creating

¹ The work in section 2. was published in Ref. [17]

conditions for intriguing relativistic electro-dynamics in a weakly interacting 2D electron system [62].

We report experimental results for the wavevector-dependent behavior of the frequency of the two-dimension π -plasmon, $\omega_\pi(q)$, a collective oscillation of the π -band charge density which propagates within the graphene sheet. This low-energy “sheet-plasmon” mode is different to the bulk π plasmon mode, which is a collective excitation of the π -valence electrons in bulk graphite [63]. The graphene π -plasmon mode is a strictly 2D mode whose energy decreases continuously to zero in the longwavelength (classical) limit $q \rightarrow 0$. Recent calculations of the dynamical dielectric function $\epsilon(q, \omega)$ [64] indicate that the 2D graphene polarizability is very different to that of systems studied to date with parabolic band dispersion [65]. Accordingly, in this paper we compare and contrast the “sheet-plasmon” dispersion and lifetime characteristics of graphene on SiC(0001) with that of a 2D electron gas, of similar charge density $n \sim 10^{13}$ free-carriers cm^{-2} , trapped in a surface state on semiconducting silicon [8]. In both cases, the 2D charge layer is isolated from its substrate charge by a charge inversion layer and Schottky potential barrier. The reduced screening of the sheet-charge electric field produces strong non-local field effects, increasing with increasing wavevector q [66]. In the case of graphene, the onset of Landau damping is not observed at $q \sim k_F$, sheet plasmon continuing to disperse at large wavevectors, $q > k_F$.

A single layer of graphene was prepared on a 6H-SiC(0001) crystalline wafer surface ($0.1 \, \Omega \, \text{cm}$ resistivity) by solid state graphitization [67]. The sheet structure has been well characterized as weakly coupled to the substrate SiC, floating on a carbon-rich $(6\sqrt{3} \times 6\sqrt{3})R30^\circ$ interfacial superstructure [57, 68]. As a comparison, a 2D electron

gas of same charge density was prepared by firstly depositing one monolayer of silver atom onto a Si(111)-(7 × 7) reconstructed surface of a n-type silicon wafer (15 Ω cm resistivity) to form Si(111)-($\sqrt{3} \times \sqrt{3}$)-Ag and following certain silver adatom deposition at elevated temperature around 600K. Measurements were performed in ultrahigh vacuum (2×10^{-10} Torr base pressure), using high resolution angle-resolved reflection electron-energy-loss spectrometer (HREELS) with a setting of medium energy resolution of ~ 10 meV to obtain strong signal. The momentum (slit) resolution is better than 0.01 \AA^{-1} .

In order to identify the origin of loss peak from graphene or SiC substrate. HREELS measurements were also taken on a bare hydrogen-etched SiC(0001) wafer surface prepared by annealing SiC wafer at elevated temperature until a sharp hexagonal 1×1 LEED pattern was observed. The temperature was monitored and controlled to lower than 1050 C° so as not to form any carbon accumulated surface reconstruction. [58, 67, 69] Figure 4.4 shows HREEL spectra of a bare SiC(0001) surface which has three energetically equidistant prominent loss peaks at 116 meV, 233 meV and 349 meV due to polarized lattices vibrations, called "Fuchs-Kliwer (F-K) surface phonons" [70], and no dispersion was observed in off-specular spectra within resolution setting ~ 10 meV. These peaks are multiple scattering from the same excitation, which is typical for ionic materials, for instance ZnO [71] and GaAs [72].

Figure 4.5 shows the energy-loss peak in the HREELS spectrum of low energy electrons back-scattered from graphene on SiC(0001), increasing and dispersing with increasing momentum transfer parallel to the surface, q given in \AA^{-1} . All data are shown for positive momentum transfer at 300k. Comparing with dramatic energy dispersion

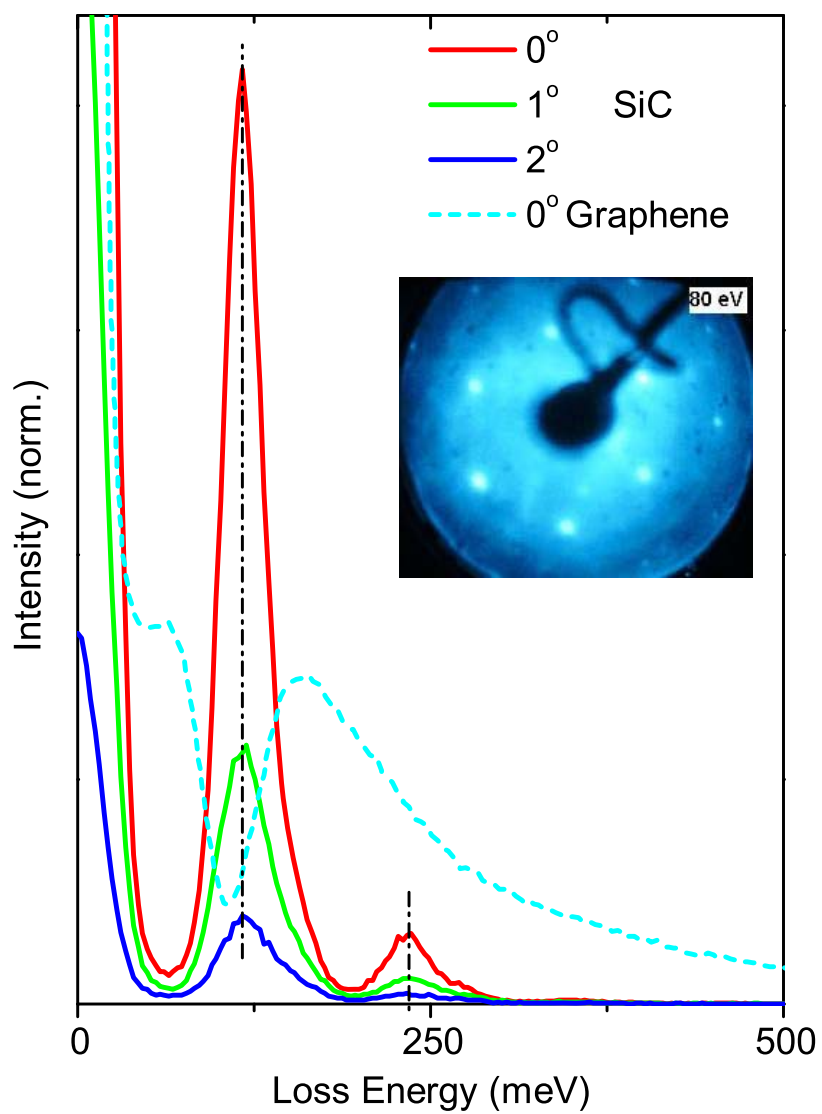


Fig. 4.4. Normalized HREEL spectra of SiC surface and graphene on SiC. The inset shows the LEED pattern of SiC(0001)(1 × 1) surface taken at incident electron beam of 80 eV.

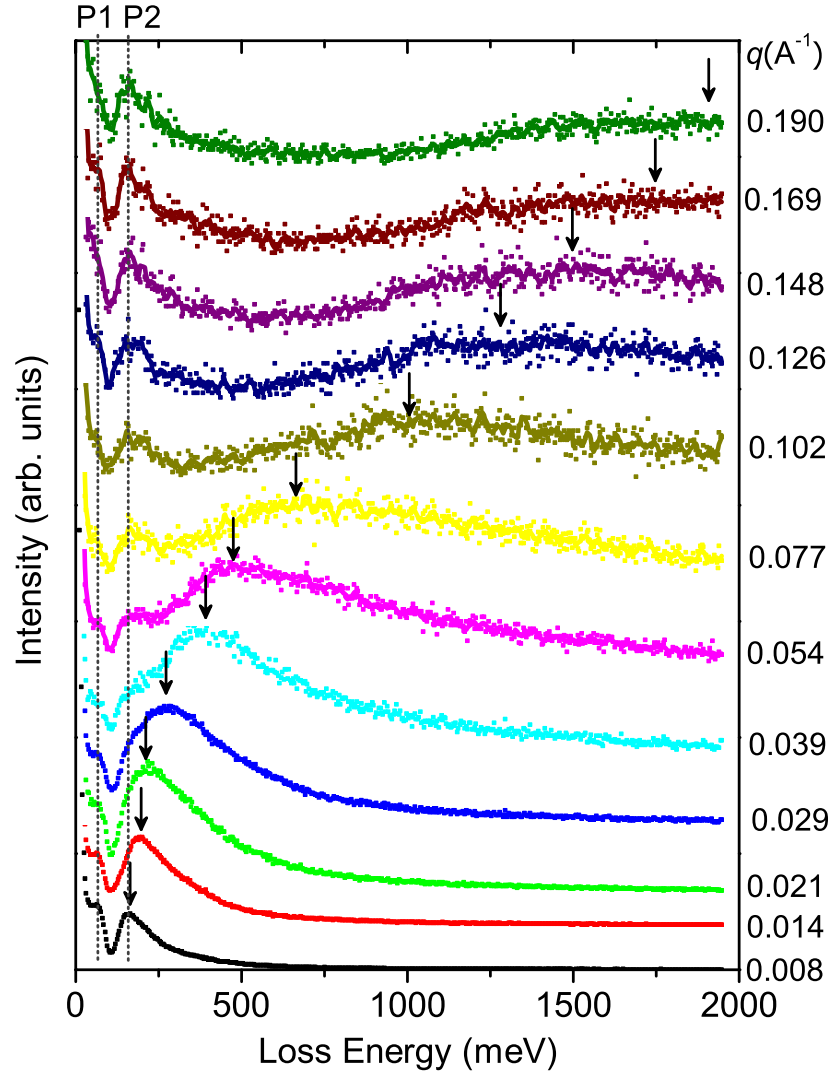


Fig. 4.5. Sheet-plasmon loss peaks of graphene dispersing with increasing momentum transfer q . The lines in magnified spectra at large momentum transfer ($> 0.5 \text{ \AA}^{-1}$) are smoothed by averaging 3-5 nearest neighbor points. Also the last two spectra (green, brown) with very broad peaks were partially presented in this figure as result of figure layout, but the extensively scanned portions from 2000 meV to 2500 meV were included in data analysis of peak positions. The incident electron beam energy is 20.29 eV.

(0.2 \sim 2 eV), the non-dispersing low loss peaks P1 (67 meV) and P2 (159 meV) were superimposed on the background and sheet-plasmon peak loss structure. They became more visible as the plasmon intensity dropped with increasing off-specular angle θ_s . The peak P1 was reported previously on HREELS study of graphitic surface as low energy π plasmon [47, 73]. Also the peak P2 originates from Fuchs-Kliwer optical phonons of both graphitic structures on SiC substrate [73, 74] and SiC surface itself [75, 76]. The energy of F-K phonon was slightly dependent on surface structure of SiC, however the change of loss energy due to momentum dependence [76] or structure dependence [75] is way-off comparable to the energy diapersion range of sheet plasmons, from 0.2 eV to 2 eV within $q < 0.2 \text{ \AA}^{-1}$. It is worthy of mention that the symmetry of F-K phonon is broken when a graphitic structure forms on SiC surface. As a result, there is convolution of peaks due to the F-K phonons, sheet plasmons and "Drude" background, dashed curve in Fig. 4.4. The probing depth q^{-1} of the electron scattering experiment can be estimated by [14]

$$q^{-1} \cong \frac{2E_0}{k_i \hbar \omega_{loss}} \quad (4.1)$$

which is related to the decay length of dipole field from the surface both into the substrate and into the vacuum. For our HREEL spectra, an electron energy $E_0 = 20.29 \text{ eV}$, $k_i = 2.3 \text{ \AA}^{-1}$ and phonon energy $\hbar \omega_{loss} = 116 \text{ meV}$, the probing depth $q^{-1} \approx 150 \text{ \AA}$ is deep enough to "look" through top layers and map the electronic and structure properties of the substrate, resulting in appearances of F-K phonon peaks at all thicknesses.

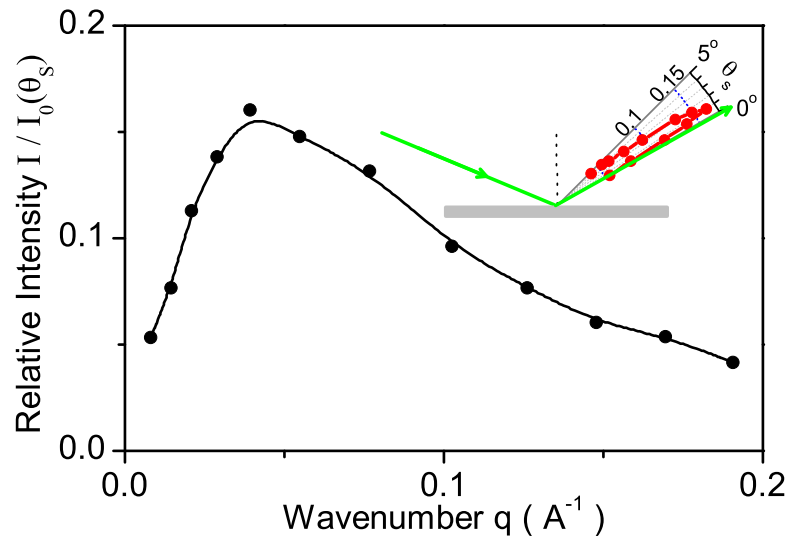


Fig. 4.6. Scattering cross-section intensity varying with q . The angular distribution profile (inset diagram, red line) of loss intensity is strongly peaked around 1.5° to specular direction (green line). Scattering angle ($0^\circ \leq \theta_s < 5^\circ$) is magnified by 3 times in polar coordinates.

In Fig. 4.6, the relative intensity of the sheet-plasmon loss peaks increase at small momentum transfer $q \leq 0.05 \text{ \AA}^{-1}$ before decreasing at larger $q > 0.05 \text{ \AA}^{-1}$. This small-angle scattering is the characteristic of dipole scattering coupling to an image-charge electric field predominantly normal to the 2D-sheet surface plane [77]. Information on the sheet-plasmon collective excitations is given by the imaginary part of the surface response function[2]:

$$g(q, \omega) = \int d\vec{r} \int d\vec{r}' e^{q \cdot z} \chi(\vec{r}, \vec{r}', q, \omega) V_{ext}(\vec{r}', \omega) \quad (4.2)$$

where the external “image-charge potential” has the form:

$$V_{ext}(\vec{r}', \omega) = -\frac{2\pi}{q} e^{q \cdot z} e^{iq \cdot r} e^{i\omega t} \quad (4.3)$$

for wavevector q and position vector r in the sheet plane ($z = 0$) of excitations with energy loss, $E_{\text{loss}} = \hbar\omega$. The polarizability is expressed by the frequency-dependent charge-density response function $\chi(\vec{r}, \vec{r}', q, \omega)$, and the imaginary part of $g(q, \omega)$ is a peak in the recorded energy-loss spectrum. The loss peaks in Fig. 4.5 gave the sheet-plasmon energy in Fig. 4.7.

The Fermi energy of the graphene layer is raised 0.57 eV above the Dirac-energy crossing point of the π bands, with $k_F \sim 0.08 \text{ \AA}^{-1}$ corresponding to a 2D charge density $n \sim 2 \times 10^{13} \text{ cm}^{-2}$. The Fermi level is pinned within the 3 eV bulk band gap of the substrate and effectively decoupled from charge excitations in the substrate [78].

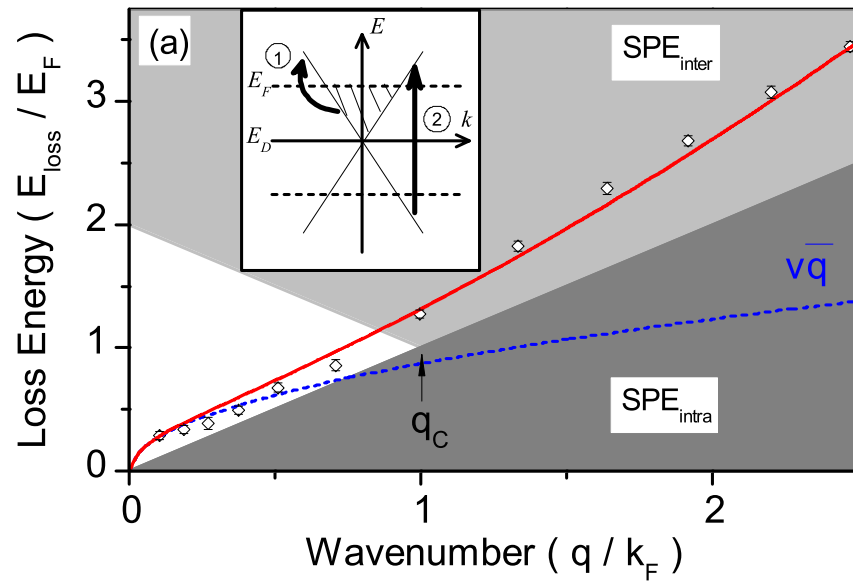


Fig. 4.7. Plasmon dispersion for graphene of similar charge density, ($E_F = 0.57$ eV) $n \sim 2 \times 10^{13} \text{ cm}^{-2}$ and schematic band structures (inset diagrams) show the origin of single-particle excitations SPE (1) intraband and (2) interband. Graphene is ambipolar with, electron and hole carriers in separate π , π^* bands.

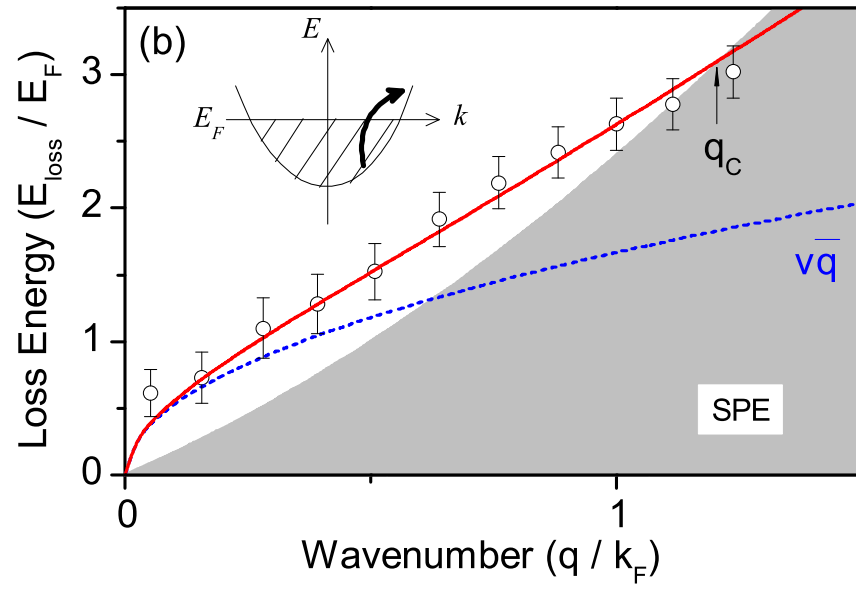


Fig. 4.8. Plasmon dispersion for Si(111)-($\sqrt{3} \times \sqrt{3}$)-Ag surface-state band ($E_F = 0.19$ eV), $n \sim 2 \times 10^{13} \text{ cm}^{-2}$. The schematic band structure (inset diagrams) shows the origin of single-particle excitations SPE

Figure 4.7 and 4.8 compare the dispersion behaviors of the plasmon losses observed in the HREEL spectra from both surfaces. The different band structures (inset diagrams) produce different distributions of single particle excitations (SPE), plotted for both cases, Fig. 4.7 and 4.8, in relation to the \sqrt{q} -dispersion predicted for a 2D charge sheet of free electrons of the same number density. The first thing we note is that the plasmons in both cases have exactly the same \sqrt{q} dispersion as that for a classical 2D gas in the local-field approximation in the longwavelength limit [79]. Stern [32] expressed this, and higher-order, non-local field effects in a random-phase-approximation:

$$\omega_{2D} = [\frac{4\pi n e^2}{m^*(1 + \epsilon_0)}|q| + \frac{3}{4}v_F^2 q^2 + \dots]^{1/2} \quad (4.4)$$

The first-term (indicated by dashed lines in Fig. 4.7 and Fig. 4.8) is dependent on the areal charge density n , effective mass m^* and static dielectric constant ϵ_0 of the medium. The Fermi wavevector and the Fermi energy of graphene are given by $k_F = (4\pi n/g_s g_\nu)^{1/2}$ and $E_F = \hbar v_F k_F$, where $g_s = 2$ and $g_\nu = 2$ are the spin and valley degeneracies for graphene [64]. The data for graphene has best-fit parameters: $n = 1.9 \times 10^{13} \text{ cm}^{-2}$, $m^* = 0.077m_e$, and $\epsilon_0 = 10$ in the $q \rightarrow 0$ limit. The data for the surface state on Si(111)-($\sqrt{3} \times \sqrt{3}$)-Ag was fitted with $n = 1.9 \times 10^{13} \text{ cm}^{-2}$, $m^* = 0.24m_e$, and $\epsilon_0 = 11.5$, in agreement with the result of Nagao et al. [8, 66]. The full curves are the best fits to the data.

The second thing we note is that even though the longwavelength plasmons have almost identical dispersion at small q , the data deviates strongly from \sqrt{q} -dispersion behavior with increasing finite q . Also, this deviation is different in the graphene, the

data falling below the \sqrt{q} -curve for $0.1 \leq q/k_F \leq 0.5$, while that for the 2D surface state shows an increasing plasmon energy, E_P , relative to the Fermi energy, E_F . This behavior is surprising, given Stern's result (Eqn. 4.4) for the dispersion of a 2D electron gas within RPA, including finite wavevector non-local higher-order corrections. Equation 4.4 expresses the first-order correction in terms of the Fermi velocity v_F , which is at least an order of magnitude smaller in the 2D surface-state band.

Hwang and Das Sarma [64] have recently shown that the wavevector-dependent dynamical polarizability of graphene can be expressed:

$$\epsilon(q, \omega) = 1 + \nu_c(q)\Pi(q, \omega) \quad (4.5)$$

in which the 2D screened coulomb interaction, $\nu_c(q) = 2\pi e^2/\kappa q$, and κ is an effective dielectric constant in which dynamical screening effects are absorbed into the static constant ϵ_0 . The 2D dynamic polarizability is the sum of two terms representing the ambipolar nature of the free carriers in “doped” graphene [inset diagram, Fig. 4.7]:

$$\Pi(q, \omega) = \Pi^+(q, \omega) + \Pi^-(q, \omega) \quad (4.6)$$

with Π^+ , Π^- representing the polarizability, of holes and electrons excited up into the π^* states.

This prediction is borne out by the experimental results, Fig. 4.7. The non-local polarization of the hole band in graphene reduces the plasmon frequency below that of the classical 2D electron gas for $q < 0.5k_F$. There is no such depolarization effect in

the 2D surface-state system, Fig. 4.8. The non-local effects produce a well-established increase in the plasmons frequency at larger q [80]. With increasing wavevector, $q > k_F$, we see a third difference in behavior between the graphene and the 2D surface state. In Fig. 4.7 and 4.8, we show also the onset of the continuum dispersion of single-particle excitations (SPE) throughout (q, ω) space (shaded regions). The plasmon in the surface-state system, Fig. 4.8, disappears into the continuum of intraband transitions at $q_c \sim 0.14 \text{ \AA}^{-1}$ beyond which point it dissolves into incoherent electron-hole pairs which form a continuum Drude background of energy loss excitations. In contrast, the graphene plasmons, Fig. 4.7 avoids the linear SPE edge due to intraband excitations, entering the continuum of interband excitations at $q_c \sim 0.08 \text{ \AA}^{-1}$ (the different energy scales of the intra- and inter-band excitations are illustrated on the band diagrams inset, Fig. 4.7). However, all of the spectral weight of the graphene mode is not transferred to the inter-SPE, the 2D π -plasmon continuing to disperse at higher $q > k_F$.

Another surprising feature of both dispersing plasmon modes is an increasing lifetime broadening even within the energy gap of SPE.

Figure 4.9 compares the observed change of this damping with increasing finite q for these two systems. Both curves show a linear increase in the plasmon damping with increasing wavevector q . The slope of the curves are roughly in the ratio of their Fermi velocities: $v_F(\text{G})/v_F(\text{SS}) = (1.1 \times 10^6 \text{ m/s}) / (5.3 \times 10^5 \text{ m/s}) \sim 2.08$. The similarity of these two ratios implicates the damping has a close relation to inter- and intra-band transitions, since v_F involves unique information m^* from the band structures in the case of comparison between two systems with similar electron density n . However, to fully understand this broadening, surface loss functions are required to be derived and

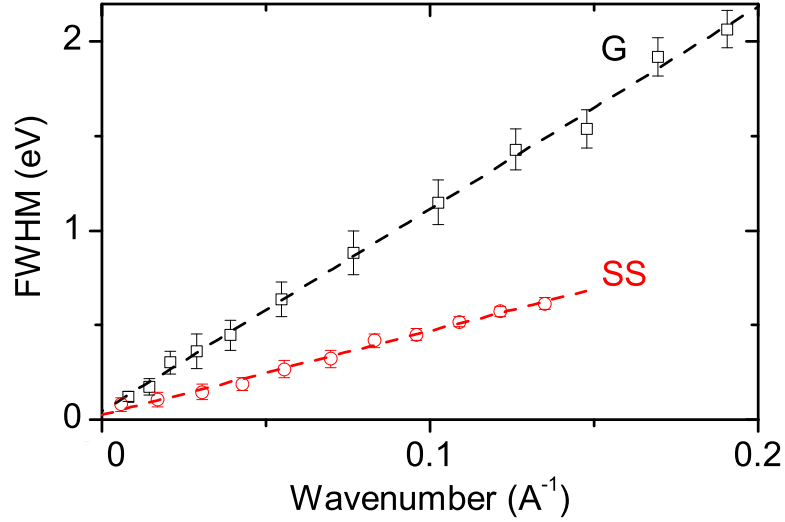


Fig. 4.9. Plasmon damping [full-width at half-maximum (FWHM) of loss peak, Fig. 4.5] plotted as a function of momentum transfer q for (G) graphene and (SS) surface-state 2D systems.

calculated. A similar effect has also been reported for a 2D electron gas formed in a GaAs/AlGaAs quantum-well as evidence for enhanced correlation effects [61]. Another contribution factor is the small magnitude of $k_F \sim 0.08 \text{ \AA}^{-1}$, giving plasmon wavelengths $\lambda_p \sim 70 \text{ \AA}$, which are large compared with the lattice size $a \sim 1.5 \text{ \AA}$. These sheet plasmons do not scatter off the lattice.

4.3 Conclusion

In summary, we find a number of intriguing differences between the sheet-plasmon behavior of a sheet of charge effectively isolated from screening by substrate excitations. These differences are manifest with increasing wavevector q , and have been widely predicted as due to non-local corrections. [61, 64, 66] These non-local corrections effectively

increase the restoring force (potential) of the plasmon harmonic oscillator, and contribute to damping increasing with q irrespective of Landau damping due to excitations of single-particle, electron-hole pairs on the Fermi surface. These effects are magnified in graphene due to the very limited amount of phase space available to electron scattering processes, and the increased electron-electron elastic scattering due to the very high Fermi velocity v_F . The dynamical screening behavior is, as a consequence, very different to that of the usual 2DEG.

Chapter 5

Plasmon Dispersion of Multi-layer Graphene

It is well known that a single graphene layer is a zero-gap semiconductor while graphite is a semimetal. One effect of the weak coupling between the graphene layers is the opening of a gap at Fermi level E_F and the reducing of number density of carriers in the π^* conduction band. Therefore it is interesting to investigate how the electronic structure changes as a function of the number of graphene layers and how the interaction or coupling between each layers affect dispersion behaviors. In this chapter, dispersion behaviors of multi-layer graphene at various thicknesses were characterized by HREELS and the results were discussed and compared to characterizations of other experimental methods.

5.1 Measurements of Multi-Layer Graphene

HREELS measurements were taken on 2 ML, 3 ML, 5 ML graphene prepared on SiC surface. The kinetic energy of incident electrons was 20.29 eV and the scattering angle was from 0° to 5° . The maximal scattering angle in each spectrum was limited by the drastic intensity drop of loss peaks due to the dipole scattering. In most of our HREELS measurements, 5° was the limit for obtaining a distinguishable spectrum from multi-layer graphene, and the step of angle was 0.5° . Figure 5.1 shows the orientation

of steps and the width of terrace (~ 350 nm for 3 ML, ~ 700 nm for 5 ML). There is a 2° -off, 5° -off, 5° -off axis for 2 ML, 3 ML, 5 ML graphene, respectively.

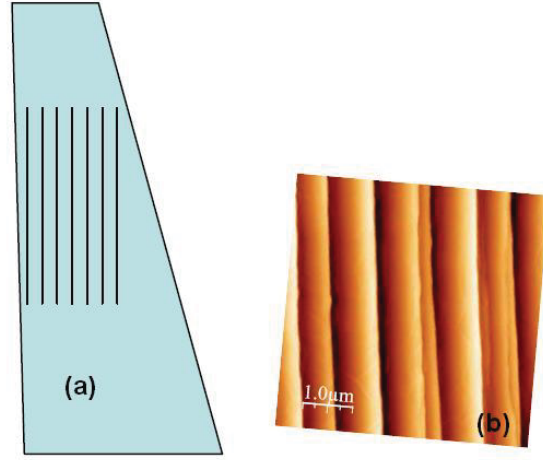


Fig. 5.1. (a) SiC(0001) sample with steps; (b) SEM image of terrace on SiC(0001).

Each set of spectra for a certain thickness is shown in following figures: Fig. 5.2 for 2 ML, Fig. 5.3 for 3 ML and Fig. 5.4 for 5 ML. Their dispersion curves, including 1 ML, are plotted in the same figure for comparison in Fig. 5.5.

Fig. 5.2 shows spectra of 2 ML graphene which has a similar dispersion behavior and linewidth profile of loss peaks as that of single-layer graphene. Those two non-dispersing peaks still exist in the spectra with loss energy of 68 meV (not obvious in this figure, but observable at a larger magnification of spectra in the low-energy range) and 152 meV (aligned with dot line), respectively.

The biggest difference in structures of spectra is the appearance of two peaks in spectrum at the momentum transfer of 0.068 \AA^{-1} . This feature is shown in the inset of

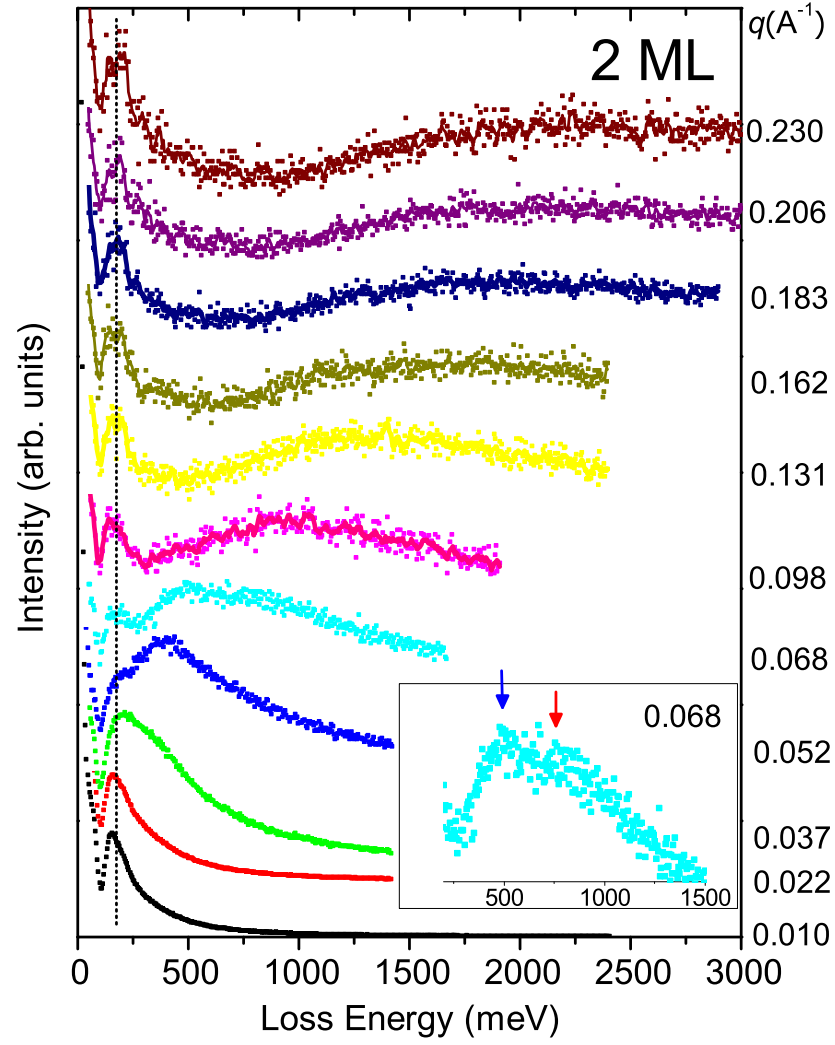


Fig. 5.2. HREEL spectra of two layers of graphene on SiC. The spectra at large momentum transfer are smoothed by averaging 5-7 nearest neighbor points for visibility (superimposed lines). The inset shows a splitting of the wavevector $q = 0.068 \text{ \AA}^{-1}$.

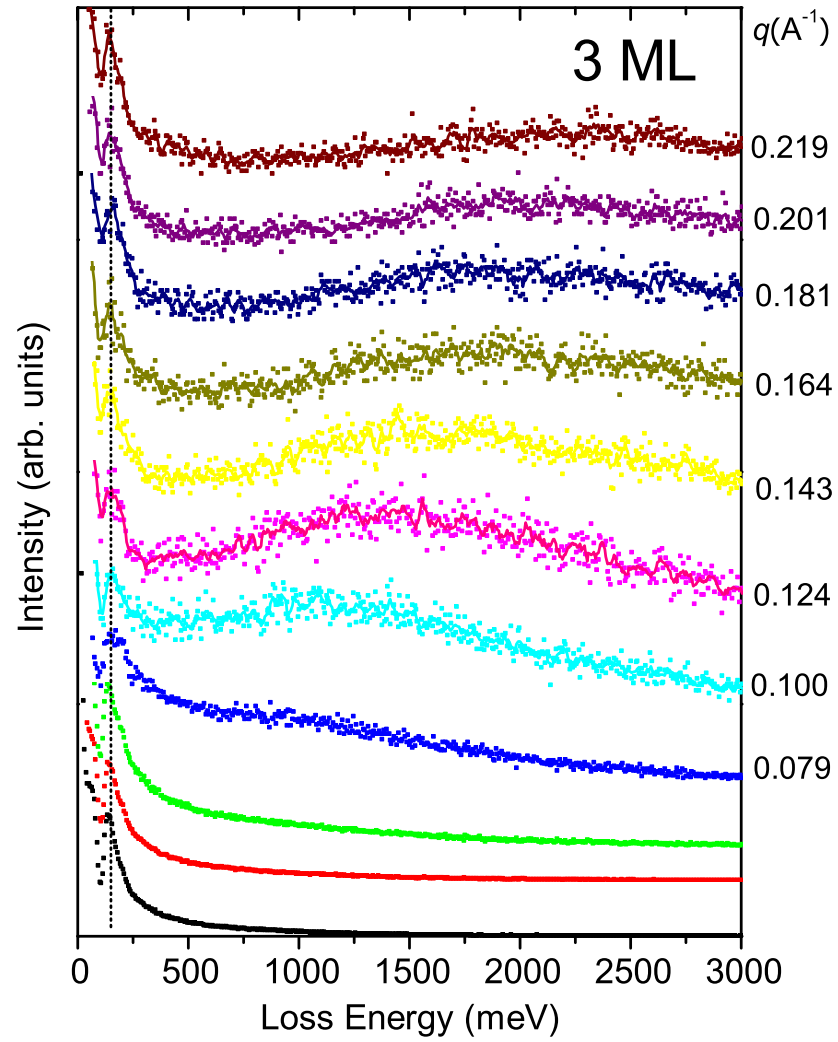


Fig. 5.3. HREEL spectra of three layers of graphene on SiC. The spectra at large momentum transfer are smoothed by averaging 5-7 nearest neighbor points for visibility (superimposed lines).

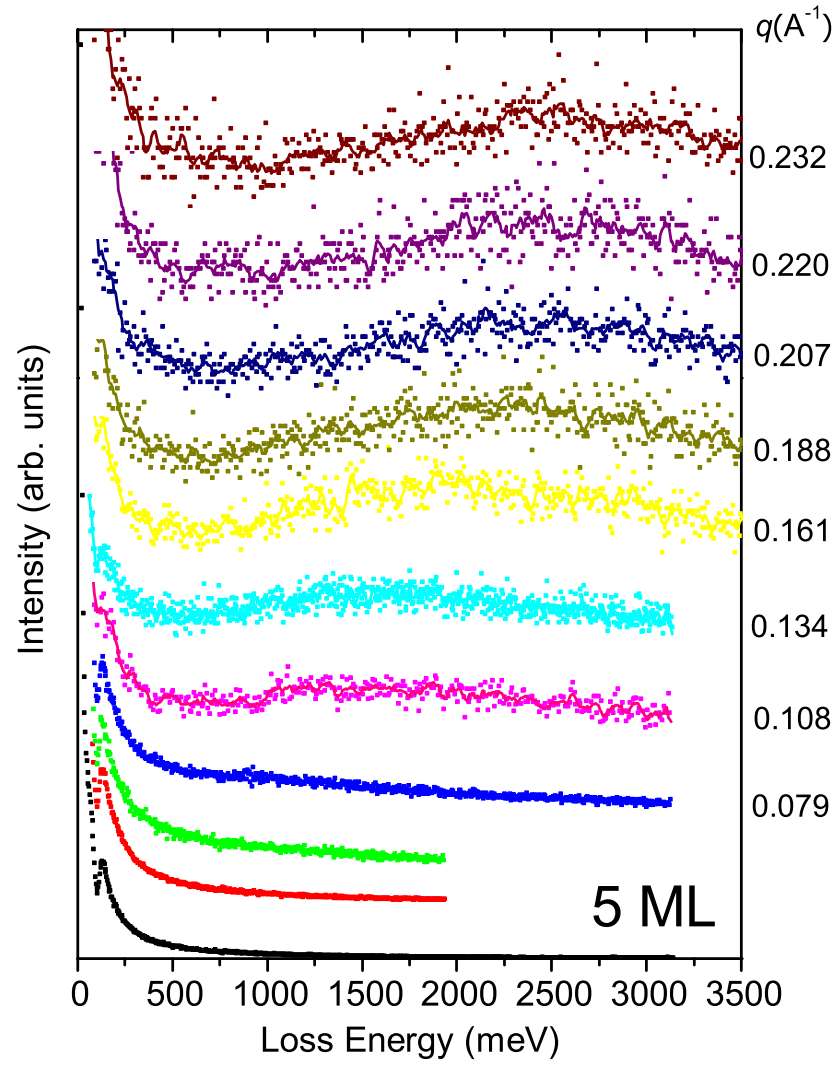


Fig. 5.4. HREEL spectra of five layers of graphene on SiC. The spectra of large momentum transfer are smoothed by averaging 5-7 nearest neighbor points for visibility (superimposed lines).

Fig. 5.2 with arrows indicating two peak positions, 545 meV (blue arrow) and 825 meV (red arrow).

Fig. 5.3 shows spectra of 3 ML graphene. In the range of large momentum transfer, it has a similar dispersion to that of 1 ML and 2 ML graphene. However, except those two non-dispersing peaks at 68 meV and 147 meV, no dispersing peaks is observed in the range of small momentum transfer $q < 0.079 \text{ \AA}^{-1}$.

Fig. 5.4 shows spectra of 5 ML graphene. The dispersion starts from $q = 0.079 \text{ \AA}^{-1}$, and continue dispersing with a very broad linewidth. Also, two non-dispersion peaks, 63 meV and 131 meV, are still seated on all spectra.

In Fig. 5.5, loss energy vs. wavenumber of graphene layers of four different thickness are plotted together to make a comparison. The critical wavenumber $q^* \sim 0.079 \text{ \AA}^{-1}$ indicates where dispersing peaks are observed. Summarizing for dispersion of four different thicknesses, for 1 ML and 2 ML, the dispersion start from very small $q < 0.01 \text{ \AA}^{-1}$, whereas dispersions of 3 ML and 5 ML start after certain $q^* \sim 0.079 \text{ \AA}^{-1}$. The dispersion behaviors of all thickness after $q^* \sim 0.079$ are similar in general trend, i.e. loss energy increases as increasing momentum transfer. The loss energy for a given q increases with increasing thickness (the curve of 2, 3, 5 ML stay above 1 ML), indicative of a different fillings of the π^* band. In spectrum of 2 ML graphene at $q = 0.068 \text{ \AA}^{-1}$, two loss peaks appear and one of them disappears in following measurements, and the slopes of dispersion in the range $q > q^* = 0.079 \text{ \AA}^{-1}$ are different. The non-dispersing

¹ The exact q^* value is unable to obtain due to the 0.5° step between each measurements limited by angular resolution of analyzer, giving only a range for q^* ($0.068 \text{ \AA}^{-1} < q^* < 0.079 \text{ \AA}^{-1}$) from two neighbor measurements.

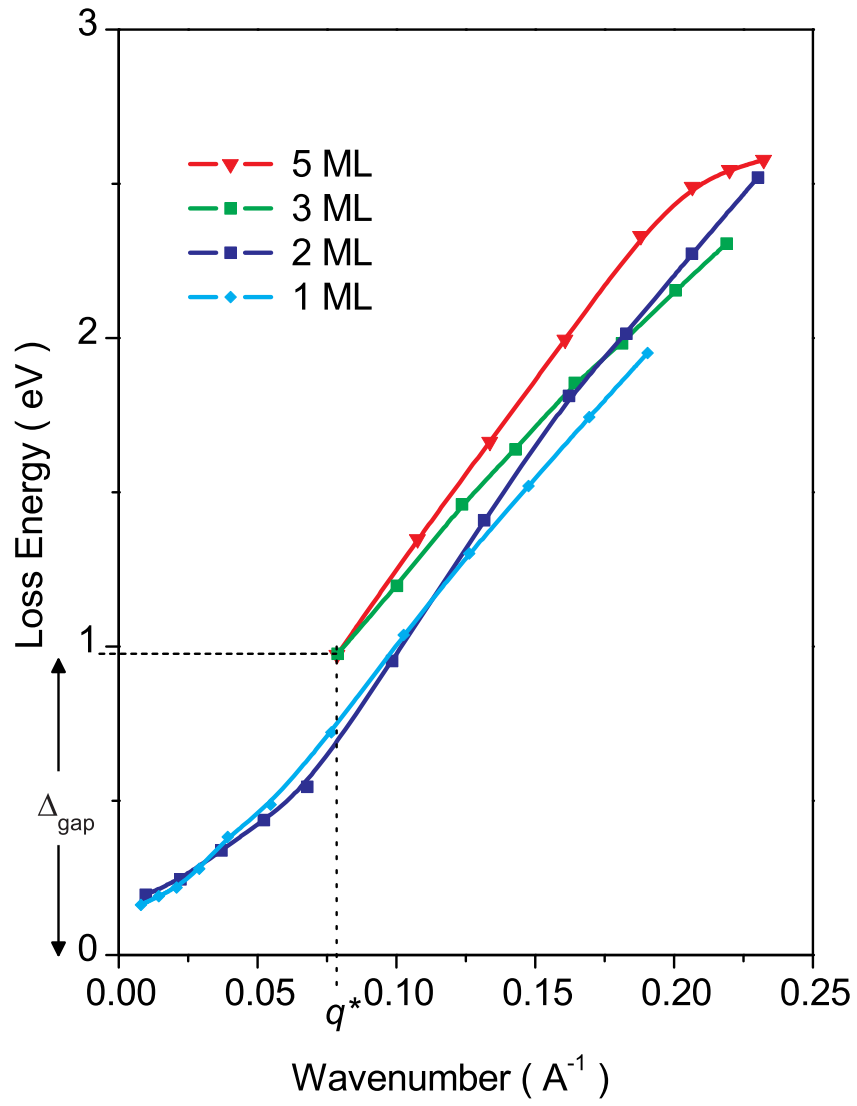


Fig. 5.5. Dispersion behaviors of graphene layer of various thickness

F-K phonon peaks ($P1 \sim 67$ meV and $P2 \sim 159$ meV, Fig. 4.5) always exist in spectra of all thickness.

5.2 Discussion

For 1 ML and 2 ML layers, the dispersion for $q \rightarrow 0$ appears to tend towards a finite energy. The value at $q = 0$ cannot be measured since the loss peak disappear into the intense elastic zero-loss feature.

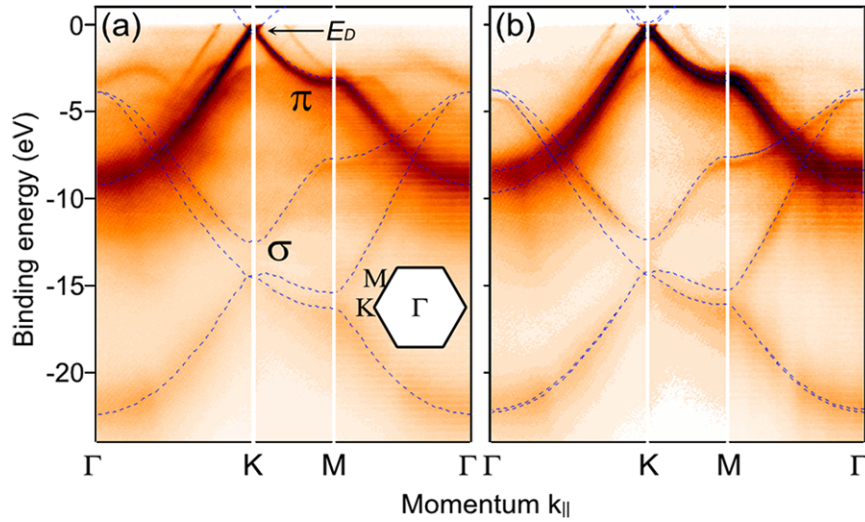


Fig. 5.6. Photoemission images revealing the band structure of (a) single and (b) bilayer graphene along high symmetry directions $\Gamma - K - M - \Gamma$. The dashed (blue) lines are scaled DFT band structure of freestanding films. Inset in (a) shows the 2D Brillouin zone of graphene. From Ref. [81]

To understand this behavior in Fig. 5.5, we consider the band structure of graphene at the corner (**K** point) of the hexagonal Brillouin zone due to delocalized

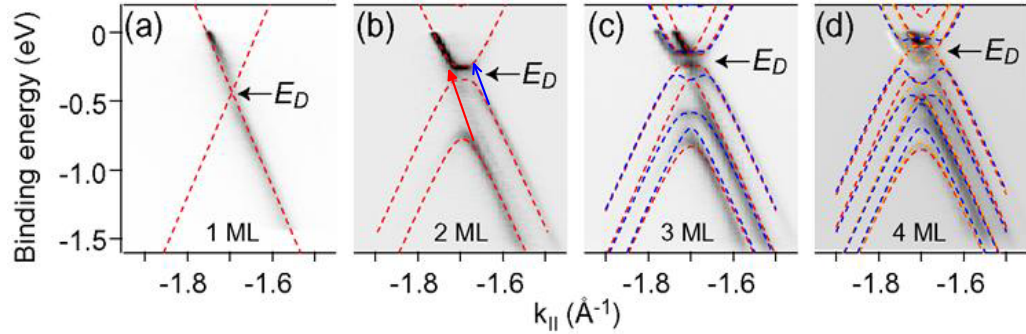


Fig. 5.7. (a)-(d) The π and π^* bands near E_F for 1-4 graphene layers, respectively. $k_{\parallel} = -1.703 \text{ \AA}^{-1}$ corresponds to the \mathbf{K} point. The dashed lines are from a calculated tight binding band structure, with band parameters adjusted to reproduce measured bands. Red and orange (light gray) lines are for Bernal-type (ABAB and ABAC) stackings, while blue (dark gray) lines are for rhombohedral-type stackings. From Ref. [81]

π and π^* states developed from p_z orbitals which are very sensitive to interaction between layers, including stacking order of multi-layer graphene. Because 2 ML graphene lattice contains two bi-atom unit cells of graphene, the π and π^* band are split by interlayer coupling, as is evident in the photoemission spectra of bilayer graphene, Fig. 5.6 [81]. The comparison between band structures of single and bilayer graphene in Fig. 5.7(a)(b), shows a similarity of the underlying electronic structure which renders similar sheet plasmon dispersion behavior (Fig. 5.5). However, the HREEL spectrum of the 2ML graphene has two peaks coexisting (inset of Fig. 5.2) due to the splitting of the π bands. New transitions are excited from the highest π states to lowest π^* states ($\Delta E \sim 0.5$ eV corresponding to peak 545 meV indicated by blue arrow in both figure) and from the second highest π states to the lowest π^* states ($\Delta E \sim 0.8$ eV corresponding to peak 825 meV indicated by red arrow in both figure), as shown in detailed band structure of 2,

3, 4 ML graphene in Fig. 5.7 [81]. These π band splittings increase with the number of layers and band-gap opens up. This newly opened energy gaps also result in the missing of loss peaks in spectra of 3 ML (Fig. 5.3) and 5 ML (Fig. 5.4) at momentum transfer $q < q^*$. The gap between π and π^* of 3 ML graphene is around 0.5 eV estimated from the photoemission spectrum, and is comparable to the measured loss energy $0.7 \sim 1.0$ eV at q^* if following considerations are taken:

1. No direct transition induced by low-energy electron excitation is allowed due to requirement of energy and momentum conservation along the surface. Since electron wavelength is not negligible compared to an optical experiment, any amounts of energy supplied for electrons transition is associated a finite momentum transfer. This make the transition route in band diagram tilted at a certain angle dependent on the impact energy and incident angle of incident electrons. The inset of Fig. 5.8 shows how the necessary energy (ΔE) to complete a interband transition is higher than the gap energy (Δ_g). Calculation can be made if detailed structure is mapped around \mathbf{K} point. It is also worthy mentioning that the incident of gapping in the multi-layer structur increases the density of states for electronic transitions across the gap. The monolayer has zero gap and steeply rising linear bands so that no such transitions are observed.

2. It is hard to estimate the measured loss energy for smallest transition energy ΔE due to the step between each HREELS measurements, which is limited by angular resolution of scattering angle. Roughly, if taking 2 ML layer spectrum around q^* as a reference gives ΔE in the range from 700 meV to 976 meV.

In the aspect of quantitative analysis, both band structure information and density of state of these bands are required, and interlayer interaction such as Coulomb

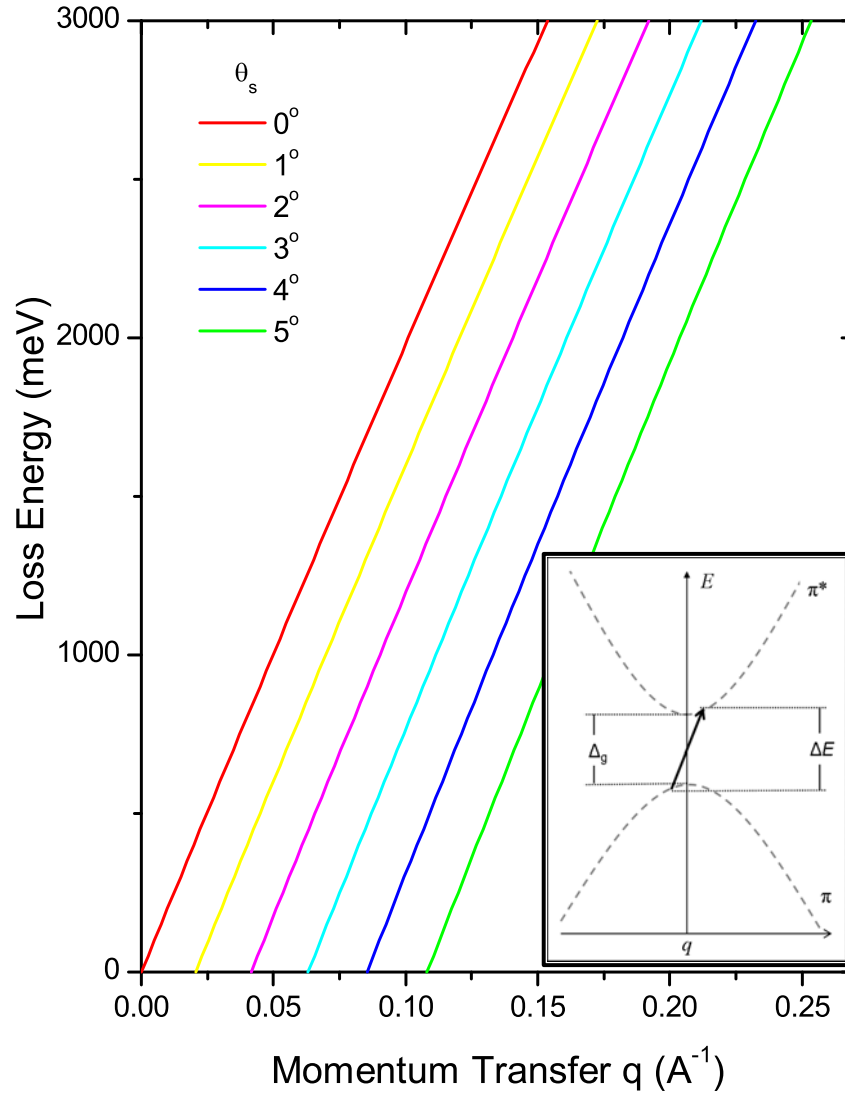


Fig. 5.8. The loss energy associated with momentum transfer according to the properties of beam energy. The route of transition in band diagram has the same slope. Inset shows the schematic of transition route induced by low energy electron excitation, $\Delta E > \Delta_g$.

interaction and intercalation between layers have to be determined and incorporated into the Hamiltonian.

5.3 Conclusion

In summary, multilayers change the band structure about the Dirac point drastically. The opening of a gap changes the dispersion of the π , π^* -bands from linear to parabolic with a concomitant increase in the density of states for q -dependent interband transitions. These transition modify the dielectric response and loss function in the vicinity of q^* . We see new features relating to the lifting of the degeneracy of the π , π^* -bands. These, in turn, modify the sheet plasmon energy, and the onset of dispersions. The dispersion is not sensitive to the band structure at large momentum transfer, but the plasmon energy is shifted by the increased number of interband transitions at finite q , as expected from dielectric theory.

Chapter 6

SUMMARY AND FUTURE STUDY

6.1 Summary

In this work, we investigated the dispersion behaviors of sheet plasmons on two different two-dimensional electron systems by using angle-resolved high resolution electron energy loss spectroscopy (HREELS).

6.1.1 Si(111)-($\sqrt{3} \times \sqrt{3}$)-Ag

Si(111)-($\sqrt{3} \times \sqrt{3}$)-Ag was prepared in ultrahigh vacuum by depositing silver on Si(111)-(7×7) surface at elevated temperature, the process was controlled and monitored by QMS and LEED. HREELS measurements were performed on these surface at a series of scattering angles to characterize wavenumber-dependent energy dispersions of sheet plasmons. The measurement on pristine Si(111)-($\sqrt{3} \times \sqrt{3}$)-Ag presented a well-defined plasmon dispersion, which was in excellent agreement with theoretical calculation based on non-local response theory. Further deposition of silver adatoms on pristine Si(111)-($\sqrt{3} \times \sqrt{3}$)-Ag surface, a two-dimensional adatom gas phase was formed and destroyed when the coverage exceeded a critical coverage. This phase characterized by the electron density fluctuation, was brought out in dispersion behaviors by showing a different slope and energy. For the first time, a "smooth" transition from two-dimensional plasmon to three-dimensional plasmon was observed in measurements on further deposited surfaces.

The opening of a gap in the longwavelength limit marked this transition into a three-dimensional plasmon, moreover a calculation of gap energy based on the simple model of surface plasmons verified its 3D-type origin. Two features of the unique electronic structure of Si(111)-($\sqrt{3} \times \sqrt{3}$)-Ag rendered this smooth transition, i.e. 1. the space-charge region in silicon works as a carrier reservoir which limited the electron density of surface; 2. the open surface was accessible by homo-adatoms to perform geometric transformation in real space. As silver deposition continued, the conventional surface plasmon was finally observed at the deposition of 20 ML of silver adatoms.

In the field of the film growth, the curvature features of dispersion curve was also in close relation to the micro-morphology of surface, the grainy size of silver micro-crystal was estimated by examining the kink of dispersion curve due to the confinement of plasmons.

6.1.2 Graphene

For the first time, we identified and measured the wavevector-dependent dispersion behavior of graphene on SiC(0001) surface in ultrahigh vacuum by HREELS. The dispersion behavior of two-dimensional electrons gas system in the single-layer graphene, was similar to 2DEG in Si(111)-($\sqrt{3} \times \sqrt{3}$)-Ag due to very likely band structure of these two systems. The loss intensity profile was strongly peaked around specular direction, indicative of a dipole-scattering mechanism, and justified the fitting based on dielectric response theory, i.e. Stern model which also gave consistent results to measurements by other techniques. A strong damping was not observed in graphene layer compared to the Landau damping of Si(111)-($\sqrt{3} \times \sqrt{3}$)-Ag, since the plasmons with high energy induced

by high electron density of 2DEG stayed above the single-particle-excitation continuum and never entered this damping region due to intra-band transition. However, another predicted damping region, which only exists in a two-dimensional system due to inter-band transition, had little observable effect on the plasmon damping of graphene even plasmons entering this region which was inconsistent with the theoretical prediction. The full width at half maximum (FWHM) of graphene showed a linear increasing with wavevector and we also found out that decay rates were proportional to the Fermi velocity of each 2DEG. With few theoretical work on the mechanism of this decaying, a satisfied quantitative explanation was not yet obtained so far.

The dispersion of stacked graphene layers were also investigated by HREELS. They showed a similar dispersion behavior except in the region smaller than critical wavevector q^* which was roughly equal to Fermi wavevector. An explanation was given based on the inter-band transitions and band structures mapped by photoemission, where the inter-band transition excited by low-energy electrons was associated a finite momentum transfer, so that the transition route was tilted in band diagram.

6.1.3 Impact of the research

The extended study on a well-established strict two-dimensional electron gas system, i.e. Si(111)-($\sqrt{3} \times \sqrt{3}$)-Ag, revealed an electrodynamic transition from 2D electron gas to 3D electron gas by measuring dispersion behaviors of sheet plasmons in two-dimensional physics.

The first-time measurements and characterizations of sheet plasmons of the recently experimentally available strict 2D electron gas system, i.e. graphene, suggested a

characteristic 2D behavior of condensed 2D electron gas, which had the physical significance in identifying electron-electron correction.

6.2 Future Study

Preparation and study of the electronic properties of a strictly 2D-electron gas are of basic interest. A theoretical study shows a very interesting evolvement of charge profile with stacked graphene layers[82]. Our HREELS measurements collected the averaged information of multi-layer graphene since the probing length was equivalent to 50 ML graphene. A thicker layered graphene system could be used to study the dynamics of the coupling and screening of 2DES and compared with well-studied graphite bulk, given the exciting 2DEG character of single layer graphene.

It is a technical challenge to take reflection EELS on a free-standing graphene layer, but it would disclose how much influence the SiC substrate have on the epitaxial graphene layer, although they show the same band structures in photoemission experiments, whereas the electron density of the epitaxial graphene layer 10 times larger than that of free-standing graphene layer.

The doping of electron-donor atoms can control the gap between π and π^* band and electron density of bi-layer graphene [83], which provide us another flexible 2DEG platform to investigating the damping mechanism of 2DEG with capabilities of switching-on and off interband transitions and of tuning phase space.

Bibliography

- [1] H. Raether. *Excitation of Plasmons and Interband Transitions by Electrons*. Springer-Verlag, Berlin, 1980.
- [2] A. Liebsch. *Electronic excitations at metal surfaces*. Plenum, London, 1997.
- [3] M. Rocca. Low-energy EELS investigation of surface electronic excitations on metals. *Surf. Sci. Rep.*, 22:1, 1995.
- [4] J. M. Pitarke, V. M. Silkin, E. V. Chulkov, and P. M. Echenique. Theory of surface plasmons and surface-plasmon polaritons. *Rep. Prog. Phys.*, 70:1, 2007.
- [5] C. C. Grimes and Gregory Adams. Observation of Two-Dimensional Plasmons and Electron-Ripplon Scattering in a Sheet of Electrons on Liquid Helium. *Phys. Rev. Lett.*, 36(3):145–148, Jan 1976.
- [6] Jr. S. J. Allen, D. C. Tsui, and R. A. Logan. Observation of the Two-Dimensional Plasmon in Silicon Inversion Layers. *Phys. Rev. Lett.*, 38:980, 1977.
- [7] Shuji Hasegawa, Norio Sato, Ichiro Shiraki, Cristian L. Petersen, Peter Boggild, Torben M. Hansen, Tadaaki Nagao, and Francois Grey. Surface-State Bands on Silicon-Si(111)- $\sqrt{3} \times \sqrt{3}$ -Ag Surface Superstructure. *Jpn. J. Appl. Phys.*, 39(6B):3815, June 2000.

- [8] T. Nagao, T. Hildebrandt, M. Henzler, and S. Hasegawa. Dispersion and Damping of a Two-Dimensional Plasmon in a Metallic Surface-State Band. *Phys. Rev. Lett.*, 86:5747, 2001.
- [9] M. P. Seah and W. A. Dench. Quantitative electron spectroscopy of surfaces: A standard data base for electron inelastic mean free paths in solids. *Surf. Interface Analysis*, 1:2, October 1979.
- [10] H. Ibach. Surface Vibrations of Silicon Detected by Low-Energy Electron Spectroscopy. *Phys. Rev. Lett.*, 27(5):253–256, Aug 1971.
- [11] H. Froitzheim. *Topics in Current Physics*, volume 4. Springer-Verlag, Berlin, 1980.
- [12] W. H. Weinberg. *Experimental Methods of Surface Physics*, volume 15. Academic Press, New York, 1980.
- [13] R. F. Willis, editor. *Vibrational Spectroscopy of Adsorbates*, volume 15 of *Chemical Physics*, Berlin, 1980. Springer-Verlag.
- [14] H. Ibach and D. L. Mills. *Electron Energy Loss Spectroscopy and Surface vibrations*. Academic Press, New York, 1982.
- [15] L. Lüth. *Solid surfaces, interfaces and thin films*. Springer, Berlin, 4th, rev. and extended ed. edition, 2001.
- [16] W. Ho, R. F. Willis, and E. W. Plummer. Observation of Nondipole Electron Impact Vibrational Excitations: H on W(100). *Phys. Rev. Lett.*, 40(22):1463, 1978.

- [17] Yu Liu, Roy F. Willis, K. V. Emtsev, and Th. Seyller. Plasmon dispersion and damping in electrically isolated two-dimensional charge sheets. *Phys. Rev. B Rapid Comm.*, 78:201403(R), 2008.
- [18] V. G. Lifshits, A. A. Saranin, and A. V. Zotov. *Surface Phases on Silicon: Preparation, Structures, and Properties*. J. Wiley, Chichester, 1994.
- [19] T. Takayanagi, Y. Tanishiro, and S. Takahashi M. Takahashi. Structure analysis of Si(111)-(7 × 7) reconstructed surface by transmission electron diffraction. *Surf. Sci.*, 164:367, 1985.
- [20] Guo-Xin Qian and D. J. Chadi. Si(111)-(7 × 7) surface: Energy-minimization calculation for the dimer-adatom-stacking-fault model. *Phys. Rev. B*, 35(3):1288–1293, Jan 1987.
- [21] S. Hasegawa, X. Tong, C. Jiang, Y. Nakajima, and T. Nagao. Electrical conduction via surface-state bands. *Surf. Sci.*, 386:322, 1997.
- [22] R. Losio, K. N. Altmann, and F. J. Himpsel. Fermi surface of Si(111)7 × 7. *Phys. Rev. B*, 61(16):10845–10853, Apr 2000.
- [23] H. Froitzheim, U. Köhler, and H. Lammering. Electronic structure of the 7 × 7 Si(111): Differences due to preparation. *Phys. Rev. B*, 30(10):5771–5776, Nov 1984.
- [24] J. E. Demuth and B. N. J. Persson. High resolution electron energy loss studies of fermi level states of clean and metallized Si(111) surfaces. *J. Vac. Sci. Technol. B*, (B 2(3)):384, July-Sept. 1984.

- [25] B. N. J. Persson and J. E. Demuth. Inelastic scattering of slow electrons from Si(111) surfaces. *Phys. Rev. B*, 30(10):5960, November 1984.
- [26] K. J. Wan, X. F. Lin, and J. Nogami. Surface reconstructions in the Ag/Si(111) system. *Phys. Rev. B*, 47(20):12700, May 1993.
- [27] M. Katayama, R. S. Williams, M. Kato, E. Nomura, and M. Aono. Structure analysis of the Si(111)($\sqrt{3} \times \sqrt{3}$) $R30^\circ$ -Ag surface. *Phys. Rev. Lett.*, 66(21):2762–2765, May 1991.
- [28] T. Takahashi and S. Nakatani. Refinement of the $\sqrt{3} \times \sqrt{3}$ -Ag structure by surface X-ray diffraction. *Surf. Sci.*, 282:17, 1993.
- [29] N. Sato, T. Nagao, and S. Hasegawa. Si(111) $\sqrt{3} \times \sqrt{3}$ -Ag surface at low temperature: symmetry breaking and surface twin boundaries. *Surf. Sci.*, 442:65, 1999.
- [30] Xiao Tong, Chun Sheng Jiang, and Shuji Hasegawa. Electronic Structure of the Si(111) - $\sqrt{21} \times \sqrt{21}$ -(Ag+Au) surface. *Phys. Rev. B*, 57(15):9015, April 1998.
- [31] L. S. O. Johansson, E. Landemark, C. J. Karlsson, and R. I. G. Uhrberg. Fermi-level pinning and surface-state band structure of the Si(111)-($\sqrt{3} \times \sqrt{3}$) $R30^\circ$ -Ag surface. *Phys. Rev. Lett.*, 63(19):2092–2095, Nov 1989.
- [32] F. Stern. Polarizability of a Two-Dimensional Electron Gas. *Phys. Rev. Lett.*, 18:546, 1967.
- [33] Yinghui Yu, Ying Jiang, Zhe Tang, Qinlin Guo, Jinfeng Jia, Qikun Xue, Kehui Wu, and Enge Wang. Thickness dependence of surface plasmon damping and dispersion in ultrathin Ag films. *Phys. Rev. B*, (72):205405, 2005.

- [34] F. Moresco, M. Rocca, T. Hildebrandt, and M. Henzler. Plasmon Confinement in Ultrathin Continuous Ag Films. *Phys. Rev. Lett.*, 83(11):2238, September 1999.
- [35] J. N. Crain, M. C. Gallagher, J. L. McChesney, M. Bissen, and F. J. Himpsel. Doping of a surface band on Si(111)- $\sqrt{3} \times \sqrt{3}$ -Ag. *Phys. Rev. B*, (72):045312, 2005.
- [36] Yuji Nakajima, Sakura Takeda, Tadaaki Nagao, and Shuji Hasegawa. Surface electrical conduction due to carrier doping into a surface-state band on Si(111)- $\sqrt{3} \times \sqrt{3}$ -Ag. *Phys. Rev. B*, 56(11):6782, September 1997.
- [37] Yuji Nakajima, Gen Uchida, Tadaaki Nagao, and Shuji Hasegawa. Two-dimensional adatom gas on the Si(111) - $\sqrt{3} \times \sqrt{3}$ - Ag surface detected through changes in electrical conduction. *Phys. Rev. B*, 54(19):14134, November 1996.
- [38] Norio Sato, Tadaaki Nagao, and Shuji Hasegawa. Two-dimensional adatom gas on the Si(111)- $\sqrt{3} \times \sqrt{3}$ -Ag surface directly observed by scanning tunneling microscopy. *Phys. Rev. B*, 60(23):16083, December 1999.
- [39] H. Ehrenreich and H. R. Philipp. Optical Properties of Ag and Cu. *Phys. Rev.*, 128(4):1622–1629, Nov 1962.
- [40] A. Liebsch. Surface-plasmon dispersion and size dependence of Mie resonance: Silver versus simple metals. *Phys. Rev. B*, 48(15):11317–11328, Oct 1993.
- [41] Lin Huang, S. Jay Chey, and J. H. Weaver. Metastable structures and critical thicknesses: Ag on Si(111)-(7 \times 7). *Surf. Sci.*, 416:1101, 1998.
- [42] E. A. Taft and H. R. Philipp. Optical Properties of Graphite. *Phys. Rev.*, 138(1A), August 1965.

- [43] Mildred S. Dresselhaus and John G. Mavroides. Magnetoreflexion Experiments in Graphite. *Carbon*, 1:263, 1964.
- [44] J. W. McClure. Band Structure of Graphite and de Haas-van Alphen Effect. *Phys. Rev.*, 108(3):612, November 1957.
- [45] R. F. Willis, B. Fitton, and G. S. Painter. Secondary-electron emission spectroscopy and the observation of high-energy excited states in graphite: Theory and experiment. *Phys. Rev. B*, 9:1926, 1974.
- [46] James F. Annett, R. E. Palmer, and R. F. Willis. Surface dielectric response of a semimetal: Electron-energy-loss spectroscopy of graphite. *Phys. Rev. B*, 37(5):2408, February 1988.
- [47] P. Laitenberger and R. E. Palmer. Plasmon Dispersion and Damping at the Surface of a Semimetal. *Phys. Rev. Lett.*, 76:1952, 1996.
- [48] L. G. Jonhnsen and G. Dresselhaus. Optical Properties of Graphite. *Phys. Rev. B*, 7(6):2275, March 1973.
- [49] A. K. Geim and K. S. Novoselov. The rise of graphene. *Nature Materials*, 6(3):183, March 2007.
- [50] J. C. Slonczewski and P. R. Weiss. Band Structure of Graphite. *Phys. Rev.*, 109(2):272, January 1958.
- [51] J. W. McClure. Energy Band Structure of Graphite. *IBM J.*, page 255, July 1964.

- [52] K. S. Novoselov, A. K. Geim, S. V. Morozov, D. Jiang, Y. Zhang, S. V. Dubonos, I. V. Grigorieva, and A. A. Firsov. Electric Field Effect in Atomically Thin Carbon Films. *Science*, 306:666, 2004.
- [53] K. S. Novoselov, A. K. Geim, S. V. Morozov, D. Jiang, M. I. Katsnelson, I. V. Grigorieva, S. V. Dubonos, and A. A. Firsov. Two-dimensional gas of massless Dirac fermions in graphene. *Nature*, 438:197, November 2005.
- [54] Zhang Yuanbao, Yan-Wen Tan, Horst L. Stormer, and Philip Kim. Experimental observation of the quantum Hall effect and Berry’s phase in graphene. *Nature*, 438:201–204, 2005.
- [55] C. Berger, Z Song, X. Li, X. Wu, N. Brown, C. Naud, D. Mayou, T. Li, J. Hass, A. N. Marchenkov, E. H. Conrad, P. N. First, and W. A. de Heer. Electronic Confinement and Coherence in Patterned Epitaxial Graphene. *Science*, 312:1192, 2006.
- [56] S. V. Morozov, K. S. Novoselov, F. Schedin, D. Jiang, A. A. Firsov, and A. K. Geim. Two-dimensional electron and hole gases at the surface of graphite. *Phys. Rev. B*, 72:201401, 2005.
- [57] A. Bostwick, T. Ohta, Th. Seyller, K. Horn, and E. Rotenberg. Quasiparticle dynamics in graphene. *Nature Physics*, 3:36, 2007.
- [58] C. Berger, Z. Song, T. Li, X. Li, A. Y. Ogbazghi, R. Feng, Z. Dai, A. N. Marchenkov, E. H. Conrad, P. N. First, and W. A. de Heer. Ultrathin Epitaxial Graphite: 2D

- Electron Gas properties and a Route toward Graphene-based Nanoelectroics. *J. Phys. Chem. B*, 108:19912, 2004.
- [59] H. Shioyama. Cleavage of graphite to graphene. *J. Mater. Sci. Lett*, 20:499, 2001.
- [60] B. Partoens and F. M. Peeters. From graphene to graphite: Electronic structure around the K point. *Phys. Rev. B*, 74:075404, 2006.
- [61] C. F. Hirjibehedin, A. Pinczuk, B. S. Dennis, L. N. Pfeiffer, and K. W. West. Evidence of electron correlations in plasmon dispersions of ultralow density two-dimensional electron systems. *Phys. Rev. B*, 65:161309, 2002.
- [62] M. Wilson. Electrons in Atomically Thin Carbon Sheets Behave Like Massless Particles. *Physics Today*, 59(1):21, 2006.
- [63] T. Pichler, M. Knupfer, M. S. Golden, J. Fink, A. Rinzler, and R. E. Smalley. Localized and Delocalized Electronic States in Single-Wall Carbon Nanotubes. *Phys. Rev. Lett.*, 80:4729, 1998.
- [64] E. H. Hwang and S. Das Sarma. Dielectric function, screening, and plasmons in two-dimensional graphene. *Phys. Rev. B*, 75:205418, 2007.
- [65] V. M. Silkin, A. Garcia-Lekue, J. M. Pitarke, E. V. Chulkov, E. Zaremba, and P. M. Echenique. Novel low-energy collective excitation at metal surfaces. *Europhys. Lett.*, 66(2):260, 2004.
- [66] Takeshi Inaoka, Tadaaki Nagao, Shuji Hasegawa, Torsten Hildebrandt, and Martin Henzler. Two-dimensional plasmon in a metallic monolayer on a semiconductor surface: Exchange-correlation effects. *Phys. Rev. B*, 66(24):245320, Dec 2002.

- [67] I. Forbeaux, J.-M. Themlin, and J.-M. Debever. Heteroepitaxial graphite on 6H-SiC(0001):Interface formation through conduction-band electronic structure. *Phys. Rev. B*, 58:16396, 1998.
- [68] K. V. Emtsev, Th. Seyller, F. Speck, L. Ley, P. Stojanov, J.D. Riley, and R.G.C. Leckey. Initial stages of the graphite-SiC(0001) interface formation studied by photoelectron spectroscopy. *Mater. Sci. Forum*, 556:525, 2007.
- [69] L. Li, C. Tindall, Y. Hasegawa O. Takaoka, and T. Sakurai. Structural and vibrational properties of 6H-SiC(0001) surfaces studied using STM/HREELS. *Surf. Sci.*, 385:60, 1997.
- [70] Ronald Fuchs and K. L. Kliewer. Optical modes of vibration in an ionic crystal slab. *Phys. Rev.*, 140(6A):A2076, 1965.
- [71] H. Ibach. Optical Surface Phonons in Zinc Oxide Detected by Slow-Electron Spectroscopy. *Phys. Rev. Lett.*, 24(25):1416–1418, Jun 1970.
- [72] R. Matz and H. Lüth. Conduction-Band Surface Plasmons in the Electron-Energy-Loss Spectrum of GaAs(110). *Phys. Rev. Lett.*, 46(7):500–503, Feb 1981.
- [73] T. Angot, M. Portail, I. Forbeaux, and J. M. Layet. Graphitization of the 6H-SiC(0001) surface studied by HREELS. *Surf. Sci.*, 502:81, 2002.
- [74] W.-H. Soe, K. H. Rieder, A. M. Shikin, V. Mozhaikii, A. Varykhalov, and O. Rader. Surface phonon and valence band dispersions in graphite overlayers formed by solid-state graphitization of 6H-SiC(0001). *Phys. Rev. B*, 70:115421, 2004.

- [75] V. van Elsbergen, H. Nienhaus, and W. Monch. Dynamical properties of 3C-, 4H-, and 6H-SiC surfaces. *Appl. Surf. Sci.*, 123:38, 1998.
- [76] T. Balster, F. S. Tautz, V. M. Polyakov, H. Ibach, S. Sloboshanin, R. Ottking, and J. A. Schaefer. Strong dispersion of the surface optical phonon of silicon carbide in the near vicinity of the surface Brillouin zone center. *Surf. Sci.*, 600:2886, 2006.
- [77] R. F. Willis, editor. *Vibrational Spectroscopy of Adsorbates*, chapter Theory of dipole electron scattering from adsorbates. Springer-Verlag, New York, 1980.
- [78] Th. Seyller, K.V. Emtsev, F. Speck, K.-Y. Gao, and L. Ley. Schottky barrier between 6H-SiC and graphite: Implications for metal/SiC contact formation. *Appl. Phys. Lett.*, 88:242103, 2006.
- [79] N. H. March and M. P. Tosi. Collective effects in condensed conduction phase including low dimensional systems. *Adv. Phys.*, 44:299, 1995.
- [80] A. Yurtsever, V. Moldoveanu, and B. Tanatar. Dynamic correlation effects on the plasmon dispersion in a two-dimensional electron gas. *Phys. Rev. B*, (67):115308, 2003.
- [81] Taisuke Ohta, Aaron Bostwick, J. L. McChesney, Thomas Seyller, Karsten Horn, and Eli Rotenberg. Interlayer interaction and electronic screening in multilayer graphene investigated with angle-resolved photoemission spectroscopy. *Phys. Rev. Lett.*, 98:206802, 2007.
- [82] F. Guinea. Charge distribution and screening in layered graphene systems. *Phys. Rev. B*, 75:235433, 2007.

- [83] Taisuke Ohta, Aaron Bostwick, Thomas Seyller, Karsten Horn, and Eli Rotenberg.
Controlling the Electronic Structure of Bilayer Graphene. *Science*, 313:951, 2006.

Vita

Yu Liu

Education

The Pennsylvania State University, State College, Pennsylvania 2002–Present

Ph.D. in Physics. Thesis adviser: Prof. Roy F. Willis

Fudan University, Shanghai, China 1997–2002

B.S. in Applied Physics. Thesis Advisor: Prof. Shaolong Zhu

Awards and Honors

Ren Min Scholarship, Fudan University 1997–2002

Braddock Fellowship, The Pennsylvania State University 2002, 2003

Duncan Fellowship, The Pennsylvania State University 2005, 2006, 2007

Professional Affiliations

American Physical Society

American Vacuum Society

Selected Publications

Y. Liu, R. F. Willis, K. V. Emtsev, and Th. Seyller, "Plasmon Dispersion and Damping in Electrically-isolated Two-dimensional Charge Sheets" Phys. Rev. B Rapid Comm. **78**, 201403 (2008)

Y. Liu (Presenter), K.V. Emtsev, Th. Seyller, R.F. Willis, "Two Dimensional Plasmon Behavior in Graphene Sheets on SiC(0001)", The 55th AVS International Symposium, Boston, MA October 2008

Y. Liu (presenter), H. Won, and R. F. Willis, "2D Sheet-Plasmon Behavior and Screening Effects at the Silicon-Diode Schottky Barrier Interface", Physical Electronics Conference, Urbana, IL June 2007